CONTROL AND ROBUSTNESS ANALYSIS OF HOMOGENEOUS CHARGE COMPRESSION IGNITION USING EXHAUST RECOMPRESSION

A DISSERTATION
SUBMITTED TO THE DEPARTMENT OF MECHANICAL ENGINEERING
AND THE COMMITTEE ON GRADUATE STUDIES
OF STANFORD UNIVERSITY
IN PARTIAL FULFILLMENT OF THE REQUIREMENTS
FOR THE DEGREE OF
DOCTOR OF PHILOSOPHY

Hsien-Hsin Liao
May 2011

Abstract

There has been an enormous global research effort to alleviate the current and projected environmental consequences incurred by internal combustion (IC) engines, the dominant propulsion systems in ground vehicles. Two technologies have the potential to improve the efficiency and emissions of IC engines in the near future: variable valve actuation (VVA) and homogeneous charge compression ignition (HCCI).

IC engines equipped with VVA systems are proven to show better performance by adjusting the valve lift and timing appropriately. An electro-hydraulic valve system (EHVS) is a type of VVA system that possesses full flexibility, i.e., the ability to change the valve lift and timing independently and continuously, making it an ideal rapid prototyping tool in a research environment. Unfortunately, an EHVS typically shows a significant response time delay that limits the achievable closed-loop bandwidth and, as a result, shows poor tracking performance. In this thesis, a control framework that includes system identification, feedback control design, and repetitive control design is presented. The combined control law shows excellent performance with a root-mean-square tracking error below 40 μm over a maximum valve lift of 4 mm. A stability analysis is also provided to show that the mean tracking error converges to zero asymptotically with the combined control law.

HCCI, the other technology presented in this thesis, is a combustion strategy initiated by compressing a homogeneous air-fuel mixture to auto-ignition, therefore, ignition occurs at multiple points inside the cylinder without noticeable flame propagation. The result is rapid combustion with low peak in-cylinder temperature, which gives HCCI improved efficiency and reduces NO_x formation. To initiate HCCI with a typical compression ratio, the sensible energy of the mixture needs to be high

compared to a spark ignited (SI) strategy. One approach to achieve this, called recompression HCCI, is by closing the exhaust valve early to trap a portion of the exhaust gas in the cylinder.

Unlike a SI or Diesel strategy, HCCI lacks an explicit combustion trigger, as auto-ignition is governed by chemical kinetics. Therefore, the thermo-chemical conditions of the air-fuel mixture need to be carefully controlled for HCCI to occur at the desired timing. Compounding this challenge in recompression HCCI is the re-utilization of the exhaust gas which creates cycle-to-cycle coupling. Furthermore, the coupling characteristics can change drastically around different operating points, making combustion timing control difficult across a wide range of conditions. In this thesis, a graphical analysis examines the in-cylinder temperature dynamics of recompression HCCI and reveals three qualitative types of temperature dynamics. With this insight, a switching linear model is formulated by combining three linear models: one for each of the three types of temperature dynamics. A switching controller that is composed of three local linear feedback controllers can then be designed based on the switching model. This switching model/control formulation is tested on an experimental HCCI testbed and shows good performance in controlling the combustion timing across a wide range. A semi-definite program is formulated to find a Lyapunov function for the switching model/control framework and shows that it is stable.

As HCCI is dictated by the in-cylinder thermo-chemical conditions, there are further concerns about the robustness of HCCI, i.e., the boundedness of the thermo-chemical conditions with uncertainty existing in the ambient conditions and in the engine's own characteristics due to aging. To assess HCCI's robustness, this thesis presents a linear parameter varying (LPV) model that captures the dynamics of recompression HCCI and possesses an elegant model structure that is more amenable to analysis. Based on this model, a recursive algorithm using convex optimization is formulated to generate analytical statements about the boundedness of the in-cylinder thermo-chemical conditions. The bounds generated by the algorithm are also shown to relate well to the data from the experimental testbed.

Acknowledgements

I once discussed with my labmates in the Dynamic Design Lab (DDL) about how much funding it takes to support a Ph.D. student during the course of his/her study (we engineers like to put things into perspective with numbers). It worked out to be an incredibly large sum, which made me, the only student in the DDL who brought along zero fellowship/scholarship funding of his own, realize how fortunate I was. It seemed that my advisor, Prof. Chris Gerdes, could've made a much safer bet than offering me a position in his lab. And I am truly grateful to him for this; and much more - During the past five years, Chris has been excellent in being a guidance in research, a motivational speaker when I failed, a cheerleader when I had successes, and a friend who has inspired me and many others with his passion for science and life. I can't thank him enough for everything he's done for me, and for the rewarding experience that I've had at Stanford.

I also want to thank my thesis reading committee. Thanks to Prof. Chris Edwards for reading and critiquing my thesis. Being a control engineer, I am very grateful for the feedback from a thermodynamics and engine guru like Chris. Thanks to Prof. Rolf Johansson, who came all the way from Sweden for my defense, for offering new perspectives on my thesis that I never thought of, as well as providing a taste of the Swedish tradition of having an "opponent" in one's defense. Thanks also to Prof. Mark Cutkosky and Prof. Steve Rock for serving on my defense committee, and for having a stimulating discussion with me in the closed session.

A lot of thanks to Prof. Ting-Jen Yeh at National Tsing Hua University in Taiwan. Working with him on a bipedal walking robot during my undergraduate years has intrigued me to learn more about control and dynamical systems, and has very much

shaped my career path.

I am also thankful for the awesome people in the DDL that I get to work with. Particularly, I'd like to thank the C-Unit (Combustion-Unit) in the DDL: Greg Shaver, Matt Roelle, Nikhil Ravi, Adam Jungkunz, Anders Widd and Steve Erlien. Although my time at Stanford does not overlap with Greg's, I'd like thank him for his advice on grad school and the beer he bought when we met in conferences. A lot of credits go to Matt, who contributed a great deal to the second chapter of this thesis. I bombarded Matt with countless questions when I started in the DDL with practically zero knowledge about engines, and I thank him for his incredible patience and guidance. Thanks to Nikhil, whose modeling work forms the foundation of this thesis. Nikhil sat next to me in the lab for four years and was always the first person I bothered when I needed to discuss research ideas with someone. I am very grateful for his insight over the years. Thanks also go to Adam, who took the lead in the daunting task of integrating the experimental engine test bed used in this thesis. I will always remember the time we spent together figuring out homework problems, fixing the engine, running experiments and talking baseball. I'd also like to thank Anders, our honorary C-Unit member from Sweden, for the great collaboration that we had, and for discussing video games with me at a very high intellectual level. Thanks also to Steve, who helped proof-read some of the math derivation in this thesis and improved its presentation. I also shared some of the best memories in life with my labmates in the DDL: Craig Beal, Carrie Bobbier, Holly Butterfield, Sam Chang, Chris Gadda, Rami Hindiyeh, Judy Hsu, John Kegelman, Mick Kritiyakirana, Shad Laws, Hyungchai Park, Josh Switkes and Kirstin Talvala. I've never seen a group of people enjoys each other's company as much as we do, and my graduate school experience would have been a lot duller without their camaraderie.

Thanks to our industrial collaborators at Bosch and General Motors for providing technical and financial support for the work presented in this thesis. I'd also like to thank our lab technicians Scott Sutton and Godwin Zhang. We have a reliable and robust engine test bed for research thanks to their hard work.

Last but certainly not least, thanks to my wonderful family - My parents have always put their children before themselves, and have always supported me no matter

what I choose to pursue in life. I owe all my accomplishments to the love that they've given me since day one. Thanks also to my little sister, Shu-Hui, for being a great friend who kindly puts up with her sometimes obnoxious brother. My wife, Krystal, is an incredibly intuitive mechanical engineer. I am very grateful that she put her career in Taiwan on hold just to be with me in the US. Thank you all for being there for me through the highs and lows of my life.

Contents

List of Tables

List of Figures

Chapter 1

Introduction

1.1 Background

In 2005, according to its Energy Information Administration [1] the U.S. emitted 5974.3 million metric tons (MMT) of carbon dioxide (CO_2) , which ranked first in the world. Roughly 25% of that total amount (1628.6 MMT) could be attributed to internal combustion (IC) engines on ground vehicles. The high percentage reflected the fact that the U.S. averaged 0.83 vehicles per capita, the highest anywhere in the world [2]. The rest of the developed world showed lower-but-comparable numbers. In 2006, China overtook the U.S. in terms of the total amount of CO_2 emitted [3], with a meager average of 0.024 vehicles per capita. India painted a similar picture with its total CO_2 emissions of 1652.1 MMT in 2009 (fifth in the world, after China, the U.S., the European Union and Japan) [3] and 0.012 vehicles per capita. With a combined population of 2.5 billion that is quickly becoming more affluent, China and India represent a developing world that, rightfully, aspires to the same personal mobility enjoyed by the developed countries. This makes the global outlook for capping CO_2, the major source of greenhouse gas, all the grimmer. In addition to CO_2 emissions, IC engines produce oxides of nitrogen (NO_x) which are known to cause smog and acid rain.

To alleviate these current and projected environmental consequences, there has been an enormous research effort worldwide to find more sustainable ways to power

ground vehicles. Fuel cells, solar cells, and powertrain electrification are among the innovations proposed. However, none of the above is currently able to replace IC engines due to petroleum fuel's ease of storage and unparalleled energy density. Improving the efficiency and emissions of IC engines, therefore, remains the most direct way to have a far-reaching effect on curbing the environmental strain caused by ground vehicles. In the near future, two technologies have the potential to make IC engines cleaner and more efficient: Variable Valve Actuation (VVA) and Homogeneous Charge Compression Ignition (HCCI). The merits and challenges associated with these technologies are discussed in Sections 1.2 and 1.3.

1.2 Variable Valve Actuation

Internal combustion engines equipped with VVA systems are proven to achieve better combustion characteristics. Novel valve strategies that appropriately vary the valve lift and/or timing can increase fuel economy [4, 5], reduce emissions [6] and boost power output [7, 8]. Furthermore, a VVA system can serve as a useful control knob for homogeneous charge compression ignition [9], the other efficiency and pollution improving technology discussed in this thesis.

There are a number of VVA systems on production engines capable of adjusting the aforementioned valve profile parameters but, in general, the adjustments are restricted due to packaging or cost constraints. For example, a cam phaser can adjust the relative rotational position between the cam shaft and crank shaft but cannot change the valve profile (fixed lift and opening duration). Furthermore, the range and slew rate of the phasing adjustment are limited. The Honda VTEC (variable valve timing and lift technology) system is another production VVA system [8]. This system has two sets of cam lobes on the cam shaft with different lift and timing configurations. Depending on the engine speed, one of the two cam lobes is engaged at a time, providing different engine breathing characteristics. The adjustment of lift and timing with the VTEC system, therefore, has only two steps and are not independent to each other.

The desire to have full flexibility in valve motion is even greater in a research environment where innovative valve strategies are developed and validated. An electro-hydraulic valve system (EHVS) is a system that can independently and continuously change the valve lift and timing on a cycle-by-cycle basis, making it ideal in a research laboratory. A schematic of a typical EHVS is shown in Fig. 1.1. There is a pump generating the high pressure supply in this hydraulic system. The first stage of the system is a spool valve driven by a voice coil. The position of the spool valve position determines the cross-sectional area of the hydraulic fluid paths and generates a pressure difference across the actuator piston. The pressure difference ultimately creates a force that moves the valve actuator which is connected to an engine valve. Therefore, the valve position can be completely decoupled from the crank position on an IC engine by using an EHVS instead of a mechanical cam.

Obviously, the full flexibility afforded by the EHVS comes with the price of greater system complexity and bulkiness, making it unsuitable for production engines. However, an EHVS can serve as a rapid prototyping tool in a research environment to explore new valve strategies that can be later emulated by more compact VVA systems suitable for production vehicles.

1.2.1 Challenges with EHVS

The concept of using an EHVS as a rapid prototyping tool in a research laboratory is appealing. However, the valve position control of such an apparatus must be accurate and consistent over the operating range of interest. Error and inconsistency in valve position add more variabilities when researchers try to make sense of the subsequent combustion results. Unfortunately, the flexibility provided by an EHVS is coupled with difficulties in valve position control. This is largely due to the response time delay that results from compressibility of the hydraulic fluid and nonlinearity of the system. In particular, the time delay decreases the phase margin of the system and limits the achievable closed-loop bandwidth of the system. Effectively, this translates to poor tracking performance that is inadequate for a research environment.

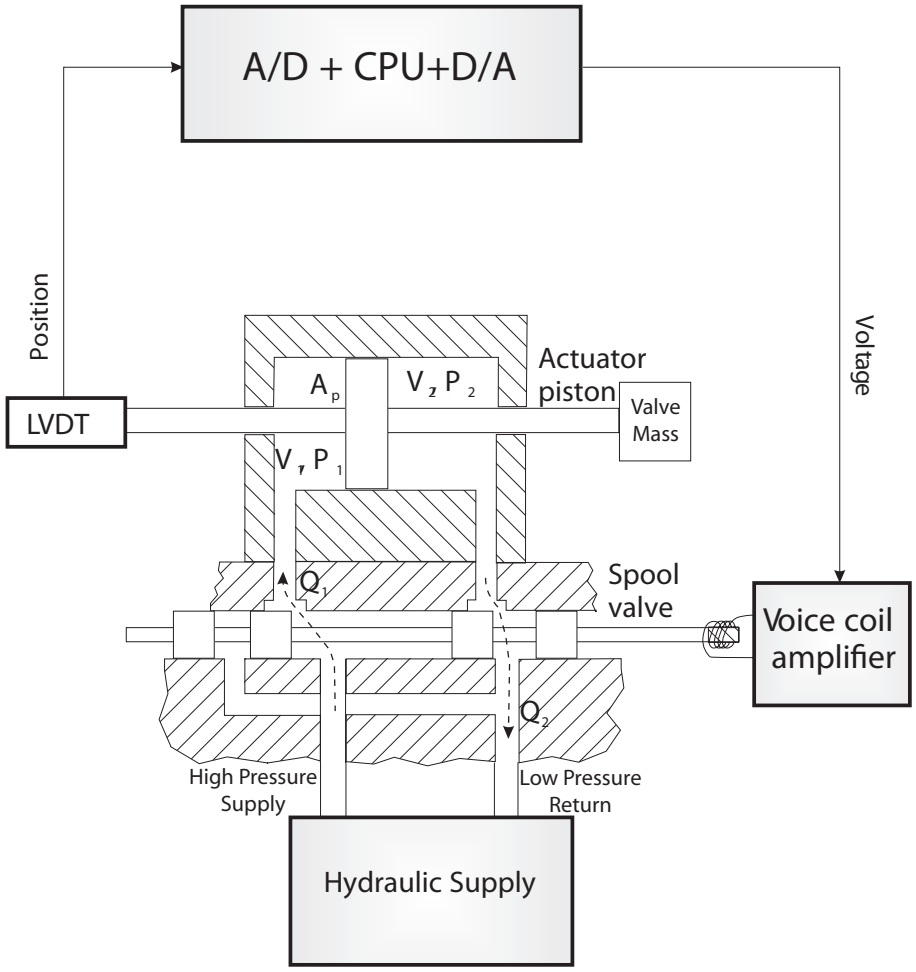

Figure 1.1: Schematics of an EHVS

1.2.2 Related Work on EHVS

A number of researchers contributed to understanding the dynamics of an EHVS. Some of the earliest modeling work was performed by Richman [10]. He constructed a five state nonlinear model based on fluid mechanics and rigid body dynamics. The model consisted of two mass-spring-damper modes for the valve actuator and spool valve, and a first order fluid dynamics mode. Hathout *et al.* later showed that the spool valve dynamics are at least an order of magnitude faster than the rest of the system modes and can be neglected. As a result, they showed that a linearized third-order model is sufficient for feedback control design [11]. Various researchers

have developed controllers for EHVS [10, 12, 11]. Anderson *et al.* demonstrated an adaptive controller for EHVS [13] that controls the maximum valve lift. Since airflow dynamics do not correlate to maximum valve lift exclusively, there are uncertainties regarding how much air is inducted or exhausted if only the maximum valve lift is controlled. Sun *et al.* [14] showed that repetitive control [15] is very effective for the EHVS profile tracking problem, since valve motion is largely repetitive for steady-state engine operations. However, this approach assumes a fundamental period of the desired valve profile and, as a result, limits the EHVS to operate at several specific engine speeds. A significant portion of this thesis focuses on developing a control framework that yields tracking performance superior to these previous results.

1.3 Homogeneous Charge Compression Ignition

HCCI is a new combustion strategy (relative to a spark ignited or Diesel strategy) where a well-mixed air and fuel charge is compressed to its autoignition point. As a result, HCCI combustion takes place almost simultaneously across the cylinder without noticeable flame propagation [16] and better approximates the instantaneous energy conversion of an ideal Otto cycle. Compared to a spark ignited (SI) strategy, HCCI promises up to 30% increase in efficiency at low load [17]. The homogeneous mixture also eliminates the existence of fuel-rich spots, the main cause of particulate matter in a Diesel strategy. Lastly, HCCI has lower peak combustion temperature which significantly reduces NO_x emissions [18, 19].

To achieve HCCI with typical compression ratios, the sensible energy of the mixture needs to be higher than for a SI strategy. Heating the intake air [20] is one way to achieve the higher sensible energy required. The other method, often considered as the more practical one, is by re-utilizing the exhaust gas from the previous engine cycles, made possible by a variable valve actuation system [21, 22, 23, 9, 24, 25]. This method is called residual-affected HCCI. Two valve strategies have been proposed to re-introduce or retain exhaust in the cylinder. In rebreathing HCCI, the exhaust valve is opened a second time along with the intake valve as the piston moves towards bottom dead center (BDC) during the intake stroke. Therefore, exhaust is re-inducted

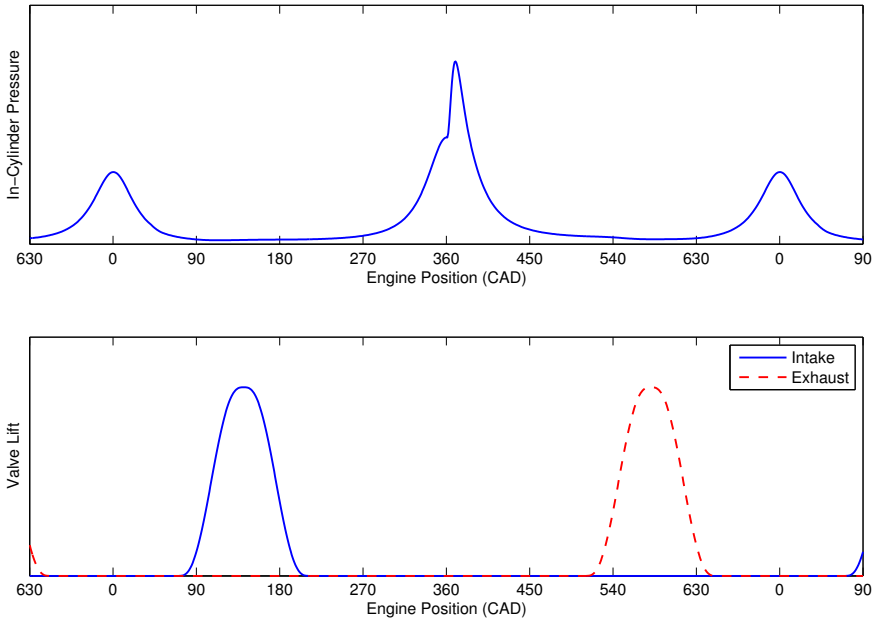

Figure 1.2: Typical recompression HCCI pressure trace and valve profiles

into the cylinder from the exhaust manifold and mixes with the air-fuel charge. The focus of this thesis, however, is HCCI by means of exhaust recompression.

A typical pressure trace and valve events for recompression HCCI are shown in Fig. 1.2. The engine position shown in the figure is referenced from gas exchange TDC and this is the convention adopted throughout this thesis. As can be seen in the top plot, a combustion event occurs around 360 CAD and the pressure trace shows an abrupt increase due to the near instantaneous energy conversion of HCCI. Work output is being extracted during the subsequent expansion stroke followed by an exhaust event shown in red in the bottom plot. The exhaust valve closure (EVC) timing is significantly earlier than that in a SI strategy to trap a significant portion of the exhaust gas in the cylinder. The retained exhaust is then recompressed, and, as a result, the pressure trace around gas-exchange TDC shows a tell-tale "hump". Fuel is injected into the cylinder during recompression, followed by the intake valve event shown in blue in the bottom plot of Fig. 1.2. Therefore, the fuel has sufficient

time to mix with the inducted air and trapped exhaust before the next combustion event. After intake valve closure (IVC), the homogenous mixture is then compressed to reach its autoignition point and the next HCCI event is initiated.

1.3.1 Challenges with Recompression HCCI

There are a number of obstacles to overcome before recompression HCCI can be reliably employed on production engines. They are listed as follows:

Lack of direct ignition trigger

Unlike conventional engines where combustion is initiated by direct triggers, i.e. a spark event in a SI engine or an injection event in a Diesel engine, HCCI relies on compressing a homogenous air-fuel mixture to its autoignition point. Therefore, only indirect inputs such as valve timings, fuel injection quantities, etc., can influence the thermo-chemical conditions of the mixture that, in turn, determine whether an HCCI event will occur or not upon compression. This obstacle becomes even more difficult when ignition is required to occur at a specific timing, which translates to controlling the thermo-chemical conditions to a high degree of accuracy using the available indirect inputs.

Cycle-to-cycle coupling

By trapping the exhaust gas and using it to initiate HCCI on the next cycle, recompression HCCI possesses cycle-to-cycle coupling. Therefore, the thermo-chemical conditions of the current engine cycle are not only functions of inputs, but also functions of the thermo-chemical conditions of the *previous* engine cycles. Essentially, recompression HCCI is a dynamical system instead of a static input-output mapping.

Significant change in system dynamics

The cycle-to-cycle dynamics of recompression HCCI can change significantly around different operating points. For example, the change in system dynamics can manifest itself as a three-fold increase in the standard deviation of ignition timing around an

ill-behaved operating point when compared to a "good" point, making the former unusable in practice. For HCCI to be practical for road use, it is desirable to have an operating range as wide as possible. This translates to the challenge of designing a controller that is effective across a wide range and is able to make ill-behaved open-loop operating points usable in closed loop.

Stability and robustness of HCCI

Stability of HCCI, loosely defined here as the boundedness of the in-cylinder thermochemical conditions, is an important topic of interest. Since HCCI is sensitive to these in-cylinder conditions, their divergence can lead to undesirable combustion characteristics or even misfires. Furthermore, a production engine and its surroundings change constantly due to aging hardware, and the different environments it operates in. Therefore, robustness of HCCI, that is, the boundedness of the in-cylinder conditions with uncertainties in the true system characteristics, is of even greater practical interest.

Currently, the majority of HCCI research in the literature focuses on overcoming the first two obstacles and the author summarizes some of it in the following section. This thesis aims to understand and overcome the latter two obstacles listed above, i.e., the change in HCCI dynamics and the stability and robustness of HCCI.

1.3.2 Related Work on HCCI

HCCI was first reported on two-stroke engines by Onishi *et al.* [26] and Noguchi [27] in 1979, and there has been much research effort in the past three decades aiming at employing HCCI on production engines. Early work demonstrated that HCCI can be achieved on research engines. Najt and Foster were the first to demonstrate that HCCI can be achieved on a four-stroke engine with blended isooctane and n-heptane [28]. Thring successfully achieved HCCI with gasoline and Diesel fuel [29] and mapped out the operating range of HCCI in terms of air-fuel ratio and exhaust gas recirculation rate at two engine speeds. Due to the lack of an explicit ignition

trigger, it was not until the mid-90s that more research reports on HCCI appeared in the literature when prototype VVA systems became available as an effective actuator for residual-affected HCCI. Since then, a lot of research effort has gone into modeling of HCCI to lend insight into the process and controlling the ignition timing and load of HCCI, as summarized in the following sections.

Modeling of HCCI

Models for HCCI are obtained from two techniques: system identification or physical modeling. In general, the former has the advantage of being faster to develop. Pfeiffer *et al.* used this approach in [30] and employed system identification at fifteen operating points on an experimental HCCI engine. The resulting fifteen, second-order models were then merged as a single model which showed good correlations to the engine data at the tested operating points. Another example is presented by Bengtsson *et al.* in [31] where a second-order model was obtained using system identification on a six-cylinder engine. The resulting linear model showed good performance in predicting combustion timing in the validation experiments.

On the other hand, physics-based models have the merits of being more portable across engines as they are governed by the same set of physical laws. Physics-based HCCI models generally fall into two groups: control-oriented, single-zone models and higher-dimension models. The latter group consists of more complicated models that include some level of spatial distribution of the thermal and chemical conditions within the cylinder, and describe how this distribution varies in time. The model complexity, however, can vary greatly among models within this group. On the simpler end of the spectrum, the models typically divide the cylinder spatially into several zones. The thermo-chemical conditions of each zone can either evolve in isolation or interact with adjacent zones based on some assumptions. For example, Aceves *et al.* used a CFD model and a ten-zone chemical kinetics model to predict peak pressure, burn duration and hydrocarbon emissions of HCCI [32]. Fiveland *et al.* [33] used a two-zone combustion model that includes an adiabatic core and a thermal boundary layer to capture the heat transfer characteristics during HCCI combustions. On the other extreme, CFD models and detailed chemical kinetics model were used to

describe HCCI with a very fine spatial resolution [34, 35, 36]. These models are highly computationally intensive. For example, a run time of twelve hours was reported [35] in 2002 for a sixty degree crank-angle simulation.

The second group of physics-based models, the control-oriented single-zone models, disregard any spatial distribution. These models assume homogeneity across the cylinder and aim to capture, based on simplifying assumptions, how the thermo-chemical conditions evolve in time when influenced by various inputs, and how these conditions can be further related to the typical control objectives, i.e. ignition timing, work output, etc. Shaver *et al.* outlined one such model in [37] that captured the dynamics of peak pressure and angle of peak pressure with the IVC timing and re-inducted exhaust ratio as the model inputs. Using slightly different thermodynamic assumptions, Ravi *et al.* developed a model for recompression HCCI [38]. The system states in this model are the oxygen content and temperature of the in-cylinder gas which were more representative of the actual thermo-chemical conditions inside the cylinder. Chiang and Stenfanopoulou presented a model that captured the effect of rebreathing lift on the dynamics of the in-cylinder temperature at IVC [39]. Widd *et al.* combined the cycle-to-cycle temperature dynamics of HCCI with the slow-varying cylinder wall temperature dynamics to form a two-state model [40]. Kang *et al.* [41] captured the dynamics of the in-cylinder temperature at IVC which can be related to the average energy conversion rate during combustion. The models described above used simplified thermodynamics and fluid dynamics assumptions with the ultimate goal of providing more tractable platforms for model-based control synthesis.

Control of HCCI

Since the work output of HCCI is largely dependent on the total amount fuel injected into the cylinder as long as ignition occurs at an "appropriate" engine position, combustion timing control is arguably the most fundamental challenge in HCCI. A number of control actuators that can influence HCCI ignition timing have been explored, including intake air temperature [20, 42], variable compression ratio [43], variable valve timing [9, 24, 25], effective octane number with different blends of fuel [28, 44], and the timing of pilot injections during recompression [45, 46]. Using

these inputs, empirically tuned controllers or model-based controllers can be used to control the combustion timing of HCCI. Empirically tuned controllers are generally of proportional-integral-derivative (PID) type which is straightforward conceptually and widely used in the industry. Olsson *et al.* [47] demonstrated tracking of ignition phasing and load profile with three PID controllers modulating the intake air temperature, effective octane-number of fuel and total amount of fuel. Agrell *et al.* [9] demonstrated a PI controller to control ignition timing by varying negative valve verlap or intake valve closure timing.

The second group of controllers, the model-based controllers, are either based on models obtained from system identification or on the control-oriented models described in the previous section. Bengtsson *et al.* used a model predictive controller (MPC) to control ignition phasing and work output based on the identified model [44] is an example of the former method. On the other hand, control synthesis based on control-oriented models are slightly more complicated, since these models are generally nonlinear. One commonly used approach is to first linearize the model about an operating point. Control techniques for linear systems [48, 49], which are well-studied, can then be used with the resulting linearized systems. For example, Shaver *et al.* designed an H_2 controller based on the linearized, control-oriented model [25]. Control of peak pressure was achieved by varying the rebreathing exhaust valve timing with the H_2 controller. Widd *et al.* used a MPC based on the linearized model to control ignition phasing of HCCI [42] with variable valve actuation and intake temperature management. Ravi *et al.* used a pole-placement controller to control ignition phasing on a multi-cylinder HCCI engine [50]. These controllers had the advantages of being tractable to develop and showed good performance around the linearized points. However, since the cycle-to-cycle dynamics of recompression HCCI can vary dramatically across the operating range, this approach can hurt HCCI combustion when the operating conditions deviate from the linearized point. This thesis analyzes how recompression HCCI dynamics change in a wide operating range and reveals the range of applicability of a linearized model. Thanks to the insights from this analysis, a methodology for control design that is only marginally more complicated than the ones described above is shown to work well on an experimental testbed across a wide

range of operating conditions.

Stability and Robustness Statements

As discussed previously, stability and robustness of HCCI are areas where researchers want to have a better understanding with the various models. One type of stability statement is readily available by examining the eigenvalues of the identified models or linearized control-oriented models. The system eigenvalues shown in [44, 25, 50] all lay inside the unit circle on the complex plane, showing that HCCI, as a discrete-time system, was stable around the identification or linearized points. Chiang *et al.* [51] used a graphical approach and concluded the existence of a stable equilibrium by examining the gradients of the two temperature propagation curves that made up a returning map. The above stability results are, however, restrictive without a region of attraction to complement them. The ability to make statements about the state trajectories from a wide set of initial conditions is more desirable, since they include the system behavior beyond the vicinity of an equilibrium. Unfortunately, relevant reports are relatively scarce in the literature. Shaver [52] and Chiang *et al.* [53] both presented stability results based on their respective control-oriented models for rebreathing HCCI. In [52], Shaver presented a semi-definite program (SDP) for finding a Lyapunov function and was able to conclude asymptotic stability of peak pressure and angle of peak pressure. Chiang *et al.* formulated a nonlinear controller that cancels much of the nonlinearity present in their rebreathing HCCI model. As a result, asymptotic stability of the in-cylinder gas temperature could be derived with the nonlinear controller closing the loop. To the best of the author's knowledge, there were no robustness statements of HCCI, i.e., the boundedness of the in-cylinder conditions with model uncertainties, yet published.

To advance the understanding of the stability and robustness properties of HCCI, this thesis presents a model that captures the essential behavior of recompression HCCI with a linear-like structure. As a result, the proposed model is more amenable to stability and robustness analysis compared to other existing HCCI models. Using this new model, a recursive algorithm is presented to make statements about the stability and robustness characteristics of recompression HCCI.

1.4 Thesis Contribution

This thesis aims to fulfill three high-level research objectives. The specific contributions in each of the three areas are outlined below.

1. To achieve precise tracking performance with an EHVS
    - Developed a framework that includes system identification, a linear quadratic tracking control design and a repetitive control design that does not depend on a fundamental period in the desired valve profile. The combined control law showed a root-mean-square tracking error under 40 μm over a maximum valve lift of 4 mm.
    - Derived a stability criterion for the presented control framework.
    - Derived an analytical expression for the variance of the steady-state mean tracking error in the presence of measurement noise.
2. To develop an effective framework for controlling combustion timing of recompression HCCI across a wide range of operating conditions
    - Showed that there exist three qualitative types of temperature dynamics across a wide operating range.
    - Constructed a three-region switching linear model to capture the change in system dynamics for control purposes.
    - Developed a three-region controller that could track a wide range of desired combustion timing command and reduce the variability of combustion phasing over open loop operations.
    - Derived stability guarantees for the switching model/control formulation.
3. To establish stability and robustness statements about recompression HCCI
    - Developed a linear parameter varying (LPV) model that captures the essential cycle-to-cycle dynamics of recompression HCCI and is amenable to analysis.

- Formulated a recursive algorithm based on the LPV model that could establish stability statements for recompression HCCI.
- Generalized the stability algorithm to include modeling uncertainties. Robustness statements that are representative of the testbed behavior can then be made with this generalization.

1.5 Thesis Outline

This thesis consists of eight chapters, outlined as follows.

Chapter 2 describes a control framework for an EHVS. The chapter first explains the system identification method used to generate a mathematical model for the EHVS. Two feedback controller designs are formulated based on this model, and their tracking performance is evaluated on the EHVS. Furthermore, the results with the feedback controllers highlight the difficulty in achieving good tracking performance with the response delay present in the EHVS. To further improve the performance, a repetitive controller is formulated to augment the feedback controller, and the combined control law is shown to achieve excellent tracking results. The last part of this chapter includes a stability proof for the control framework presented and shows that the mean tracking error asymptotically converges to zero with the repetitive controller. An analysis of the variance of the mean tracking error is also presented to discuss the effect of sensor noise on the proposed control scheme.

Chapter 3 gives a brief summary of the control-oriented, single-zone model developed by Ravi [38], since it serves as the launching point of this thesis.

Chapter 4 uses a graphical analysis of the nonlinear model summarized in Chapter 3. This analysis reveals that there exist three types of temperature dynamics that can be related to the qualitative change in system behavior observed on an experimental HCCI engine. Based on the analysis, a three-region switching linear model composed of three local linearized models is constructed.

Chapter 5 presents a three-region switching controller based on the switching linear model described in Chapter 4. This controller can track a wide range of desired combustion phasing on the experimental HCCI testbed. Furthermore, this controller

is shown to reduce the variability of combustion phasing compared to open loop operations. This chapter further includes a semi-definite program (SDP) to find a Lyapunov function for the switching control/model formulation presented in Chapter 4 and 5. The obtained Lyapunov function guarantees that the switching controller is exponentially stable with the switching linear model about a single equilibrium. The SDP is further modified to discuss stability with respect to a set of equilibria simultaneously.

Chapter 6 derives a linear parameter varying (LPV) model that is formulated with the explicit goal of tractable stability and robustness analysis of HCCI. This model, which is based on the nonlinear model developed by Ravi *et al.* [38], uses two varying parameters to summarize the major system nonlinearities and uses a set of linear equations to describe the remaining system behavior. With this, the LPV model has a significant reduction in model complexity compared to the nonlinear model. This chapter further examines the LPV model in various numerical examples. The results show that this simplified model resembles the nonlinear model in all test cases.

Chapter 7 builds on the LPV model presented in Chapter 6 and formulates a recursive stability algorithm that can analytically establish the convergence of the two system states: in-cylinder oxygen content and temperature. The algorithm utilizes the convexity of the LPV model equations and can be very efficiently solved by convex optimization software. In the second part of this chapter, the stability algorithm is further generalized to accommodate modeling uncertainties. As a result, analytical robustness statements can be made, which have not been reported previously in the literature. The established robustness statements are also shown to relate well to the data taken from the experimental testbed.

Chapter 8 briefly summarizes this thesis and points out some possible future research directions related to the presented work.

Chapter 2

Control of an Electro-Hydraulic Engine Valve System

An electro-hydraulic valve system (EHVS) can independently and continuously adjust the valve timing and lift of an IC engine on a cycle-by-cycle basis, making it an ideal rapid prototyping tool in a research environment. However, with an EHVS, it is difficult to achieve the same level of accurate position control that a mechanical cam provides. In particular, the response time delay and nonlinear dynamics of the hydraulic system can lead to error in valve position control. This chapter presents a control framework that achieves good tracking performance with an EHVS. Section 2.1 first describes the system identification method used to generate a mathematical model for the EHVS. Section 2.2 compares two feedback control designs based on the identified model in Section 2.1, and highlights the inadequacy of using only feedback control due to the significant response delay present in the EHVS. The remainder of this chapter introduces a repetitive controller that generates a feed-forward input profile on a cycle-by-cycle basis and further improves the root-mean-square tracking performance of the EHVS to under 40 μm.

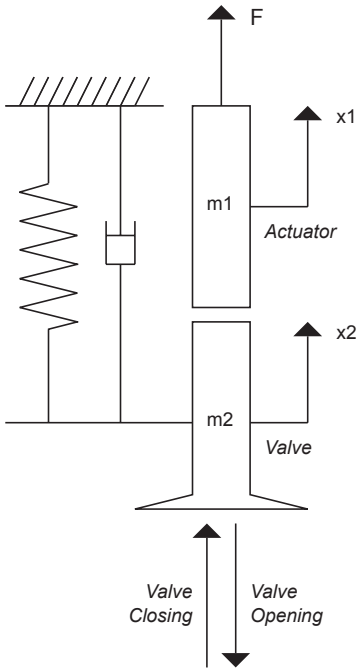

Figure 2.1: Valve and actuator illustration

2.1 System Identification

A schematic of the EHVS used in this thesis is shown in Fig. 1.1. The hydraulic pump supplies the EHVS with a fixed pressure of 20.7 MPa (3000 psi). The input of a single valve actuator takes an analog voltage to drive the voice coil which in turn drives the spool valve shown in Fig. 1.1. The spool valve position determines the cross-sectional area of the hydraulic fluid paths and generates a pressure difference across the hydraulic piston. The pressure difference ultimately creates a force that moves the valve actuator. A linear variable differential transformer (LVDT) is attached to the valve actuator to measure its position. The EHVS consists of eight such actuators and drives a total of sixteen intake and exhaust valves on a 2.2 liter four-cylinder GM Ecotech engine. The two intake (or exhaust) valves of each cylinder are paired together and driven by a single actuator. The Matlab xPC platform is used to generate voltage inputs to the voice coil amplifiers and to sense the position measurements from the LVDTs at 5 kHz. The particular sampling frequency is chosen

to exceed the desired closed loop bandwidth and to satisfy the limited computational capabilities of the hardware.

As discussed in Chapter 1, the dynamics of the EHVS can be represented by a five-state nonlinear model shown by Richman [10]. Hathout *et al.* [11] further show that two of the states associated with the spool valve are an order of magnitude faster than the engine valve mode and can be safely neglected for control design. This model structure is adopted in this thesis and the frequency response of the EHVS shown later indeed resembles a third-order linear system with input delay.

To use frequency identification techniques, the identification input must be sufficiently rich in frequency content to excite the system dynamics. The input should also be sufficiently large in magnitude to create a reasonable signal-to-noise ratio. Furthermore, the valve actuators are not rigidly linked to the engine valves as shown in Fig. 2.1. Therefore, the identification input needs to carefully chosen so that the valve contacts the actuator at all times. Detachment of the two elements might corrupt the identification results and, more importantly, could damage the valve-actuator contact surface due to large impact forces. To ensure continuous contact, the two elements must experience the same acceleration, and the reaction force between the two elements must be positive. The first condition gives the following equation:

$$\ddot{x}_1 = \frac{F+R}{m_1} = \frac{-d_2\dot{x}_2 - k_2(x_2 - x_{20}) - R}{m_2} = \ddot{x}_2 \tag{2.1}$$

where

m_1 is the actuator mass

m_2 is the valve mass

k_2 is the valve spring constant

d_2 is the valve damping coefficient

x_1 is the actuator position

x_2 is the valve position

x_{20} is the valve spring relaxed position

F is the actuator force

R is the reaction force between the two elements

Solving for R and restricting it to be positive, we have the following condition:

$$\frac{m_1 k_2(x_{20} - x_2) - m_1 d_2 \dot{x}_2 - m_2 F}{m_1 + m_2} > 0 \tag{2.2}$$

While the valve damping coefficient is difficult to measure, the valve spring force is very large compared to the force generated by the damping term. The valve spring is also heavily preloaded from its relaxed position of x_{20}. The actuator force can be bounded conservatively to be negative which translates to bounding the input voltage to be negative, since negative input voltage represents negative force in a steady-state sense. With this bound applied to the system identification input, the actuators and valves remain in contact during experiments. A pseudo random binary sequence (PRBS) is used to excite the EHVS, since a PRBS has rich frequency contents and its amplitude can be easily controlled to satisfy Equation (2.2). In addition, a dither at 800 Hz is added to overcome the static friction present in the spool valve.

The empirical transfer function estimate (ETFE) obtained using this setup is shown in Fig. 2.2. One important characteristic of the system is the presence of a 1 ms response delay. This delay likely arises from the compressibility of the hydraulic fluid and the friction between the hydraulic piston and cylinder. In general, the system behaves much like a third-order system with input delay. Therefore, we fit an eighth-order discrete model with the sampling rate of 5 kHz to the ETFE. Five of the eight states in this discrete model are used to represent the 1 ms response delay. The Bode plot of this discrete model is shown in the red dotted line in Fig. 2.2. The effect of the delay can be best seen from the phase plot: the green dashed line in the phase plot of Fig. 2.2 is a model that has the same dynamics except for the response delay, highlighting the phase loss that the delay introduces. In general, the model fits the ETFE well using this model structure. A discrete time model of one of the valve

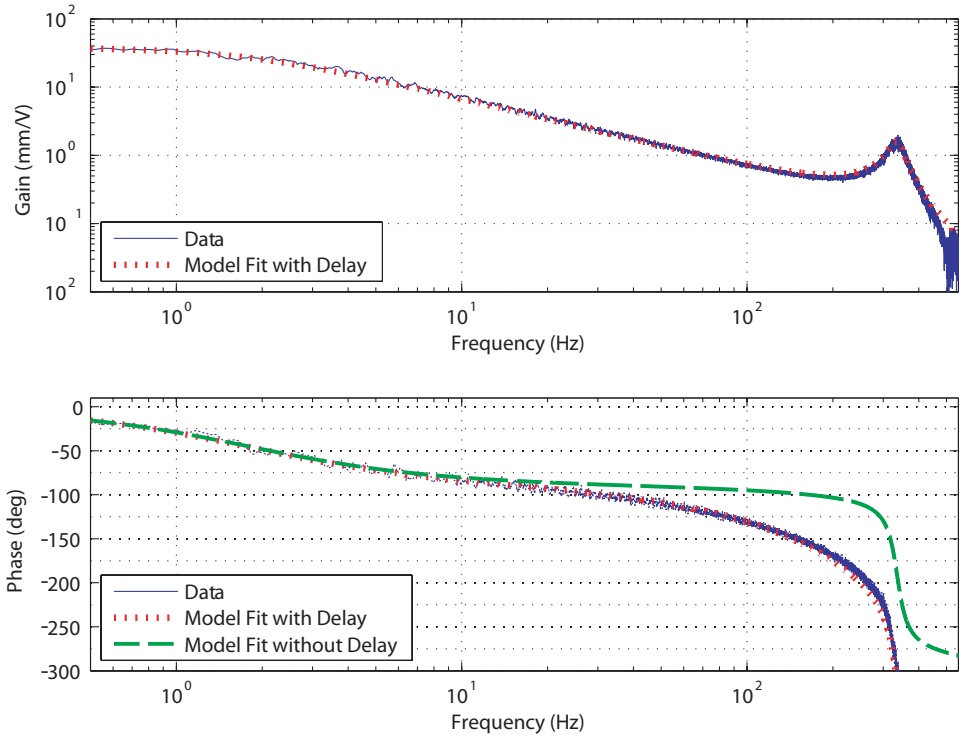

Figure 2.2: ETFE and model fit

actuators is given in the following transfer function:

$$G(z) = \frac{0.003653z^2 + 0.007306z + 0.003653}{z^8 - 2.775z^7 + 2.722z^6 - 0.9462z^5} \tag{2.3}$$

Some nonlinearity of the system is observed when varying the amplitude of the PRBS. As shown in Fig. 2.3, the ETFE generated by a 1.3 Volt PRBS has a higher resonance peak than that of the ETFE generated by a 0.9 Volts. This is consistent with the nonlinear relationship between the flowrate and the aperture size determined by the spool valve position and the presence of Coulomb friction. Since overshoot of the valve is highly undesirable as it might collide with the piston, the ETFE that has the highest resonance peak is chosen for fitting a model.

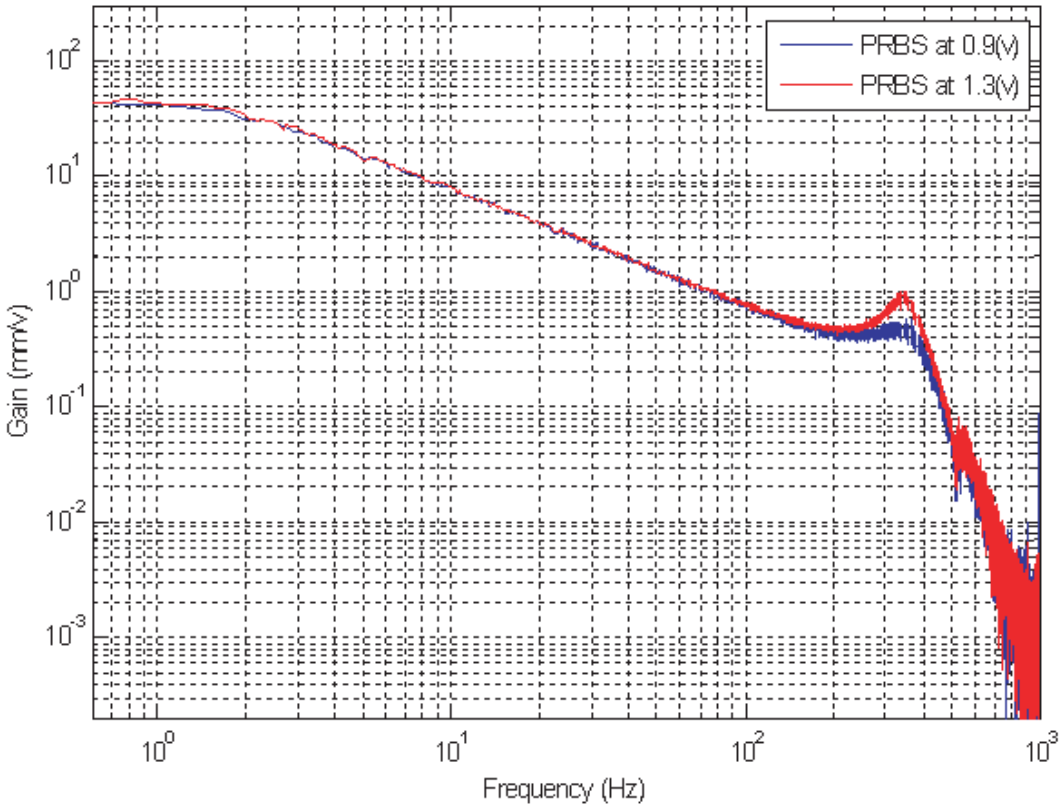

Figure 2.3: Nonlinearity in the EHVS

2.2 Feedback Controller

With a model to approximate the dynamics of the system, a model-based controller can be designed for the EHVS. To implement full-state feedback, a Kalman filter is constructed to give state estimation. The controllability and observability Gramians of the system are ill-conditioned. This is related to the fact that there is a response delay in the system and hints at a difficult control problem. Further understanding of the control challenges can be obtained by examining two simple linear feedback controllers.

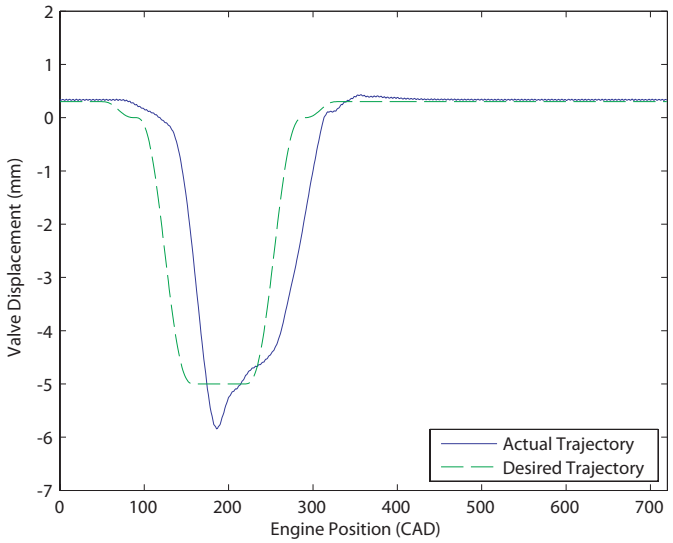

Figure 2.4: Tracking performance of the pole placement controller

2.2.1 Pole Placement Controller

The first controller designed is a pole placement controller in which the dominant second-order poles are placed with a damping ratio of 0.8. The closed-loop system is designed to be well damped because overshoot might cause the valve to collide with the engine piston and result in damage. Tracking performance is tested at an engine speed of 1800 RPM with this controller. The desired profile to be tracked has a maximum lift of 5 mm as shown in green in Fig. 2.4. The rising and falling edges of the profile are 70 crank angle degree (CAD) and translate to a rise time of 5.2 ms at 1800 RPM. The 1 ms delay is roughly twenty percent of the rise time which is not insignificant. The dwelling length at maximum lift is 60 CAD. The entire valve opening and closing event lasts 200 CAD. Note that the desired valve actuator position is set at 0.3 mm above the valve seat when the valve is closed. With this valve lash, the actuator lifts off the valve seat and ensures proper valve closure.

The test result is shown in Fig. 2.4. The response trajectory lags the desired trajectory and shows an overshoot of approximately fifteen percent. Advancing the desired profile in time can certainly solve the lagging problem, but the overshoot

characteristic is still not satisfactory even with a designed damping ratio of 0.8. The 1 ms response delay adversely impacts the phase margin of the system and, inevitably, modeling error from approximating nonlinear dynamics with a linear model gives rise to poor performance.

2.2.2 Receding Horizon Linear Quadratic Tracking Controller

The desired valve trajectory is determined at the beginning of an engine cycle by the engine control unit (ECU). The fact that the desired valve profile to be tracked is known ahead of the valve event gives extra information. The future desired trajectory also has the desired velocity and acceleration information implicit in it. Thus, one should be able to control the EHVS better if the controller is given the information of where the valve should be in the future. To that end, a quadratic cost function (2.4) based on tracking error and input is formulated with a finite horizon, N:

$$J_t = \left\{ \sum_{\tau=t}^{\tau=N+t-1} [y_{des}(\tau) - y(\tau)]^T \cdot Q \cdot [y_{des}(\tau) - y(\tau)] \quad + u(\tau)^T \cdot R \cdot u(\tau) \right\} + [y_{des}(N+t) - y(N+t)]^T Q [y_{des}(N+t) - y(N+t)] \tag{2.4}$$

where

Q is a positive scalar that weighs tracking error

R is a positive scalar that weighs control effort

N is a positive constant that defines the time horizon

For a given time step $t = \tau_1$, the cost function, J_{τ_1}, is minimized. The optimal input trajectory, $u_{opt}(\tau_1), ..., u_{opt}(\tau_1 + N - 1)$, can be solved recursively by using dynamic programming. The first element of this optimal input trajectory is applied to the system at $t = \tau_1$, i.e. $u_{opt}(\tau_1)$. At the next time step, the cost function, J_{τ_1+1}, is minimized and $u_{opt}(\tau_1+1)$ is applied to the system. Essentially, this is a receding horizon controller. The control law can be expressed as a combination of pre-calculated

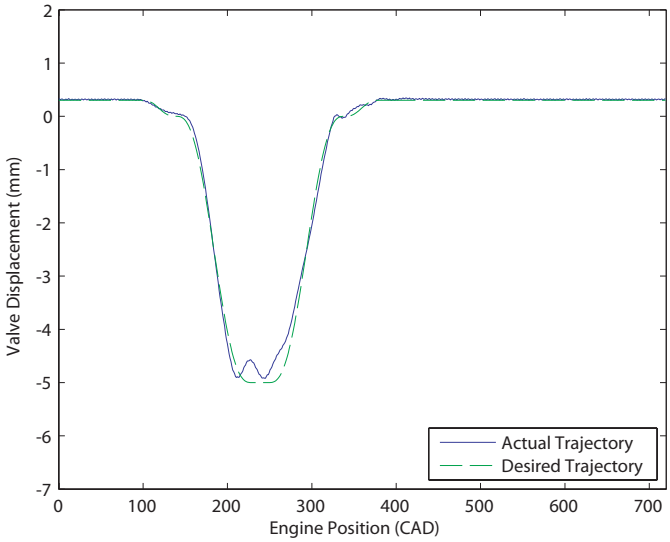

Figure 2.5: Tracking performance of the linear quadratic tracking controller

feedback and feed-forward gains as shown in Equation (2.5).

$$u(t) = N_r \cdot Y_{des}(t) - K \cdot x(t) \tag{2.5}$$

where

$Y_{des}(t) = [y_{des}(t+1) \;\; y_{des}(t+2) \;\; ... \;\; y_{des}(t+N)]^T$ is the future desired trajectory

u is the scalar optimal input

x is the system state

N_r is the feed-forward gain

K is the feedback gain

A derivation of this controller can be found in [54]. As show in Equation (2.5), for each time step, the future desired trajectory and the current states are updated and multiplied by the static gains, N_r and K, to determine the input for the system. The variables, N, Q and R, are the tuning parameters in this LQT controller formulation.

A time horizon of $N = 30$ works well with the EHVS. The ratio of Q and R is empirically determined through experiments until a satisfactory response is obtained.

A typical response with this controller is shown in Fig. 2.5 with the same desired profile defined previously in Fig. 2.4. The response of this controller is aligned with the desired trajectory in time, since the controller knows where the valve position should be in the future and is able to act proactively by taking the response delay into account. The overshoot is improved compared to the pole placement controller. However, there is still some ringing in the response.

The linear quadratic tracking controller performs better than the pole placement controller as a result of knowing the future desired trajectory. The predictive nature of the controller enables it to track the desired profile more closely. However, for both controllers, the 1 ms delay in the loop makes it very difficult to damp out the resonance mode using feedback. To put the control problem into perspective, at the resonance frequency of 350 Hz of the system, the 1 ms delay costs 126 degrees of phase. Therefore, phase margin is seriously hurt by this response delay. As a rapid prototyping tool in a research laboratory, it is desirable to further eliminate this tracking error so that the subsequent combustion research is not affected by the inconsistent valve performance.

2.3 Repetitive Controller

As shown in the previous section, using only the feedback controller is not sufficient to achieve the accurate position control offered by a mechanical cam. To further improve the tracking performance, the repeatability of the tracking error with the feedback controller is exploited. In Fig. 2.6, tracking errors from ten engine cycles are plotted. It can be seen that the tracking errors are almost identical from one cycle to the next. Based on this observation, this section presents a repetitive controller that can iteratively generates an auxiliary input to compensate for the highly repeatable tracking error using feed-forward. The concept of this repetitive controller is very similar to the iterative learning controllers proposed by Uchiyama [55], Arimoto *et al.* [56] and Casalino *et al.* [57]. These iterative learning controllers can improve the

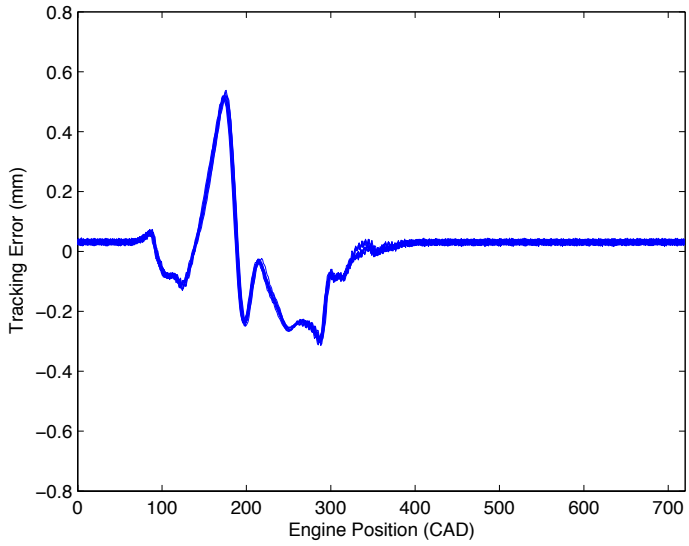

Figure 2.6: Tracking error from 10 engine cycles (over-plotted)

tracking performance of robotic manipulators by perfecting their feed-forward input through repeated trials.

The algorithm of this repetitive controller is described as follows. First, the tracking error profile is evenly partitioned into several pieces, as shown in the top plot of Fig. 2.7. Each of these partitions is referred as a *repetitive state*, and each of them has the same width in crank angle. For example, if the state width is 10 CAD, a valve opening and closing event that lasts 140 CAD consists of 14 repetitive states. Therefore, the repetitive controller is crank angle based at heart. However, the number of time samples in each repetitive state varies depending on the sampling rate and engine speed. The following equations, that express the repetitive control law, reflect this characteristic.

There are no repetitive states defined in the period where the actuator is detached from the valve, i.e., where the actuator lifts to the 0.3 mm valve lash. This is because the tracking performance during this period of operation is not important as long as the actuator stays above the valve seat. With the repetitive states defined, two properties are associated with each repetitive state: the mean tracking error and the repetitive control input. The mean tracking error of each state is computed as shown

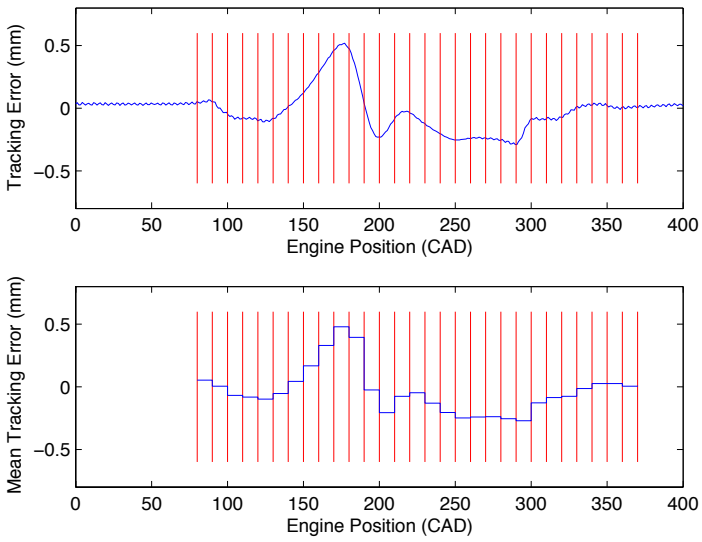

Figure 2.7: Repetitive states and mean error

in the bottom plot of Fig. 2.7. This calculation of the mean tracking error can be represented by a linear function:

$$E^{(k)} = P \cdot (\overline{y}_{des} - \overline{y}^{(k)}) \tag{2.6}$$

where

$P \in R^{m \times n}$

$E \in R^m$ is the mean error of each state

$\overline{y}_{des} \in R^n$ is the desired valve trajectory for a given cycle

$\overline{y} \in R^n$ is the actual valve trajectory for a given cycle

k represents the k^{th} engine cycle

m is the number of repetitive states

n is the number of samples that the repetitive controller covers

For example, when there are three samples within one repetitive state then the mean tracking error is simply the average of the tracking error of the three samples. In this particular case, P has the form:

$$P = \begin{bmatrix} \frac{1}{3} & \frac{1}{3} & \frac{1}{3} & 0 & 0 & 0 & \dots & 0 & 0 & 0 \\ 0 & 0 & 0 & \frac{1}{3} & \frac{1}{3} & \frac{1}{3} & \dots & 0 & 0 & 0 \\ \vdots & \vdots & \vdots & \vdots & \vdots & \vdots & \ddots & \vdots & \vdots & \vdots \\ 0 & 0 & 0 & 0 & 0 & 0 & \dots & \frac{1}{3} & \frac{1}{3} & \frac{1}{3} \end{bmatrix}$$

Note that (2.6) indicates how the tracking error in the time domain relates to the mean tracking error of each repetitive state, which is defined on a crank-angle basis. The number of columns in P, therefore, depends on the engine speed and the sampling time chosen for a particular system.

After computing the mean tracking error, the goal is to find an input that drives the mean error of each state to zero. To determine the repetitive control input for each state, the control input is updated once per engine cycle according to the following equation:

$$U_{rep}^{(k)} = U_{rep}^{(k-1)} + k_I \cdot M \cdot E^{(k-1)} \tag{2.7}$$

where

$M \in R^{m \times m}$

k_I is the integral gain

$U_{rep} \in R^m$ is the repetitive control input for each state for a given engine cycle

Note that in (2.7), U_{rep} is a vector with each of the elements representing the repetitive input to the corresponding state, and the vector is updated with respect to engine cycles. Thus U_{rep} has the same length as the number of repetitive states. The repetitive control law is specified by the M matrix as it relates the repetitive control input to the mean tracking error. In its simplest form, the M matrix can be an identity matrix and represents an integral controller which adjusts the repetitive input to each state according to the mean tracking error of that state. A slightly

more evolved example of the M matrix is shown below:

$$M = \begin{bmatrix} \frac{1}{2} & \frac{1}{2} & 0 & 0 & 0 & 0 & \dots & 0 & 0 \\ \frac{1}{3} & \frac{1}{3} & \frac{1}{3} & 0 & 0 & 0 & \dots & 0 & 0 \\ 0 & \frac{1}{3} & \frac{1}{3} & \frac{1}{3} & 0 & 0 & \dots & 0 & 0 \\ 0 & 0 & \frac{1}{3} & \frac{1}{3} & \frac{1}{3} & 0 & \dots & 0 & 0 \\ \vdots & \vdots & \vdots & \vdots & \vdots & \vdots & \ddots & \vdots & \vdots \\ 0 & 0 & 0 & 0 & 0 & 0 & \dots & \frac{1}{2} & \frac{1}{2} \end{bmatrix}$$

In this specific example, the structure of the M matrix implies that the repetitive control input for each state is a function of the error from the current state and the adjacent states. This dependency on adjacent states helps the stability of the repetitive controller.

So far this section explains how the mean tracking error and repetitive control input associated with each state are updated. In order to apply the obtained repetitive control input to the system, the vector U_{rep} needs to be converted into a vector in R^n, the domain of the system input. This can be achieved by simply using the same repetitive control input for all samples in the same state. As an example, the case with three samples per state is presented again:

$$\overline{u}_{rep}^{(k)} = S \cdot U_{rep}^{(k)} \tag{2.8}$$

where

$$S^T = \begin{bmatrix} 1 & 1 & 1 & 0 & 0 & 0 & \dots & 0 & 0 & 0 \\ 0 & 0 & 0 & 1 & 1 & 1 & \dots & 0 & 0 & 0 \\ \vdots & \vdots & \vdots & \vdots & \vdots & \vdots & \ddots & \vdots & \vdots & \vdots \\ 0 & 0 & 0 & 0 & 0 & 0 & \dots & 1 & 1 & 1 \end{bmatrix}$$

$S \in R^{n \times m}$

$\overline{u}_{rep} \in R^n$ is the repetitive control trajectory for a given engine cycle

The vector, $\overline{u}_{rep}$, is of length n and corresponds to all the samples where the repetitive states are defined. Similar to the averaging matrix P, the number of rows

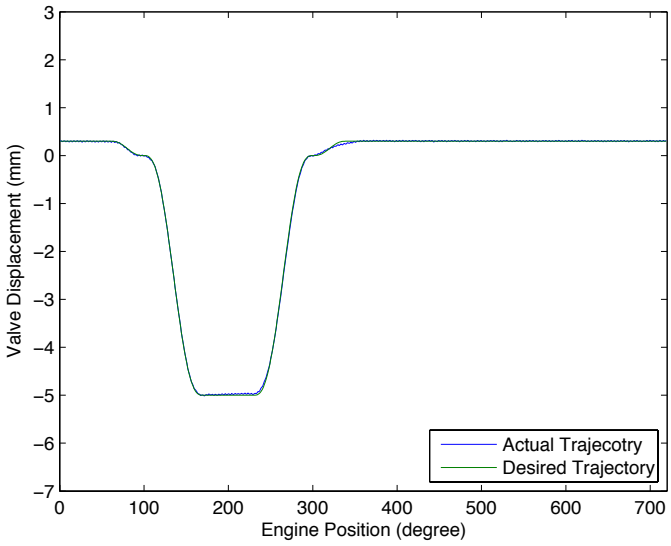

Figure 2.8: Tracking performance with the repetitive controller

of S depends on the engine speed and sampling rate as it relates the crank-angle domain to the time domain.

As a final step, this input trajectory $\overline{u}_{rep}$ is advanced in time by d time steps, 12 in this case for the particular system, to account for the response delay. The parameter d is found empirically so that the repetitive controller converges on the EHVS.

2.4 Tracking Performance: Combined Control Law

The algorithm is implemented with the same desired profile as before. The tracking performance achieved by the combination of the LQT controller and the repetitive controller is shown in Fig. 2.8. As can be seen, the tracking error with this set-up is further improved when compared to the response with only the LQT controller shown in Fig. 2.5. The maximum tracking error in Fig. 2.8 is within ± 0.08 mm.

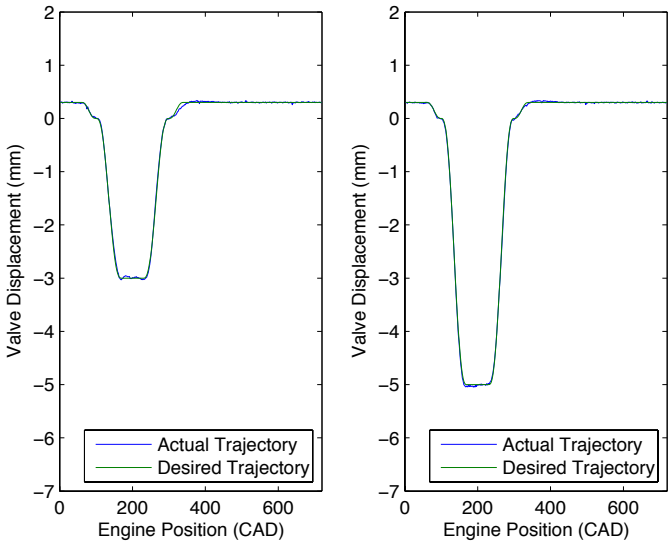

Figure 2.9: Low- and high-lift profile

2.4.1 Step Lift Change

The repetitive controller is tested in the case of switching between two different valve lifts. The two different valve lifts are 3 mm and 5 mm and are shown in blue in Fig. 2.9. These two profiles are switched every five seconds or 75 engine cycles at 1800 RPM. The steady-state tracking performance is plotted in blue in Fig. 2.9. The RMS tracking error is calculated for the period when the valve is opened in each engine cycle and is plotted in Fig. 2.10. As can be seen, the RMS tracking error jumps up every time the desired profile is switched and decays as time progresses. The higher RMS tracking error immediately after the profile change is expected, though its value of 0.12 mm is still acceptable. The repetitive controller manages to reduce the RMS error to below 0.04 mm as it learns the new input. It is possible to store the steady-state repetitive input for a desired profile in advance. Whenever that specific desired profile is needed, the corresponding repetitive input can be recalled and applied to the system. This allows any profile switch to be achieved in one engine cycle and gets around the finite time required for the repetitive controller to converge to the steady-state input.

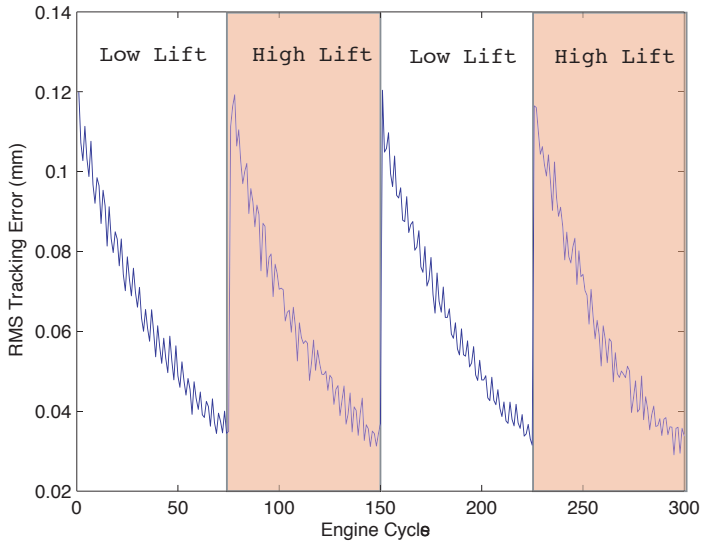

Figure 2.10: RMS tracking error for variable lift

2.4.2 Step Opening Duration Change

One immediate problem arises if one wishes to change the valve opening duration. This means that a different number of repetitive states are needed to accommodate the different opening durations. One example of such a change is shown in blue in Fig. 2.11. The valve opening timing is fixed at 100 CAD and the closing timing is varied between 300 CAD and 240 CAD. Since the difference between the two profiles is that one has a longer duration at maximum valve lift, the extra states at maximum lift are thrown away for the short-duration profile. These additional repetitive states are recalled if the long-duration profile is needed again. At 1800 RPM, a scenario where the two desired profiles are switched every 5 seconds is tested. The steady-state tracking performance is plotted in blue in Fig. 2.11. The RMS tracking error plotted in Fig. 2.12 is below 0.04 mm for all times in this experiment.

2.4.3 Engine Speed Transient

In this test, the engine speed increases from 1500 RPM to 2500 RPM in 3 s. The engine speed variation is shown in the top plot of Fig. 2.13. The corresponding RMS

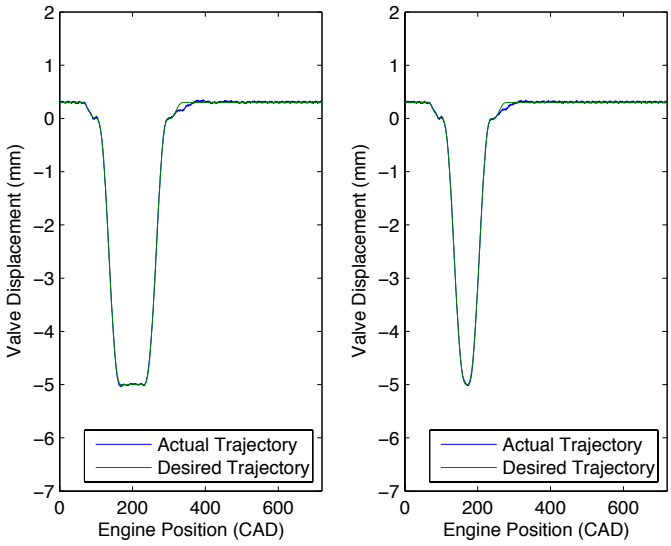

Figure 2.11: Long- and short-duration profile

tracking error is shown in the bottom plot of Fig. 2.13. As can be seen from the plot, the RMS error increases immediately when the engine speed starts to increase. After the engine speed settles, the repetitive controller learns a new input and the tracking error converges to a steady-state value under 0.04 mm. Comparable tracking performance was achieved with this controller on two additional EHVS systems with different hardware.

2.5 Stability and Mean Tracking Error Variance Analysis

To provide a solid analytical background for the tested repetitive control algorithm described in Section 2.3, a stability and a mean tracking error variance analysis are presented in this section to complete the mathematical framework for this work.

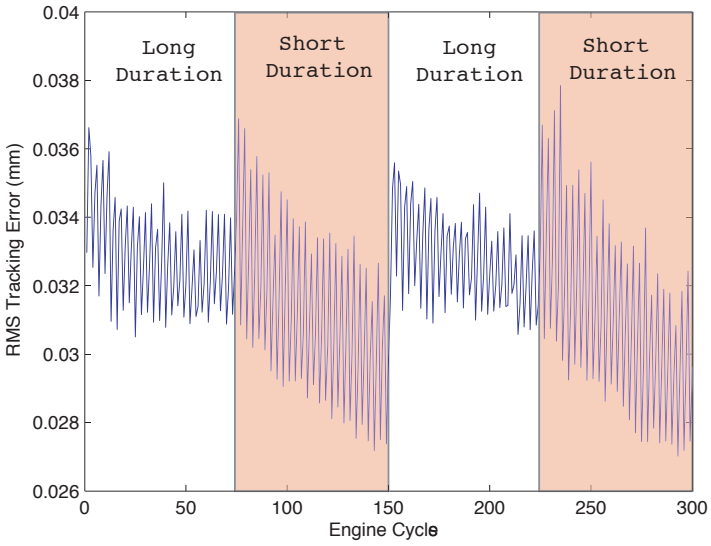

Figure 2.12: RMS tracking error for variable opening duration

2.5.1 Stability Analysis

Throughout this section, the system is assumed linear and time invariant. For clarity, the following stability analysis is derived with the pole placement controller described in Section 2.2.1. It should be noted that a similar stability analysis can be derived if one chooses to incorporate the linear quadratic tracking controller instead. The two feedback controllers in Section 2.2 differ in structure in that the LQT controller has a feed-forward that depends on the future desired trajectory. It will be demonstrated that this difference does not affect the stability criterion developed in this section.

The open-loop EHVS model can be expressed in the state space form:

$$\begin{aligned} x(t+1) &= A \cdot x(t) + B \cdot (u(t) + u_{rep}(t)) \\ y(t) &= C \cdot x(t) \end{aligned} \tag{2.9}$$

where

$x \in R^8$ are the true states

$u \in R$ is the feedback control input

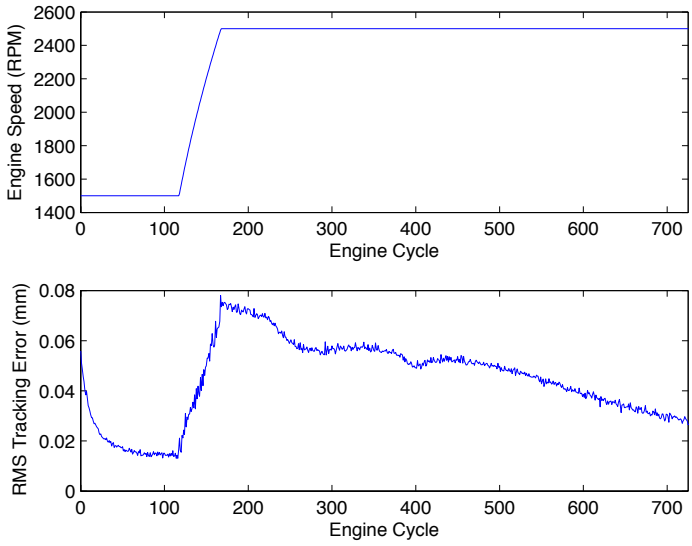

Figure 2.13: Effect of engine speed transients

$u_{rep} \in R$ is the repetitive control input

$A \in R^{8\times 8}$

$B \in R^{8}$

$C \in R^{1\times 8}$

The identified model is assumed to have the same system matrices A, B, C as the actual EHVS. Therefore, the observer has the following form:

$$\tilde{x}(t+1) = A \cdot \tilde{x}(t) + B \cdot u(t) + L \cdot (C \cdot x(t) - C \cdot \tilde{x}(t)) \tag{2.10}$$

where

$\tilde{x} \in R^{8}$ are the observed states

$L \in R^{8}$ is the observer gain

Note that the repetitive control input is not fed to the observer. This is because the feedback controller views the repetitive control input as a disturbance and tries

to reject it if the observer knows its presence. Finally, the pole placement feedback control law can be expressed as:

$$u(t) = \bar{N} \cdot y_{des}(t) - K \cdot \tilde{x}(t) \tag{2.11}$$

where

$K \in R^{1\times 8}$ is the feedback gain

$\bar{N} \in R$ is the reference input gain

Note that this control law differs from the LQT controller described in Equation (2.5) in that the LQT controller has a feed-forward dependent on the future desired trajectory. Equation (2.9), (2.10) and (2.11) can be combined to define the closed loop system dynamics:

$$\begin{aligned} \begin{bmatrix} x(t+1) \\ \tilde{x}(t+1) \end{bmatrix} &= \begin{bmatrix} A & -BK \\ LC & A - BK - LC \end{bmatrix} \cdot \begin{bmatrix} x(t) \\ \tilde{x}(t) \end{bmatrix} \\ &\quad + \begin{bmatrix} B\bar{N} \\ B\bar{N} \end{bmatrix} \cdot y_{des}(t) + \begin{bmatrix} B \\ \mathbf{0} \end{bmatrix} \cdot u_{rep}(t) \\ y(t) &= \begin{bmatrix} C & \mathbf{0} \end{bmatrix} \cdot \begin{bmatrix} x(t) \\ \tilde{x}(t) \end{bmatrix} \end{aligned} \tag{2.12}$$

To simplify the notation, the following matrices and vectors are defined:

$$\begin{aligned}
\hat{A} &= \begin{bmatrix} A & -BK \\ LC & A-BK-LC \end{bmatrix} \\
\hat{B}_1 &= \begin{bmatrix} B\bar{N} \\ B\bar{N} \end{bmatrix} \\
\hat{B}_2 &= \begin{bmatrix} B \\ \mathbf{0} \end{bmatrix} \\
\hat{C} &= \begin{bmatrix} C & \mathbf{0} \end{bmatrix} \\
\hat{x}(t) &= \begin{bmatrix} x(t) \\ \tilde{x}(t) \end{bmatrix}
\end{aligned} \tag{2.13}$$

The closed loop system can therefore be expressed as follows:

$$\begin{aligned}
\hat{x}(t+1) &= \hat{A}\cdot\hat{x}(t) + \hat{B}_1\cdot y_{des}(t) + \hat{B}_2\cdot u_{rep}(t) \\
y(t) &= \hat{C}\cdot\hat{x}(t)
\end{aligned} \tag{2.14}$$

With the closed loop system established, the trajectory of the system output can be related to the initial conditions and the input trajectories with Toeplitz matrices. To analyze the stability of the repetitive control algorithm, the system output for the n time steps where the repetitive states are defined in engine cycle k is shown below.

$$\overline{y}^{(k)} = T_1\cdot\overline{y}_{des} + T_2\cdot\overline{u}_{rep}^{(k)} \tag{2.15}$$

where

$$T_1 = \begin{bmatrix} 0 & 0 & \dots & 0 \\ \hat{C}\hat{B}_1 & 0 & \dots & 0 \\ \vdots & \vdots & \ddots & \vdots \\ \hat{C}\hat{A}^{n-2}\hat{B}_1 & \hat{C}\hat{A}^{n-3}\hat{B}_1 & \dots & 0 \end{bmatrix}$$

$$T_2 = \begin{bmatrix} \hat{C}\hat{A}^{d-1}\hat{B}_2 & \hat{C}\hat{A}^{d-2}\hat{B}_2 & \dots & 0 \\ \hat{C}\hat{A}^{d}\hat{B}_2 & \hat{C}\hat{A}^{d-1}\hat{B}_2 & \dots & 0 \\ \vdots & \vdots & \ddots & \vdots \\ \hat{C}\hat{A}^{n+d-2}\hat{B}_2 & \hat{C}\hat{A}^{n+d-3}\hat{B}_2 & \dots & \hat{C}\hat{A}^{d-1}\hat{B}_2 \end{bmatrix}$$

$$\overline{y} = \begin{bmatrix} y(t+1) & \dots & y(t+n) \end{bmatrix}^T$$

$$\overline{y}_{des} = \begin{bmatrix} y_{des}(t+1) & \dots & y_{des}(t+n) \end{bmatrix}^T$$

$$\overline{u}_{rep} = \begin{bmatrix} u_{rep}(t+1-d) & \dots & u_{rep}(t+n-d) \end{bmatrix}^T$$

If the LQT controller is chosen in this derivation in place of the pole placement controller, T_1 would have a different structure but T_2 maintains the same structure.

Assuming steady state operation where the desired valve trajectory is fixed from cycle to cycle, $\overline{y}_{des}$ does not change from one cycle to the next. Note that the repetitive control input is advanced in time by d time steps, as pointed out in the last paragraph of Section 2.3. The initial conditions are neglected in the equation since they do not affect the following stability analysis as long as they stay unchanged from one engine cycle to the next. This is a fair assumption since the engine valves stay closed for a large portion of the time in one engine cycle. Therefore, any transients of EHVS after valve closure have sufficient time to die out before the next valve opening event. As a result, when considering the output trajectory of these n time steps, the system can be safely assumed to start from the same initial conditions from cycle to cycle.

To establish the stability of the repetitive controller, the same algorithm and notations described in Section 2.3 is followed. Combining Equation (2.7) and Equation (2.8) gives the following expression that represents the repetitive control law in the time domain:

$$\overline{u}_{rep}^{(k)} = \overline{u}_{rep}^{(k-1)} + k_I \cdot S \cdot M \cdot E^{(k-1)} \tag{2.16}$$

Substituting Equation (2.16) into Equation (2.15) gives:

$$\overline{y}^{(k)} = T_1 \cdot \overline{y}_{des} + T_2 \cdot \overline{u}_{rep}^{(k-1)} + k_I \cdot T_2 \cdot S \cdot M \cdot E^{(k-1)} \tag{2.17}$$

Note that the first two terms on the right hand side of Equation (2.17) can be combined to be $\overline{y}^{(k-1)}$ using (2.15). This gives:

$$\overline{y}^{(k)} = \overline{y}^{(k-1)} + k_I \cdot T_2 \cdot S \cdot M \cdot E^{(k-1)} \tag{2.18}$$

It should be clear at this point that if the LQT controller is used in this derivation in place of the pole placement controller, Equation (2.18) remains the same. This is because introducing the LQT controller only changes T_1 in (2.17) and does not affect the result shown in (2.18). The stability proof, therefore, does not depend on which feedback controller is incorporated into the analysis.

To look at how mean tracking error propagates, recall that $E^{(k)} = P \cdot (\overline{y}_{des} - \overline{y}^{(k)})$. So with Equation (2.18):

$$\begin{aligned} E^{(k)} &= P \cdot (\overline{y}_{des} - \overline{y}^{(k)}) \\ &= P \cdot (\overline{y}_{des} - \overline{y}^{(k-1)}) - k_I \cdot P \cdot T_2 \cdot S \cdot M \cdot E^{(k-1)} \end{aligned} \tag{2.19}$$

Noting that the first term on the right hand side of Equation (2.19) is just $E^{(k-1)}$. This gives:

$$\begin{aligned} E^{(k)} &= E^{(k-1)} - k_I \cdot P \cdot T_2 \cdot S \cdot M \cdot E^{(k-1)} \\ &= (I - k_I \cdot P \cdot T_2 \cdot S \cdot M) \cdot E^{(k-1)} \end{aligned} \tag{2.20}$$

Further defining $A_E = I - k_I \cdot P \cdot T_2 \cdot S \cdot M$ to simplifies the notation gives:

$$E^{(k)} = A_E \cdot E^{(k-1)} \tag{2.21}$$

Equation (2.21) relates the mean tracking error of the previous engine cycle to the current cycle. Essentially, A_E describes the error dynamics of the system. Therefore, the mean tracking error approaches zero asymptotically if the eigenvalues of A_E satisfy the following condition:

$$|\lambda_i(A_E)| < 1, \quad \forall i = 1, 2, \ldots, m \tag{2.22}$$

This condition states that if all the eigenvalues of A_E lies within the unit circle on the complex plane then the mean tracking error converges to zero asymptotically. Using this formulation and the parameters of the EHVS, it is verified analytically that the mean tracking error indeed converges to zero. The eigenvalues of A_E can also serve as a quantitative metric to compare different repetitive controller designs, since they relate directly to the rate of convergence of the system.

2.5.2 Tracking Error Variance Analysis

In a more realistic setting, the LVDT measurements inevitably have some sensor noise characteristics. The mean tracking error in this case is a function of the random sensor noise and, therefore, is a random variable itself. It is desirable to know the variance of the steady-state mean tracking error if the sensor noise characteristics are given, since it establishes confidence bounds on the steady-state mean tracking error. Of course, the system can in reality exhibit more variation compared to the analysis in this section. For example, un-modeled dynamics that are certainly present in any real world application can potentially make the actual tracking error variance exceed the predictions in this section. However, given the sensor noise characteristics, the bound presented in this section can serve as a best-case scenario that one can hope to achieve with the EHVS. If this optimistic bound is deemed too great to be acceptable, there are potential design changes on the system that are necessary.

In the following analysis, the valve trajectory that the LVDT measures is assumed to be corrupted by a zero-mean Gaussian noise with covariance Σ_w. Furthermore, it is assumed that the measurement noise of two different engine cycles is independent and identically distributed (IID). This analysis starts from Equation (2.15) and follows the same derivation shown previously with the addition of the measurement noise to

the equation:

$$\begin{aligned}
\overline{y}^{(k)} &= T_1\overline{y}_{des} + T_2\overline{u}_{rep}^{(k)} + w^{(k)} \\
&= T_1\overline{y}_{des} + T_2\overline{u}_{rep}^{(k-1)} + k_I T_2 SME^{(k-1)} + w^{(k)} \\
&= \overline{y}^{(k-1)} + k_I T_2 SME^{(k-1)} + w^{(k)} - w^{(k-1)} \\
&= \overline{y}^{(k-1)} + k_I T_2 SME^{(k-1)} - v^{(k)} \qquad (2.23)
\end{aligned}$$

where

$\Sigma_w \in R^{n\times n}$ and is symmetric and positive definite

$w \sim N(0, \Sigma_w)$

$v^{(k)} = w^{(k-1)} - w^{(k)}$

Recall that $E^{(k)} = P \cdot (\overline{y}_{des} - \overline{y}^{(k)})$, one can perform the same operations as shown in Equation (2.19) on Equation (2.23). This gives an expression that is similar to Equation (2.21):

$$E^{(k)} = A_E \cdot E^{(k-1)} + P \cdot v^{(k)} \qquad (2.24)$$

Back-propagating the error dynamics gives the following equation:

$$E^{(k)} = A_E^k \cdot E^{(0)} + \sum_{i=0}^{k-1} A_E^i \cdot P \cdot v^{(k-i)} \qquad (2.25)$$

To find out the steady-state mean tracking error variance, let k approach infinity and look at the covariance of $E^{(k)}$:

$$Cov(\lim_{k\to\infty} E^{(k)}) = Cov(\lim_{k\to\infty} A_E^k \cdot E^{(0)} + \sum_{i=0}^{k-1} A_E^i \cdot P \cdot v^{(k-i)}) \qquad (2.26)$$

The error dynamics given by A_E are assumed stable here; therefore, the first term of Equation (2.26) vanishes when the limit is taken to infinity. This gives:

$$Cov(\lim_{k\to\infty} E^{(k)}) = Cov(\lim_{k\to\infty} \sum_{i=0}^{k-1} A_E^i \cdot P \cdot v^{(k-i)}) \qquad (2.27)$$

Expanding the right side of Equation (2.27) requires the knowledge of how $v^{(i)}$ correlates with $v^{(j)}$ for all i, j. To that end, $v^{(k)}$, $v^{(k-1)}$ and $v^{(k-2)}$ are expressed as functions of $w^{(k)}$, $w^{(k-1)}$, $w^{(k-2)}$ and $w^{(k-3)}$:

$$\begin{bmatrix} v^{(k-2)} \\ v^{(k-1)} \\ v^{(k)} \end{bmatrix} = \begin{bmatrix} 1 & -1 & 0 & 0 \\ 0 & 1 & -1 & 0 \\ 0 & 0 & 1 & -1 \end{bmatrix} \begin{bmatrix} w^{(k-3)} \\ w^{(k-2)} \\ w^{(k-1)} \\ w^{(k)} \end{bmatrix} \tag{2.28}$$

Obvious from the above equation, $v^{(k)}$ is correlated to $v^{(k-1)}$ but not correlated to $v^{(k-2)}$. Since the $w^{(k)}$ are zero-mean IID Gaussian random variables with variance Σ_w, the distribution of the random vector $[v^{(k-2)} \quad v^{(k-1)} \quad v^{(k)}]^T$ can be expressed as:

$$\begin{bmatrix} v^{(k-2)} \\ v^{(k-1)} \\ v^{(k)} \end{bmatrix} \sim N(0, \Sigma_v) \tag{2.29}$$

where

$$\Sigma_v = \begin{bmatrix} 2\Sigma_w & -\Sigma_w & 0 \\ -\Sigma_w & 2\Sigma_w & -\Sigma_w \\ 0 & -\Sigma_w & 2\Sigma_w \end{bmatrix}$$

With this example, one can conclude the expected value of $v^{(i)} \cdot (v^{(j)})^T$ is:

$$\mathbf{E}[v^{(i)} \cdot (v^{(j)})^T] = \begin{cases} 2\Sigma_w & , \quad if \;\; i-j=0 \\ -\Sigma_w & , \quad if \;\; |i-j|=1 \\ 0 & , \quad if \;\; |i-j| \geq 2 \end{cases} \tag{2.30}$$

Since the $v^{(i)}$ are zero-mean, Equation (2.27) becomes:

$$\begin{aligned} Cov(\lim_{k\to\infty} E^{(k)}) &= Cov(\lim_{k\to\infty} \sum_{i=0}^{k-1} A_E^i \cdot P \cdot v^{(k-i)}) \\ = \quad \mathbf{E}[\lim_{k\to\infty} \sum_{i=0}^{k-1} \sum_{j=0}^{k-1} A_E^i \cdot P \cdot v^{(k-i)} \cdot (A_E^j \cdot P \cdot v^{(k-j)})^T] \end{aligned} \tag{2.31}$$

Using the knowledge that $v^{(i-n)}$ is uncorrelated to $v^{(i)}$ when $|n| \geq 2$, Equation (2.31) can be expressed as:

$$\begin{aligned} & Cov(\lim_{k\to\infty} E^{(k)}) \\ & = \mathbf{E}[\lim_{k\to\infty} \sum_{i=0}^{k-1} A_E^i \cdot P \cdot v^{(k-i)} \cdot (A_E^i \cdot P \cdot v^{(k-i)})^T \\ & \quad + \sum_{i=0}^{k-1} A_E^{i+1} \cdot P \cdot v^{(k-i-1)} \cdot (A_E^i \cdot P \cdot v^{(k-i)})^T \\ & \quad + \sum_{i=0}^{k-1} A_E^i \cdot P \cdot v^{(k-i)} \cdot (A_E^{i+1} \cdot P \cdot v^{(k-i-1)})^T] \end{aligned} \tag{2.32}$$

Finally, using the relations in Equation (2.30) gives the following:

$$Cov(\lim_{k\to\infty} E^{(k)}) = 2 \cdot \Sigma - A_E \cdot \Sigma - \Sigma \cdot A_E^T \tag{2.33}$$

where

$$\Sigma = \sum_{i=0}^{\infty} A_E^i \cdot P \cdot \Sigma_w \cdot P^T \cdot (A_E^T)^i$$

Since A_E is stable, the infinite sum that defines Σ converges. Furthermore, Σ satisfies the following Lyapunov equation:

$$A_E \cdot \Sigma \cdot A_E^T = \Sigma - P \cdot \Sigma_w \cdot P^T \tag{2.34}$$

Once the sensor noise covariance Σ_w is characterized, one can solve Equation (2.34) for Σ and use (2.33) to calculate the steady-state mean tracking error covariance. With this covariance matrix, a confidence bound on the steady-state mean tracking error can be established.

2.6 Conclusion

An EHVS gives researchers the capability to quickly implement and validate new valve strategies on an internal combustion engine. However, the benefits of using this powerful rapid prototyping tool can only be reaped if the valve motion is accurately controlled. This chapter shows that the dynamics of an EHVS can be well approximated by a third-order linear model with input delay. It is also shown that the tracking performance with feedback controllers is inadequate due to this response delay. To ensure accurate valve motion in a research laboratory setting, the proposed repetitive control algorithm is demonstrated to be very effective for further improving the tracking performance.

The repetitive controller generates an auxiliary input adaptively based on the valve tracking error of each engine cycle. With this auxiliary input augmenting the feedback controllers, steady-state RMS tracking errors under 40 μm for various different desired valve profiles are achieved. Besides excellent tracking performance, the adaptive nature of the repetitive control algorithm can readily handle system parameter drifts as an EHVS warms up during operation.

The simple repetitive control algorithm proposed is not only observed to be stable in experiments but also proven analytically. Furthermore, the mathematical framework developed can be extended to include sensor noise characteristics that lead to confidence bounds on steady-state mean tracking errors. The methodology described in this chapter that includes system identification, feedback control design and repetitive control design has been proven to work well on multiple EHVSs with different hardware.

Chapter 3

The Nonlinear Model

From Chapter 3 onwards, this thesis shifts its focus from the EHVS to recompression HCCI. The work presented in this thesis uses the control-oriented, single-zone model developed by Ravi *et al.* [58] as a launching point. In this chapter, a summary of the model and some of its equations are given. Throughout this thesis, this model is referred to as the nonlinear model or simply as the NL. The nonlinear model captures the cycle-to-cycle dynamics of recompression HCCI as shown in [58] and is able to reflect how various inputs influence the combustion timing of HCCI. However, for the purpose of this thesis, the exhaust valve closure (EVC) point is chosen as the only input to the system and it captures the amount of exhaust trapped in the cylinder, which initiates HCCI on the *next* engine cycle. The model output, the combustion timing, is represented by the engine position where fifty percent fuel energy conversion occurs, denoted as θ_{50}.

3.1 Summary of the Nonlinear Model

The start of an engine cycle in the nonlinear model is defined at 300 CAD referenced from recompression TDC. In-cylinder oxygen content and temperature at 300 CAD are chosen as the system states. The choice of this particular engine position is motivated by the fact that 300 CAD is a point after the breathing process, therefore, the air-fuel charge is fixed in its composition. There are seven points defined at seven

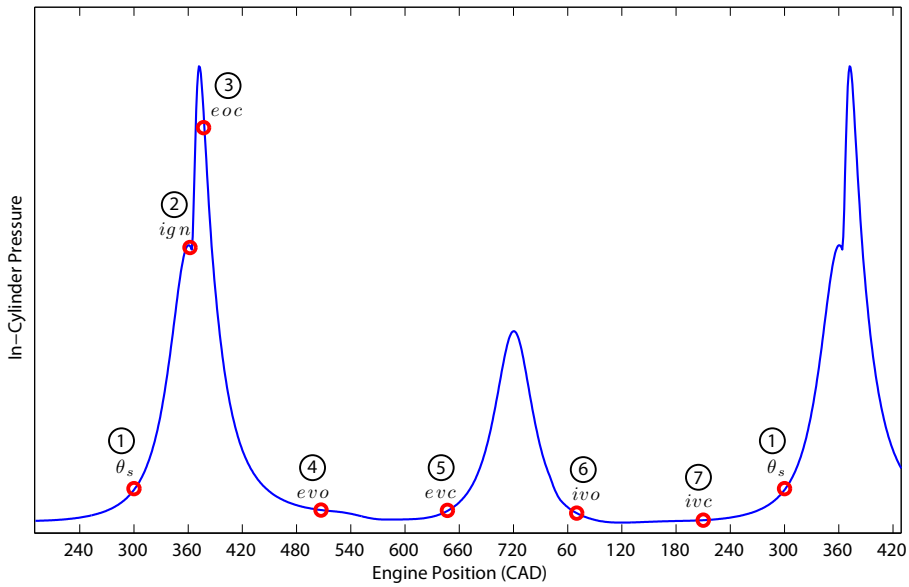

Figure 3.1: The seven breakpoints of the nonlinear model in an engine cycle

distinct engine positions in a cycle and they are listed below:

Point 1: State definition point at 300 CAD (θ_s)

Point 2: Ignition (ign)

Point 3: End of combustion (eoc)

Point 4: Exhaust valve opening (evo)

Point 5: Exhaust valve closure (evc)

Point 6: Intake valve opening (ivo)

Point 7: Intake valve closure (ivc)

The shorthand notations in the parantheses are used to refer to these distinct engine positions. These breakpoints are illustrated in Fig. 3.1 along with a typical pressure trace. There are six variables in the model equations that are directly related to the thermo-chemical conditions of the in-cylinder gas. These are listed below:

n : Total number of moles in the cylinder

p : In-cylinder pressure

T : In-cylinder temperature

V : Cylinder volume

n^{O_2} : Number of moles of oxygen in the cylinder

n^f : Number of moles of gasoline in the cylinder

The first four variables specify the thermodynamic states of the in-cylinder gas. Note that knowing three of these four variables is sufficient to completely describe the thermodynamic states of the in-cylinder gas, as the remaining unknown variable can be calculated based on the ideal gas law assumption. The last two variables, n^{O_2} and n^f are associated with the chemical conditions of the in-cylinder gas. Other variables that appear in the model equations are parameters for describing environmental conditions or engine characteristics. The six thermo-chemical variables listed above can be further given subscripts to specify the thermo-chemical conditions at a particular engine position. For example, V_{evc} is the cylinder volume at the exhaust valve closure point and p_{θ_s} is the pressure at the state definition point. Therefore, the states, x, of the nonlinear model are defined as:

$$x = \begin{bmatrix} n_{\theta_s}^{O_2} \\ T_{\theta_s} \end{bmatrix} \tag{3.1}$$

There are mainly two reasons that motivate the choice of system states shown in Equation (3.1). Firstly, the temperature state, T_{θ_s}, in Equation (3.1) is representative of the thermodynamic conditions of the in-cylinder gas. This is because the gas pressure at the state definition point is assumed constant in this model, and the cylinder volume at 300 CAD is known. Therefore the temperature state, T_{θ_s}, completes the description of the thermodynamic states of the in-cylinder gas at the state definition point. Secondly, the two physical quantities, oxygen content and temperature, defining the system states can be related to ignition timing using an Arrhenius

global reaction rate model shown in Equation (3.2), as described by Shaver [59]. The reaction rate is the integrand shown in (3.2), which is exponentially dependent on the in-cylinder temperature, and proportional to powers of the oxygen and fuel concentration. In this model, ignition is defined as the instance when the value of this integral exceeds a threshold K_{th}.

$$\theta_{ign} = \left\{ \theta_\tau \;\middle|\; K_{th} = \int_{\theta_s}^{\theta_\tau} A \cdot e^{\frac{-E_a}{R \cdot T_\theta}} \cdot [n_{\theta_s}^{O_2}]^a \cdot [n_{\theta_s}^{f}]^b \cdot \frac{1}{\omega} \mathrm{d}\theta \right\} \tag{3.2}$$

where

θ is the engine position

ω is the engine speed

T_θ is the in-cylinder temperature as a function of the engine position θ

$\left[n_{\theta_s}^{O_2}\right]$ is the oxygen concentration, inversely proportional to the cylinder volume

$\left[n^f\right]$ is the fuel concentration, inversely proportional to the cylinder volume

The model output, θ_{50}, is further defined as one-half of the combustion duration after the ignition point:

$$\theta_{50}(k) = \theta_{ign}(k) + 0.5 \cdot \theta^{durn} \tag{3.3}$$

where θ^{durn} is the combustion duration.

The combustion timing of HCCI, θ_{50}, is therefore dependent on the in-cylinder temperature, oxygen concentration and fuel concentration, in descending order of their relative sensitivity. Note that the Arrhenius model defines the second breakpoint, the ignition point, in a cycle, which is an implicit function of the states as can be seen in Equation (3.2). Combining (3.2) and (3.3) gives a nonlinear output equation that relates the system states to the output:

$$\theta_{50}(k) = h\big(n_{\theta_s}^{O_2}(k), T_{\theta_s}(k)\big) \tag{3.4}$$

The seven breakpoints define seven cascading stages in an engine cycle as listed below:

Stage 1: Polytropic compression from 300 CAD to autoignition

Stage 2: Constant-duration combustion

Stage 3: Polytropic expansion from EOC to EVO

Stage 4: Polytropic blowdown and exhaust from EVO to EVC

Stage 5: Recompression from EVC to IVC

Stage 6: Adiabatic induction from IVO to IVC

Stage 7: Polytropic compression from IVC to 300 CAD on the *next* engine cycle

Seven sub-models propagate the two system states from the start of a stage to the end of a stage based on simple thermodynamic assumptions. These seven sub-models are summarized briefly in this chapter. The derivation of these sub-models is given in Appendix A.

Stage 1: Polytropic compression from 300 CAD to ignition

$$n_{ign}^{O_2}(k) = n_{\theta_s}^{O_2}(k) \tag{3.5}$$

$$T_{ign}(k) = T_{\theta_s}(k) \cdot \left(\frac{V_{\theta_s}}{V_{ign}(k)} \right)^{\kappa_1 - 1} \tag{3.6}$$

The end of this stage is defined by the ignition point shown in Equation (3.2). Note that due to the use of the Arrhenius integral, θ_{ign} cannot be expressed as an explicit function of the states. It is, however, easy to simulate the resulting θ_{ign} given the values of oxygen content and temperature at the state definition point. The parameter, κ_1, is the polytropic exponent associated with **Stage 1**, and is assumed constant during this stage. Using this convention, κ_i represents the polytropic exponent for **Stage** i.

Stage 2: Constant-duration combustion from ignition to end of combustion

$$n_{eoc}^{O_2}(k) = n_{ign}^{O_2}(k) - \lambda_{stoich} \cdot n_{\theta_s}^{f} \tag{3.7}$$

$$T_{eoc}(k) = T_{ign}(k) \cdot \left(\frac{V_{ign}(k)}{V_{eoc}(k)}\right)^{\kappa_2 - 1} + \frac{E \cdot n_{\theta_s}^{f}}{(C_{v,f} - C_v) \cdot n_{\theta_s}^{f} + C_v \cdot n_{\theta_s}(k)} \tag{3.8}$$

where

$\theta_{eoc}(k) = \theta_{ign}(k) + \theta^{durn}$

$E = (1 - \epsilon) \cdot LHV_f + (3.25 \cdot C_v - C_{v,f}) \cdot T^{amb}$

λ_{stoich} is the stoichiometric oxygen-fuel ratio

The combustion process has a constant duration defined by θ^{durn}. Energy conversion from fuel oxidation is modelled as instantaneous at the end-of-combustion point. The amount of energy per unit fuel quantity, E, added to cylinder constituents is given above. The variable ϵ in the expression of E accounts for the heat transfer during combustion as a portion of the lower heat value (LHV) of the fuel. The term $(3.25 \cdot C_v - C_{v,f}) \cdot T^{amb}$ in the expression is the results of accounting for the change in the total number of moles and the average specific heat before and after a lean combustion. The variable, T^{amb}, is the ambient temperature that serves as the reference temperature in the first law analysis. The denominator of the second term in Equation (3.8) represents the product of the average specific heat of the in-cylinder gas and the total amount of gas in the cylinder. A lean mixture is assumed; therefore the oxygen content after combustion is given in Equation (3.7).

Stage 3: Polytropic expansion from EOC to EVO

$$n_{evo}^{O_2}(k) = n_{eoc}^{O_2}(k) \tag{3.9}$$

$$T_{evo}(k) = T_{evc}(k) \cdot \left(\frac{V_{eoc}(k)}{V_{evo}(k)}\right)^{\kappa_3 - 1} \tag{3.10}$$

The expansion after combustion is modelled as a polytropic process.

Stage 4: Polytropic blowdown and exhaust from EVO to EVC

$$n_{evc}^{O_2}(k) = n_{evo}^{O_2}(k) \cdot \frac{n_{evc}(k)}{n_{evo}(k)} \tag{3.11}$$

$$T_{evc}(k) = T_{evo}(k) \cdot \left(\frac{p^{em}}{p_{evo}(k)} \right)^{1-\frac{1}{\kappa_4}} \tag{3.12}$$

where

$n_{evo}(k) = n_{eoc}(k) = n_{ign}(k) = n_{\theta_s}(k)$

$n_{evc}(k) = \frac{p^{em} \cdot V_{evc}(k)}{R \cdot T_{evc}(k)}$

$p_{evo}(k) = p_{eoc}(k) \cdot \left(\frac{V_{evo}(k)}{V_{ign}(k)} \right)^{\kappa_2}$

p^{em} is the exhaust manifold pressure.

The ratio between n_{evc} and n_{evo} seen in Equation (3.11) is the percentage of exhaust trapped in the cylinder at EVC. This ratio is, of course, a strong function of the EVC timing and is typically in the range of 0.5∼0.6 for recompression HCCI. Furthermore, the total number of moles of gas in the cylinder is assumed unchanged before and after combustion. The in-cylinder pressure at EVC is assumed to be equal to the exhaust manifold pressure, p^{em}.

Stage 5: Recompression from EVC to IVO

$$n_{ivo}^{O_2}(k) = n_{evc}^{O_2}(k) \tag{3.13}$$

$$T_{ivo}(k) = T_{evc}(k) - \frac{h}{n_{ivo}(k) \cdot C_v} \cdot \left(\frac{1}{2} \cdot T_{evc} \cdot \left(1 + \left(\frac{V_{evc}(k)}{V^{tdc}} \right)^{\gamma-1} \right) - T^{wall} \right) \tag{3.14}$$

where

$n_{ivo}(k) = n_{evc}(k)$

h is a lumped heat transfer parameter.

The variable γ in Equation (3.14) is the specific heat ratio of air. Therefore, the term $\frac{1}{2} \cdot T_{evc} \cdot \left(1 + \left(\frac{V_{evc}(k)}{V^{tdc}}\right)^{\gamma-1}\right)$ in Equation (3.14) is a measure of the average, isentropic temperature during recompression. The amount of heat transfer during recompression is modelled as proportional to the difference between the average in-cylinder temperature and cylinder wall temperature. Equation (3.14) provides a simple construct to capture the effect of cylinder wall temperature on the system states.

Stage 6: Adiabatic induction from IVO to IVC

$$n_{ivc}^{O_2}(k) = n_{ivo}^{O_2}(k) + \chi \cdot n^{ind}(k) \tag{3.15}$$

$$T_{ivc}(k) = \frac{p^{im} \cdot V_{ivc}(k)}{R \cdot (n_{ivo}(k) + n^{ind}(k))} \tag{3.16}$$

where

$n^{ind}(k) = \frac{C_v}{C_p \cdot R \cdot T^{im}} \cdot (p^{im} \cdot V_{ivc} - n_{ivo}(k) \cdot R \cdot T_{ivo}(k))$

p^{im} is the intake manifold pressure.

The amount of fresh air inducted, n^{ind}, multiplied by the molar concentration of oxygen in air (around 0.2), χ, gives the increase in the oxygen content at IVC. The pressure at IVC is assumed to be equal to the intake manifold pressure p^{im}. The total amount of gas at IVC, the sum of n^{ind} and n_{ivo}, determines the temperature at IVC based on the ideal gas law.

Stage 7: Polytropic compression from IVC to θ_s

$$n_{\theta_s}^{O_2}(k+1) = n_{ivc}^{O_2}(k) \tag{3.17}$$

$$T_{\theta_s}(k+1) = T_{ivc}(k) \cdot \left(\frac{V_{ivc}}{V_{\theta_s}}\right)^{\kappa_7 - 1} \tag{3.18}$$

The system states on the *next* engine cycle can be propagated from IVC with a polytropic process. Note that the gas pressure at the state definition point, p_{θ_s}, can

be obtained with the polytropic process:

$$p_{\theta_s}(k+1) = p_{ivc}(k) \cdot \left(\frac{V_{ivc}(k)}{V_{\theta_s}}\right)^{\kappa_7} = p^{im} \cdot \left(\frac{V_{ivc}(k)}{V_{\theta_s}}\right)^{\kappa_7}$$

Since $p_{ivc} = p^{im}$, the pressure at the state definition point is constant given a fixed intake manifold pressure.

The composition of these seven sub-models, therefore, gives a cycle-by-cycle model. The propagation of states from one cycle to the next can be summarized by two nonlinear equations:

$$\begin{aligned} n_{\theta_s}^{O_2}(k+1) &= f\left(n_{\theta_s}^{O_2}(k), T_{\theta_s}(k), V_{evc}(k)\right) \\ T_{\theta_s}(k+1) &= g(n_{\theta_s}^{O_2}(k), T_{\theta_s}(k), V_{evc}(k)) \end{aligned} \tag{3.19}$$

Equation (3.4) and Equations (3.19) combined describe a discrete-time, single-input-single-output, nonlinear dynamical system.

This nonlinear model captures the cycle-to-cycle dynamics of recompression HCCI as shown in [58], and its relative simplicity makes the analysis and control synthesis presented in this thesis tractable. While the NL is tuned to the particular experimental testbed used in this thesis, its physics-based nature could potentially make the insight shown in Chapter 4∼7 applicable to other recompression HCCI engines.

Chapter 4

Change in Recompression HCCI Dynamics

Arguably, two of the most important control objectives for IC engines are the work output and combustion timing. The work output of an HCCI engine is largely a function of the amount of fuel [59, 60] in the cylinder, assuming complete combustion of fuel and that ignition occurs at the designated timing. Therefore, control of combustion timing is, in some sense, the more fundamental problem in HCCI control. As outlined in Chapter 1, residual-affected HCCI presents several challenges in controlling its combustion timing, i.e., the lack of direct ignition trigger, cycle-to-cycle coupling, and drastic change in system dynamics. Particularly, the change in system dynamics compounds the first two challenges when one wishes to operate HCCI over a wide range.

The change in recompression HCCI dynamics can be best seen from the combustion timing response. Two sets of open-loop, steady-state combustion timing trajectories of an experimental HCCI testbed are shown in Fig. 4.1. In this figure, combustion timing is represented by θ_{50}, the engine position where fifty percent fuel energy conversion occurs (referenced from gas-exchange TDC). These two trajectories are generated with only one difference in inputs: the top plot of Fig. 4.1 has an earlier exhaust valve closure (EVC) timing to trap more exhaust in the cylinder.

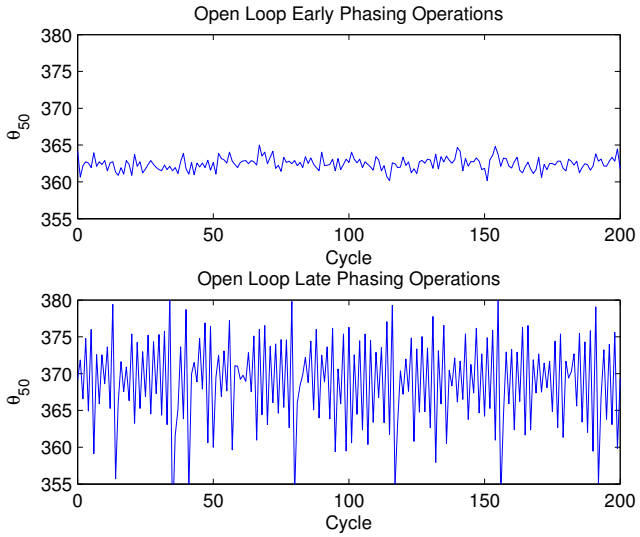

Figure 4.1: Early-phasing vs. late-phasing operation

As a result, the mixture temperature is higher on average which results in an earlier mean combustion timing compared to the bottom plot. Besides the difference in mean response, the variances of the responses are dramatically different in the two trajectories. Large oscillations in the bottom plot suggests that the system dynamics change significantly around this late ignition phasing operating point.

The oscillatory response of late phasing operation is clearly undesirable, but this operating point has merits from a practical point of view. An HCCI event delayed away from TDC occurs over a larger cylinder volume which decreases the rate of pressure rise during combustion. Therefore, late phasing HCCI is attractive in terms of reducing the audible engine noise and stress experienced by the cylinder, especially under high load conditions. Running the engine at the late phasing point, however, requires an understanding of how HCCI dynamics change in a wide range of operating conditions and appropriate cycle-by-cycle feedback control to improve the open-loop response.

Since the purpose of this chapter is understanding the change of system behavior, EVC is chosen as the only input for simplicity. Furthermore, the injected fuel quantity is assumed constant. It should be clear later that the insight of this chapter is still valid under a different amount of injected fuel, i.e., at a different load condition. This

chapter first uses a graphical approach to analyze the temperature dynamics around different operating points of the nonlinear model described in Chapter 3. The results show that there are three qualitative types of temperature dynamics across a wide range of recompression HCCI operations. This chapter further presents a three-region switching linear model that captures the qualitative change in system dynamics for control purposes.

4.1 Change in Temperature Dynamics

For a qualitative understanding of how HCCI dynamics change from one operating point to another, this sections presents a graphical analysis of the nonlinear model. Similar visualization techniques were used by Chiang *et al.* [51] and by Kang *et al.* [41] to analyze HCCI temperature dynamics. This graphical analysis shows how in-cylinder temperature at 300 CAD (60 CAD before combustion TDC) and 420 CAD (60 CAD after combustion TDC) evolve on a cycle-to-cycle basis. The temperature at 300 CAD, T_{300} (or $T_{\theta s}$, since 300 CAD is the state definition point of the NL), can be related roughly to ignition phasing, since ignition phasing is typically far more sensitive to temperature than oxygen concentration [61]. Knowing how T_{300} evolves from one cycle to the next gives much information about the combustion timing response. The temperature at 420 CAD (T_{420}) is a measure of the exhaust temperature, since this is a point after the end of combustion. T_{420} is of great interest because it represents the energy density of the exhaust that initiates the *next* HCCI event.

T_{300} and T_{420} are, of course, coupled. Besides the obvious fact that the temperature state, T_{300}, is dependent on the exhaust temperature on the *previous* cycle in recompression HCCI, there is also a correlation between T_{300} and T_{420} in the same cycle. It follows that a certain T_{300} leads to a certain ignition phasing which, in turn, determines the amount of heat transfer and work output during combustion and the subsequent expansion stroke and ultimately has an impact on T_{420}. With simplifying assumptions in the oxygen mode, the nonlinear model can generate two temperature maps: a combustion map that shows how $T_{300}(k)$ relates to $T_{420}(k)$, and a breathing

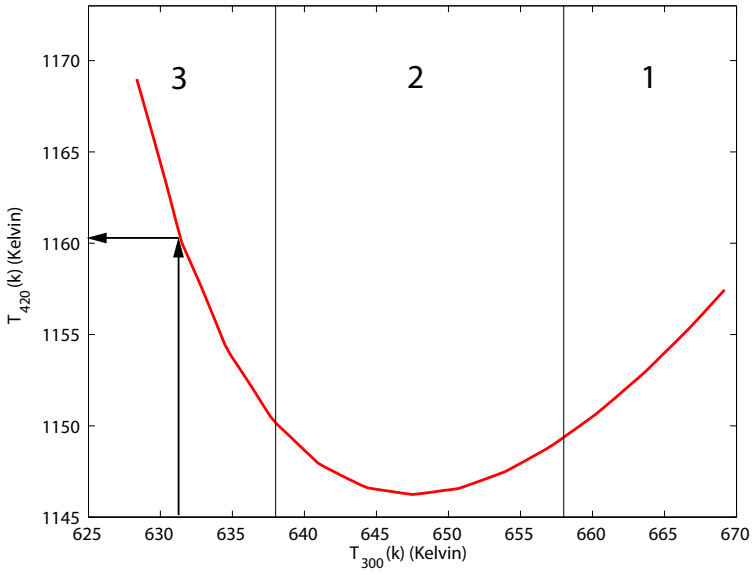

Figure 4.2: Combustion temperature map

map that shows how $T_{420}(k)$ relates to $T_{300}(k+1)$. The variable k here represents the engine cycle index.

4.1.1 Combustion Temperature Map

During the combustion stage, Fig. 4.2 shows how T_{300} at the beginning of the stage relates to T_{420} at the end of the stage, as indicated by the arrows in this plot. Note that both the oxygen content and temperature state have an effect on ignition timing in the nonlinear model and, therefore, can both influence the exhaust temperature, T_{420}. However, since ignition phasing is more sensitive to changes in temperature than oxygen content, neglecting the effect of oxygen content is a reasonable starting point. The effects of oxygen content are explicitly included later in the chapter. The data points shown in the 1-D map are obtained by varying the exhaust valve timing in steady state.

In Fig. 4.2, the bowl-shaped relationship shown is the result of changing heat transfer and work output characteristics across a wide combustion timing range. Note

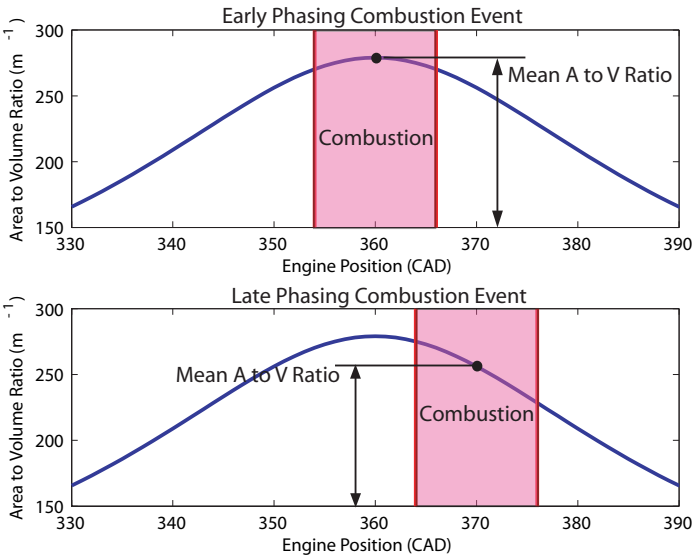

Figure 4.3: Area-to-volume ratio: early-ignition vs. late-ignition

that the rightmost data point in Fig. 4.2 corresponds to a θ_{50} close to 360 CAD (combustion TDC). This is why, locally, the temperature relationship in the region marked **1** in Fig. 4.2 shows a positive slope. In this region, a change in the charge temperature on the x-axis leads to a θ_{50} close to combustion TDC where the cylinder volume is changing relatively slower. Therefore, the amount of heat transfer and work output is not sensitive to a change in combustion timing. As a result, the bulk temperature effect dominates in Region **1**, i.e., a higher charge temperature, T_{300}, monotonically leads to a higher exhaust temperature, T_{420}.

As the charge temperature on the x-axis further decreases into the region marked **3** in Fig. 4.2, combustion timing becomes significantly later (the leftmost data point in Fig. 4.2 has a θ_{50} of 11 CAD after combustion TDC). When the combustion timing is sufficiently late, the amount of heat transfer during combustion and the work output during the expansion stroke both reduce significantly. The lower heat transfer can be attributed to a decrease in the mean area-to-volume ratio [45] and a lower in-cylinder temperature during a late HCCI combustion. The area-to-volume

ratio around TDC can be seen in Fig. 4.3. In this figure, two combustion events take place in the shaded regions. In the bottom plot, late HCCI combustion occurs away from TDC with a lower mean area-to-volume ratio compared to the early HCCI combustion in the top plot. In addition, the average gas temperature during a late combustion event is lower, as combustion occurs over a larger cylinder volume. This creates a smaller temperature gradient between the in-cylinder gas and the cylinder wall. These two effects result in lower overall heat transfer in a late phasing HCCI event. Furthermore, work output typically decreases when HCCI occurs too late in the expansion stroke. As a result, a late HCCI event yields exhaust gas of higher internal energy which is why the exhaust temperature in Region **3** in Fig. 4.2 starts to increase when the charge temperature is sufficiently low.

Roughly speaking, there exist three types of correlation between the charge and exhaust temperature. In Region **1** in Fig. 4.2, there is a positive correlation between T_{300} and T_{420}. This region also has higher charge temperature corresponding to early ignition phasing operations. On the other hand, Region **3** exhibits a negative correlation between the two temperature and has low charge temperature corresponding to late phasing operations. There is also a transitional region in between, Region **2**, where there is little correlation between the two temperatures.

4.1.2 Breathing Temperature Map

Fig. 4.4 shows how the exhaust temperature on one cycle relates to the charge temperature on the *next* engine cycle. Naturally, this relationship depends on the amount of exhaust trapped in the cylinder which is further dependent on the EVC command. As a result, a given $T_{420}(k)$ on the y-axis can be paired with an EVC value to map to a $T_{300}(k+1)$ on the x-axis. The breathing temperature map matches the intuition that a higher exhaust temperature monotonically leads to a higher $T_{300}(k+1)$ given the same EVC. Also, a later EVC monotonically leads to a lower $T_{300}(k+1)$ given the same exhaust temperature on the *previous* cycle, due to the decrease in the amount of trapped exhaust.

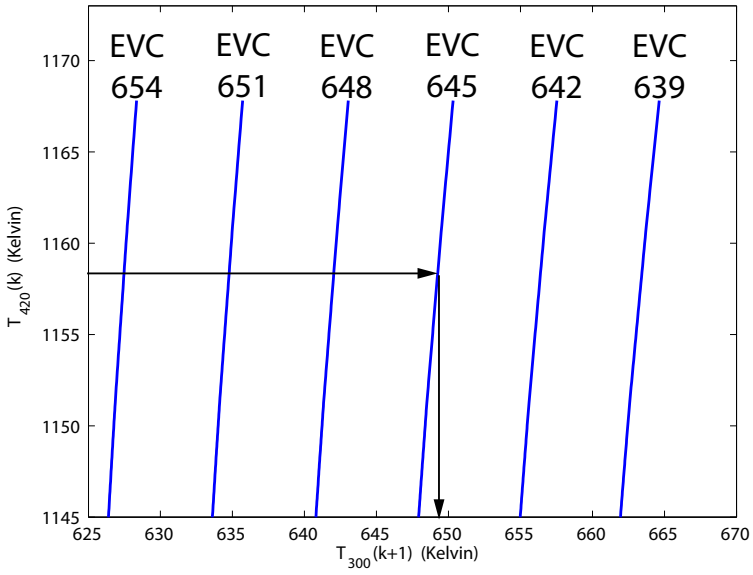

Figure 4.4: Breathing temperature map

4.1.3 Temperature Trajectories around Different Operating Points

The two temperature maps, Fig. 4.2 and Fig. 4.4, can be overlaid on top of each other. A temperature trajectory can then be traced out starting from an initial temperature by alternating the two temperature maps. In this section, one temperature trajectory is shown within each of the three regions marked in Fig. 4.2.

The Early Ignition Phasing Region: Region 1

In Fig. 4.5, a temperature trajectory starts from an initial charge temperature marked by the asterisk **1**. After the first HCCI event, this charge temperature is mapped to a certain exhaust temperature, T_{420}, indicated by the circle **1'**. This exhaust temperature goes through the breathing stage and is further mapped to the charge temperature marked by the asterisk **2**. As can be seen, the temperature trajectory eventually converges to the equilibrium marked by the intersection of the combustion and breathing temperature maps. In Fig. 4.5, the charge temperature, indicated by

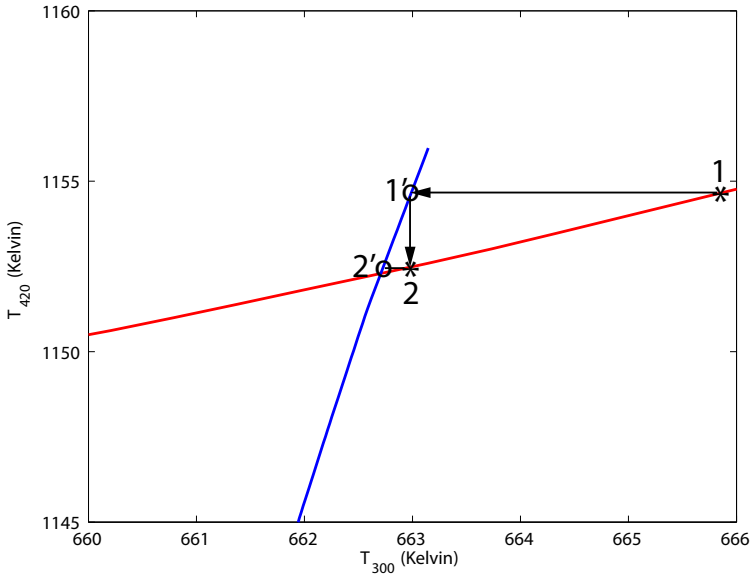

Figure 4.5: Temperature trajectory around an early-phasing point

the asterisks, smoothly decays to the equilibrium value due to the locally positive correlation between the charge and exhaust temperature during combustion. Note that equilibria in this region are associated with early ignition timing due to the higher charge temperature.

The Sweet Spot Region: Region 2

Similarly, a temperature trajectory inside the transitional region, Region **2** in Fig. 4.2, can be traced out in Fig. 4.6. As can be seen, the charge temperature roughly converges to the equilibrium charge temperature within one cycle. This is because there is very little correlation between T_{300} and T_{420} during combustion within this region. In Region **2**, any change in the charge temperature produces roughly the same exhaust temperature and, therefore, leads back to the same nominal charge temperature on the *next* cycle given the same EVC. This region is essentially a "sweet spot" of HCCI operation in terms of its capability to reject disturbance, since any charge temperature perturbations roughly die out in one cycle.

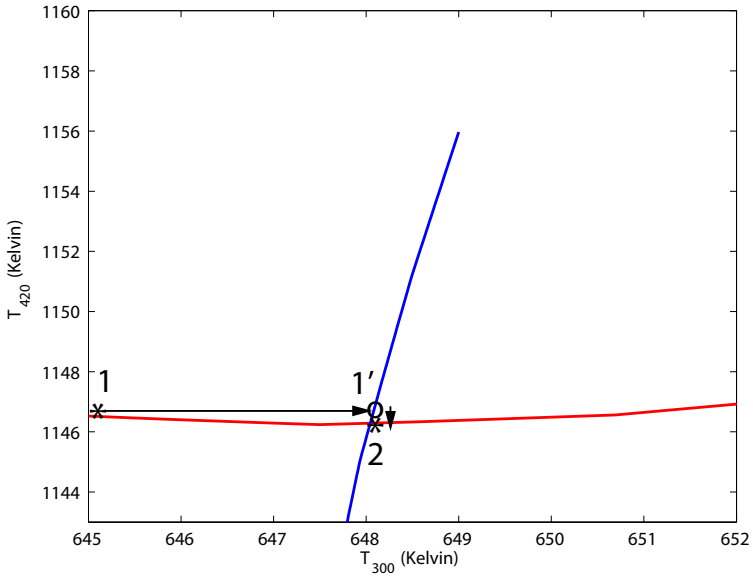

Figure 4.6: Temperature trajectory around a sweet spot

The Late Ignition Phasing Region: Region 3

Finally, a temperature trajectory within the late ignition phasing region is shown in Fig. 4.7. Compared to the early phasing region, the temperature correlation in the combustion stage is reversed in the late phasing region, as can be seen from the negative-sloped red line in Fig. 4.7. As a result, the charge temperature oscillates about the equilibrium in Fig. 4.7 instead of the smooth convergence shown in Fig. 4.5. This behavior also coincides with the observation made on the experimental testbed, i.e. the combustion timing response is oscillatory around a late phasing operating point as shown in the bottom plot of Fig. 4.1. When this set of late phasing operation data, which spans a wide combustion timing range, is further structured as a lag plot shown in Fig. 4.8, a pattern emerges and further validates the three types of temperature dynamics in this graphical analysis. The right half of Fig. 4.8 shows a clear negative correlation structure i.e. a later θ_{50} on cycle k on the x-axis leads to an earlier θ_{50} on cycle $k+1$ on the y-axis. On the other hand, a positive correlation can be seen in the left half of Fig. 4.8. In between these two dominant structures,

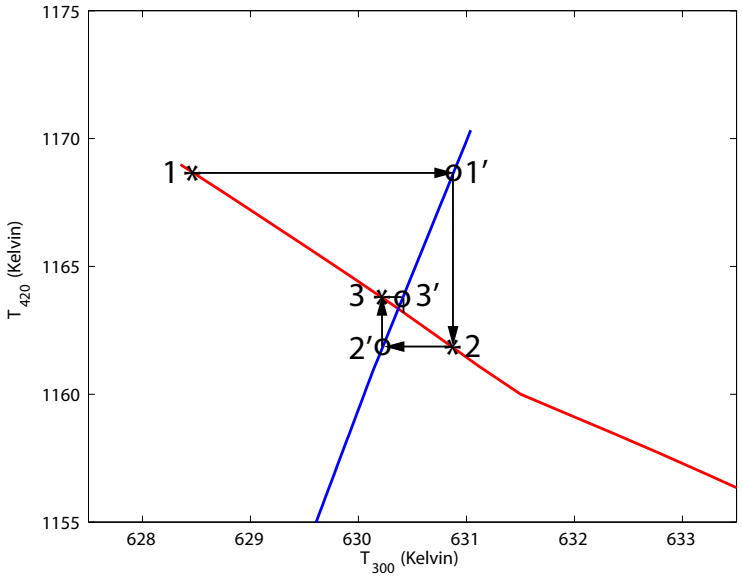

Figure 4.7: Temperature trajectory around a late-phasing point

there is a transitional region where any change in $\theta_{50}(k)$ on the x-axis roughly leads to the same $\theta_{50}(k+1)$ on the y-axis.

Clearly, the change in system behavior is caused by the "bowl-shaped" combustion temperature map shown in Fig. 4.2. Under a different fueling rate, the same physical factors that lead to this bowl-shaped curve remain in place. Therefore changing the amount of injected fuel roughly moves the combustion temperature map vertically. As a result, the qualitative understanding in this section is the same under a different load condition.

The graphical analysis suggests that there exist three types of temperature dynamics across the operating range due to the three qualitative types of temperature correlations during combustion. As a result, a minimum of three linear models is needed to describe recompression HCCI over its operating range. To obtain these, the nonlinear model with both oxygen and temperature dynamics is linearized about three equilibrium points: one equilibrium in each of the three regions in Fig. 4.2.

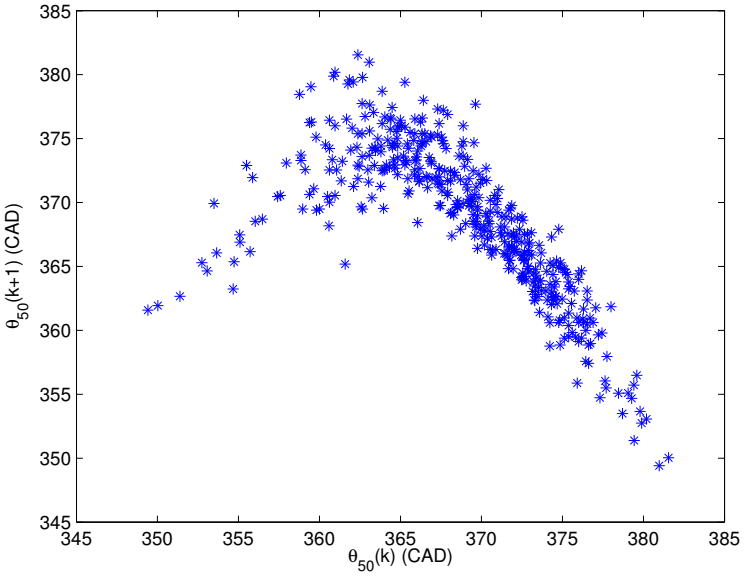

Figure 4.8: Lag plot of combustion timing: late-phasing operation

4.2 Three Regions and Corresponding Linearized Models

Before the linearization results are presented, the format of a linearized model is first explained in Section 4.2.1.

4.2.1 Linearizations of the Nonlinear Model

To understand the local behavior of the nonlinear model, Equation (3.4) and Equations (3.19) can be further linearized about an equilibrium. A set of nominal state, input and output values characterize this particular operating point and are denoted as $O_{2,i}$, T_i, $V_{EVC,i}$ and $\theta_{50,i}$. The resulting linearized system has the following structure:

$$\begin{aligned} \tilde{x}_i(k+1) &= \tilde{A}_i \cdot \tilde{x}_i(k) + \tilde{B}_i \cdot \tilde{u}_i(k) \\ \tilde{y}_i(k) &= \tilde{C}_i \cdot \tilde{x}_i(k) \end{aligned} \tag{4.1}$$

where

$$\tilde{A}_i = \left[\begin{array}{cc} \frac{\partial f}{\partial n_{\theta_s}^{O_2}} \cdot n_{\theta_s,i}^{O_2} & \frac{\partial f}{\partial T_{\theta_s}} \cdot T_{\theta_s,i} \\ \frac{\partial g}{\partial n_{\theta_s}^{O_2}} \cdot n_{\theta_s,i}^{O_2} & \frac{\partial g}{\partial T_{\theta_s}} \cdot T_{\theta_s,i} \end{array} \right] \Bigg|_{n_{\theta_s}^{O_2}=n_{\theta_s,i}^{O_2}, T_{\theta_s}=T_{\theta_s,i}}$$

$$\tilde{B}_i = \left[\begin{array}{c} \frac{\partial f}{\partial V_{evc}} \cdot V_{evc,i} \\ \frac{\partial g}{\partial V_{evc}} \cdot V_{evc,i} \end{array} \right] \Bigg|_{V_{evc}=V_{evc,i}}$$

$$\tilde{C}_i = \left[\begin{array}{cc} \frac{\partial h}{\partial n_{\theta_s}^{O_2}} \cdot n_{\theta_s,i}^{O_2} & \frac{\partial h}{\partial T_{\theta_s}} \cdot T_{\theta_s,i} \end{array} \right] \Big|_{n_{\theta_s}^{O_2}=n_{\theta_s,i}^{O_2}, T_{\theta_s}=T_{\theta_s,i}}$$

$$\tilde{x} = \left[\begin{array}{c} \frac{n_{\theta_s}^{O_2} - n_{\theta_s,i}^{O_2}}{n_{\theta_s,i}^{O_2}} \\ \frac{T_{\theta_s} - T_{\theta_s,i}}{T_{\theta_s,i}} \end{array} \right]$$

$$\tilde{u}_i = \frac{V_{evc} - V_{evc,i}}{V_{evc,i}}$$

$$\tilde{y}_i = \frac{\theta_{50} - \theta_{50,i}}{\theta_{50,i}}$$

The subscript i represents the variable value at the steady-state operating point i. The $\sim$ symbol in (4.1) signifies the locality of these variables around the steady-state operating point i. This notation becomes useful when multiple linearizations are introduced. Under this structure, the states, input and output represent normalized changes with respect to the steady-state values of the operating point. Comparing the local behaviors around different equilibria makes more intuitive sense with this linear model format.

4.2.2 Three Linearized Models

Picking one equilibrium in each of the three regions in Fig. 4.2 gives three linearized models: The linearized model for the early ignition region (Region **1** in Fig. 4.2) is given as:

$$\begin{aligned} \tilde{A}_1 &= \left[\begin{array}{cc} 0.6037 & 0.3767 \\ -0.0062 & 0.1876 \end{array} \right] \quad \tilde{B}_1 = \left[\begin{array}{c} -2.3784 \\ 0.4428 \end{array} \right] \\ \tilde{C}_1 &= \left[\begin{array}{cc} -0.0164 & -0.4666 \end{array} \right] \end{aligned} \tag{4.2}$$

For the sweet spot region (Region **2** in Fig. 4.2):

$$\begin{aligned} \tilde{A}_2 &= \begin{bmatrix} 0.5616 & 0.1913 \\ -0.0115 & -0.0112 \end{bmatrix} \quad \tilde{B}_2 = \begin{bmatrix} -1.6006 \\ 0.3929 \end{bmatrix} \\ \tilde{C}_2 &= \begin{bmatrix} -0.0222 & -0.6385 \end{bmatrix} \end{aligned} \tag{4.3}$$

And lastly, for the late phasing region (Region **3** in Fig. 4.2):

$$\begin{aligned} \tilde{A}_3 &= \begin{bmatrix} 0.4922 & 0.0326 \\ -0.0313 & -0.6092 \end{bmatrix} \quad \tilde{B}_3 = \begin{bmatrix} -1.0481 \\ 0.3474 \end{bmatrix} \\ \tilde{C}_3 &= \begin{bmatrix} -0.0549 & -1.6905 \end{bmatrix} \end{aligned} \tag{4.4}$$

Each linearization faithfully captures the qualitative behavior of the three regions in the graphical analysis. Particularly, the A_{22} entry of each A matrix represents how the temperature state on cycle k affects the temperature state on cycle $k+1$. During early ignition operations, it shows a positive A_{22} entry that corresponds to a smooth decay. There is a strong negative A_{22} entry in Region **3** that shows highly oscillatory dynamics in the late ignition timing region. Region **2** has an A_{22} entry that is close to zero, signifying the "deadbeat" temperature dynamics that are impervious to disturbance.

Other entries of the A matrix also give insights about the HCCI process. The A_{21} entries represent how oxygen concentration on one cycle affects the temperature state on the next cycle. Since oxygen concentration has a minor effect on ignition timing, it only has a small impact on the exhaust temperature which further translates to small A_{21} entries in all three regions. On the other hand, the A_{12} entries change their magnitudes notably due to the change in T_{300}-T_{420} correlations across the range of operation. This is because different exhaust temperatures affect the subsequent breathing processes differently, and exert different influences on the oxygen concentration on the *next* engine cycle. All A_{11} entries show a smooth decaying behavior with a slower converging rate. Since recompression HCCI traps a fairly large portion of the exhaust gas, it makes sense that an excess of oxygen takes several cycles to be

bled out of the system. Capturing the oxygen dynamics in the first row of A can be important in guaranteeing the air-fuel ratio stays within the permitted range.

4.3 The Switching Linear Model

Both the graphical analysis and the linearized models show that the entire operating range qualitatively possesses three sets of cycle-to-cycle temperature dynamics: smooth decaying in the early ignition phasing region, oscillatory in the late phasing region and strongly converging in the sweet spot region. As a result, a model that switches between the three linearizations can capture the change in HCCI dynamics for control purposes. Depending on which region the temperature state is in, the corresponding linear model is used to describe HCCI dynamics. It should be noted that each linearization in Equations (4.2), (4.3) and (4.4) captures the system dynamics about a different equilibrium. Each of the equilibria is associated with a different set of steady-state oxygen content, temperature, V_{EVC} and θ_{50} as defined in Equations (4.1). Therefore, the same numerical values of system states from two different linearized models represent different physical quantities. To arrive at an unified state, input and output description, it is necessary to re-normalize each linear model with a nominal set of steady state values. An example of the re-normalization can be found in Appendix B. By choosing the steady-state values associated with the sweet spot model (4.3), the resulting switching linear model can be expressed as:

$$\begin{aligned} x(k+1) &= A_i \cdot x(k) + B_i \cdot u(k) + d_i \\ y(k) &= C_i \cdot x(k) + e_i \\ &\text{if } x(k) \in \Omega_i, \qquad i = 1, 2, 3 \end{aligned} \tag{4.5}$$

where

$$\Omega_i \triangleq \{x : S_i x \leq R_i\} \tag{4.6}$$

The convention in Equations (4.2), (4.3) and (4.4) is followed which associates $i = 1$ to the early phasing region, $i = 2$ to the sweet spot region and $i = 3$ to the late phasing region. Note that the $\sim$ symbols are dropped in Equations (4.5), since it

is a global model instead of the local linearization shown in (4.1). The matrices S_i and R_i define the region where model i is active. Since the switching mechanism is constructed according to temperature thresholds indicated by the vertical lines in Fig. 4.2, this gives:

$$S_i = \begin{bmatrix} 0 & 1 \\ 0 & -1 \end{bmatrix} \quad R_i = \begin{bmatrix} T_{i,u} \\ -T_{i,l} \end{bmatrix} \tag{4.7}$$

where $T_{i,u}$ and $T_{i,l}$ are the upper and lower limits of each region. Also, the thresholds have the following relatioship:

$$T_{i,l} = T_{i+1,u} \tag{4.8}$$

Therefore, the lower temperature limit of a region is the upper limit of the next region. The additional bias terms d_i and e_i in Equations (4.5) stem from the nonlinear nature of Equation (3.19) and Equation (3.4). Since the steady state values of the sweet spot model are chosen as the standard states, input and output throughout the three regions, d_2 and e_2, are identically zero.

The temperature thresholds for each region are chosen such that an equilibrium always exists given a certain steady state input. Furthermore, this equilibrium is unique. To satisfy these conditions, first define a steady state input, $u_{i,l}$, that results in a steady-state temperature with the i_{th} linear model equal to the i_{th} lower temperature threshold, $T_{i,l}$:

$$T_{i,l} = \begin{bmatrix} 0 & 1 \end{bmatrix} \cdot (I - A_i)^{-1} \cdot (B_i \cdot u_{i,l} + d_i) \tag{4.9}$$

To fulfill the requirements of the region thresholds, the same-steady state input, $u_{i,l}$, drives the steady-state temperature with the $i + 1_{th}$ linear model to its upper temperature threshold:

$$T_{i+1,u} = \begin{bmatrix} 0 & 1 \end{bmatrix} \cdot (I - A_{i+1})^{-1} \cdot (B_{i+1} \cdot u_{i,l} + d_{i+1}) \tag{4.10}$$

With the relationship in Equation (4.8), equating Equation (4.9) and (4.10) and

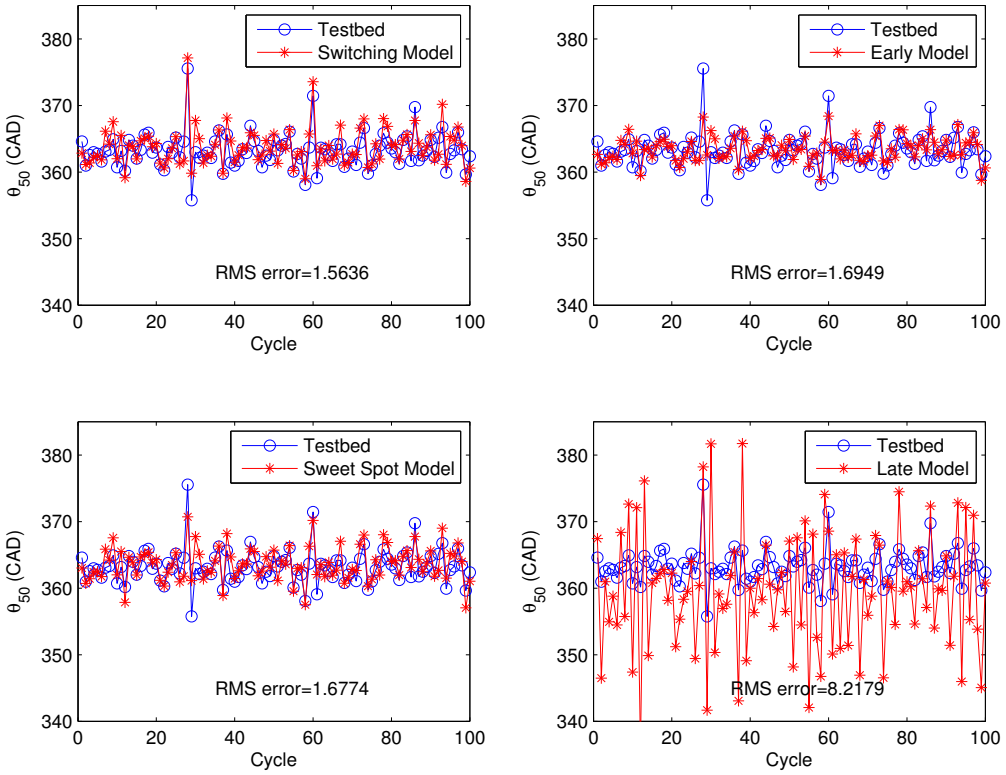

Figure 4.9: θ_{50} responses: test bed response compared to the the response of the switching linear model(top left), the early-phasing model(top right), the sweet-spot model(bottom left) and the late-phasing model(bottom right)

solving for $u_{i,l}$ gives:

$$u_{i,l} = \frac{\begin{bmatrix} 0 & 1 \end{bmatrix} \cdot \left[(I - A_{i+1})^{-1} \cdot d_{i+1} - (I - A_i)^{-1} \cdot d_i \right]}{\begin{bmatrix} 0 & 1 \end{bmatrix} \cdot \left[(I - A_i)^{-1} \cdot B_i - (I - A_{i+1})^{-1} \cdot B_{i+1} \right]} \tag{4.11}$$

Substituting the calculated $u_{i,l}$ from Equation (4.11) into Equation (4.9) gives the lower temperature threshold for the i_{th} region. Temperature thresholds for other regions can be calculated in a similar manner.

To show that Equations (4.5) capture the cycle-to-cycle dynamics better than a

single linearization, an EVC trajectory is randomly generated and fed to the switching linear model and the three local linearized models (4.2), (4.3) and (4.4). The resulting θ_{50} responses are compared to the engine testbed subjected to the same input trajectory shown in blue in Fig. 4.9.The root-mean-square (RMS) error in θ_{50} computed for each case. Not surprisingly, the switching linear model results in the lowest RMS error when compared to the testbed. The early phasing model generates a RMS error close to the switching linear model. This is because the randomly generated EVC trajectory is biased towards the early phasing region, favoring the early phasing model in this particular test.

4.4 Conclusion

Compared to using a single linearization, it is not surprising that combining multiple linearized models better approximates a nonlinear system over a wide range. As a matter of fact, this is a widely used approach for designing gain-scheduling controllers for nonlinear systems. There are two commonly quoted drawbacks with this approach. Firstly, it is often unclear what the appropriate number of linearizations should be, as a result, control design becomes an ad hoc process, i.e. increasing the number of linearizations until satisfactory performance is achieved. Secondly, as switching between a number of *stable* linear systems can cause instability, this approach is associated with stability concerns. In this chapter, the graphical analysis quells the first concern by revealing the three qualitative types of temperature dynamics: smooth converging in the early phasing region, oscillatory in the late phasing region and strongly converging in between. Of particular interest is that the oscillatory dynamics coincide with the highly variable ignition phasing response observed on the testbed around a late phasing operating point. The ability to make this problematic operating point usable in closed-loop is a benchmark for the switching controller presented in the next chapter. Furthermore, Chapter 5 aims to address the second drawback of the switching modeling/control approach by providing both experimental and analytical stability evidence.

Chapter 5

Combustion Timing Control with a Switching Controller

The three-region switching linear model is motivated by the insight that there exist three types of temperature dynamics across a wide range of recompression HCCI operation. The model captures the qualitative change in system behavior and has a simple structure for control synthesis. Based on this model, this chapter further presents a three-region switching controller that consists of three local LQR controllers. This switching controller is evaluated on the engine testbed and is effective across a wide range of desired combustion timing. Particularly, the problematic late phasing operating point shown in the bottom plot of Fig. 4.1 is made well-behaved with the switching controller in closed-loop. This chapter also reveals that a local linear controller has a directionality error when the operating conditions deviate sufficiently from the linearized point, which causes misfires on the testbed. This demonstrates the drawback of using a single linear controller commonly employed in previous work on combustion timing control of HCCI.

In the last part of this chapter, two semi-definite programs (SDP) are presented to establish the stability properties of the switching model/control formulation. It is well known that even switching between a number of *stable* linear systems can cause instability. The stability guarantees serve as an analytical check and echoes the controller's success on the experimental testbed. Furthermore, although the switching

linear model is intended as a platform for tractable control design, it is a reasonable approximation of the experimental testbed as shown in Fig. 4.9; therefore, the stability statements presented can be viewed as a preliminary investigation of global stability of recompression HCCI.

Due to the close connection between Chapter 4 and Chapter 5, the same conventions and variable names are used in these two chapters.

5.1 The Switching LQR Controller

Just as with the switching linear model, a switching controller can be formed with three local controllers. One approach to obtain these local controllers is by designing three LQR controllers based on the three linearized systems (4.2), (4.3) and (4.4).

5.1.1 Local LQR Controllers

Each of the three local feedback control laws is given as:

$$\tilde{u}_i(k) = -\tilde{K}_i \cdot \tilde{x}_i(k) \tag{5.1}$$

where $\tilde{x}_i$, $\tilde{K}_i$ and $\tilde{u}_i$ are the states, feedback gains and input for the i_{th} linearized system defined in Equations (4.2), (4.3) and (4.4). These controllers are derived so that they optimize the respective cost functions (5.2) with the same weights Q and R.

$$J_i = \sum_{\tau=0}^{\infty} \tilde{x}_i(\tau)^T \cdot \tilde{C}_i^T \cdot Q \cdot \tilde{C}_i \cdot \tilde{x}_i(\tau) + \tilde{u}_i(\tau)^T \cdot R \cdot \tilde{u}_i(\tau) \tag{5.2}$$
$$i = 1, 2, 3, \quad Q = 85, \quad R = 1$$

It is implied in the cost functions that the propagation from $\tilde{x}_i(k)$ to $\tilde{x}_i(k+1)$ follows the dynamics of the i_{th} linearized system. Note that Equation (5.2) aims to regulate the outputs of of the linearized models, $\tilde{C}_i \cdot \tilde{x}_i$. The resulting feedback control gains in each region are given as:

For the early ignition region (Region **1** in Fig. 4.2):

$$\tilde{K}_1 = \begin{bmatrix} 0.0299 & 0.3958 \end{bmatrix} \tag{5.3}$$

For the sweet spot region (Region **2** in Fig. 4.2):

$$\tilde{K}_2 = \begin{bmatrix} 0.0189 & -0.0109 \end{bmatrix} \tag{5.4}$$

For the late ignition region (Region **3** in Fig. 4.2):

$$\tilde{K}_3 = \begin{bmatrix} -0.0471 & -1.8632 \end{bmatrix} \tag{5.5}$$

Note the $\sim$ symbols on top of K signify that these are local controllers. Therefore, a positive oxygen concentration and temperature state in Region **1** warrants a negative input based on (5.1) and (5.3). This should be read as a higher oxygen concentration and temperature with respect to the linearized point in Region **1** warrants a decrease in volume at EVC.

The temperature control gains, the second entries of $\tilde{K}$, show a change in sign between Region **1** and **3**. In Region **3**, a lower temperature with respect to the linearized point results in a decrease in volume at EVC to trap less exhaust. This is due to the negative correlation between the charge temperature and exhaust temperature in Region **3** shown in Fig. 4.2. Since the temperature correlation is positive in Region **1**, it makes sense that the temperature control gain of $\tilde{K}_1$ reverses its sign compared to $\tilde{K}_3$. This suggests that a controller works well in Region **1** can have an error in its directionality when applied to equilibria in Region **3**, making the highly oscillatory nature of late phasing HCCI even worse. The temperature gain in $\tilde{K}_2$ is small in magnitude. Since equilibria in Region **2** are naturally impervious to disturbance, the feedback controller does not need to exert much effort to regulate ignition phasing.

The open- and closed-loop pole locations for the three regions are tabulated in Table 5.1. In Table 5.1, all three open-loop systems show consistent oxygen modes which have the pole locations around 0.5. The temperature dynamics, on the other

Table 5.1: Pole locations of the open- and closed-loop linearized systems

	Region 1	Region 2	Region 3
Open Loop	0.5980, 0.1933	0.5578, -0.0074	0.4912 , -0.6082
Closed Loop	0.6336, 0.0536	0.5864, -0.0014	0.5044, -0.0235

hand, show a sign change in the three linear models in open loop. With feedback controllers, the closed-loop pole locations consistently show that the temperature modes have been moved close to the origin across all three regions and should demonstrate the same strong disturbance rejection characteristics as open-loop sweet spot HCCI operation. Furthermore, the cost function shown in Equation (5.2) aims to regulate the outputs of the linearized models, which are weakly dependent on the oxygen state. Therefore, the closed-loop eigenvalues of the oxygen modes are not significantly altered compared to the open-loop eigenvalues.

5.1.2 Feed-forward Gains for Reference Tracking

In the previous section, the three local feedback controllers regulate the system output around their respective linearized points. To enable tracking of a desired θ_{50} trajectory, a feed-forward input is needed in addition to the feedback control. Due to the fact that the switching linear model is composed of three linear models, three sets of feed-forward gains can be generated with each linearization. Therefore, at each time step, three feed-forward inputs are possible given a desired θ_{50}. In this section, the calculation of the three sets of feed-forward gains is first shown, then the ambiguity of three possible feed-forward gains is removed by associating each set of gains to a unique range of desired output.

The switching linear system described in (4.5) which reaches a desired steady-state

command, r_{ss}, satisfies the following equation:

$$\begin{aligned} x_{ss,i} &= A_i \cdot x_{ss,i} + B_i \cdot u_{ss,i} + d_i \\ r_{ss} &= C_i \cdot x_{ss,i} + e_i \\ i &= 1, 2, 3 \end{aligned} \tag{5.6}$$

where $u_{ss,i}$ and $x_{ss,i}$ are the steady state input and system states associated with r_{ss}. The feed-forward gains $N_{x,i}$ and $N_{u,i}$ are designed such that they satisfy the following equations:

$$\begin{aligned} x_{ss,i} &= N_{x,i} \cdot r_{ss} \\ u_{ss,i} &= N_{u,i} \cdot r_{ss} \end{aligned} \tag{5.7}$$

Substituting Equation (5.7) into Equation (5.6) gives:

$$\begin{aligned} N_{x,i} \cdot r_{ss} &= A_i \cdot N_{x,i} \cdot r_{ss} + B_i \cdot N_{u,i} \cdot r_{ss} + d_i \\ r_{ss} &= C_i \cdot N_{x,i} \cdot r_{ss} + e_i \\ i &= 1, 2, 3 \end{aligned} \tag{5.8}$$

Rearranging Equation (5.8) gives the following equation:

$$\begin{bmatrix} I - A_i & -B_i \\ C_i & \mathbf{0} \end{bmatrix} \cdot \begin{bmatrix} N_{x,i} \\ N_{u,i} \end{bmatrix} = \begin{bmatrix} \frac{d_i}{r_{ss}} \\ 1 - \frac{e_i}{r_{ss}} \end{bmatrix} \qquad i = 1, 2, 3 \tag{5.9}$$

Therefore, the three sets of feed-forward gains are given by:

$$\begin{bmatrix} N_{x,i} \\ N_{u,i} \end{bmatrix} = \begin{bmatrix} I - A_i & -B_i \\ C_i & \mathbf{0} \end{bmatrix}^{-1} \cdot \begin{bmatrix} \frac{d_i}{r_{ss}} \\ 1 - \frac{e_i}{r_{ss}} \end{bmatrix} \qquad i = 1, 2, 3 \tag{5.10}$$

To remove the ambiguity of three possible feed-forward gains, recall the input, $u_{i,l}$, calculated in Equation (4.11). This input drives the temperature state to the lower temperature limit of the i_{th} region. It is also associated with the highest steady state

output, $y_{i,u}$, in the i_{th} region:

$$y_{i,u} = C_i \cdot (I - A_i)^{-1} \cdot (B_i \cdot u_{i,l} + d_i) + e_i \tag{5.11}$$

Since $C_i \cdot (I - A_i)^{-1} \cdot B_i$ is always negative, $y_{i,u}$ is indeed the highest achievable steady state output in the i_{th} region. At any given cycle, the feed-forward gains associated with the i_{th} region are chosen if the desired output is lower than $y_{i,u}$ but higher than $y_{i-1,u}$.

With these, the full control law that combines feedback and feed-forward is given by:

$$u(k) = N_{u,\lambda} \cdot y_{des}(k) + K_\mu \cdot [N_{x,\lambda} \cdot y_{des}(k) - x(k)] \tag{5.12}$$

$$\mu = \{i : x(k) \in \Omega_i\} \qquad i = 1, 2, 3 \tag{5.13}$$

$$\lambda = \{i : y_{i,u} \geq y_{des} \geq y_{i-1,u}\} \qquad i = 1, 2, 3 \tag{5.14}$$

5.2 Experimental Results

In this section, the switching controller (5.12) with the feedback gains shown in Equations (5.3), (5.4) and (5.5) is evaluated on an experimental engine testbed. The system response is generally not The testbed is a 2.2 liter 4-cylinder GM Ecotech engine. The fully flexible EHVS presented in Chapter 2 is mated with this engine to provide valve actuation. Both the intake and exhaust valve events are 140 CAD in duration and have a maximum lift at 4 mm. The IVC timing is fixed at 210 CAD (referenced from recompression TDC) and the EVC timings are decided by the switching controller. Gasoline is directly injected into each cylinder at a rate of 10 mg per cycle. The injection timing is fixed at 40 CAD. All the experiments presented are conducted at an engine speed of 1800 RPM with a fixed throttle position. The intake manifold pressure is therefore dependent on valve timing but is typically around 97 kPa. Each cylinder has a pressure sensor installed with a sampling rate of 10 kHz. The pressure measurement is then fed to an algorithm to calculate θ_{50} which is a proxy of combustion timing as well as the output to be controlled. The Matlab xPC platform is used to implement the control algorithms and perform all the necessary sensing and

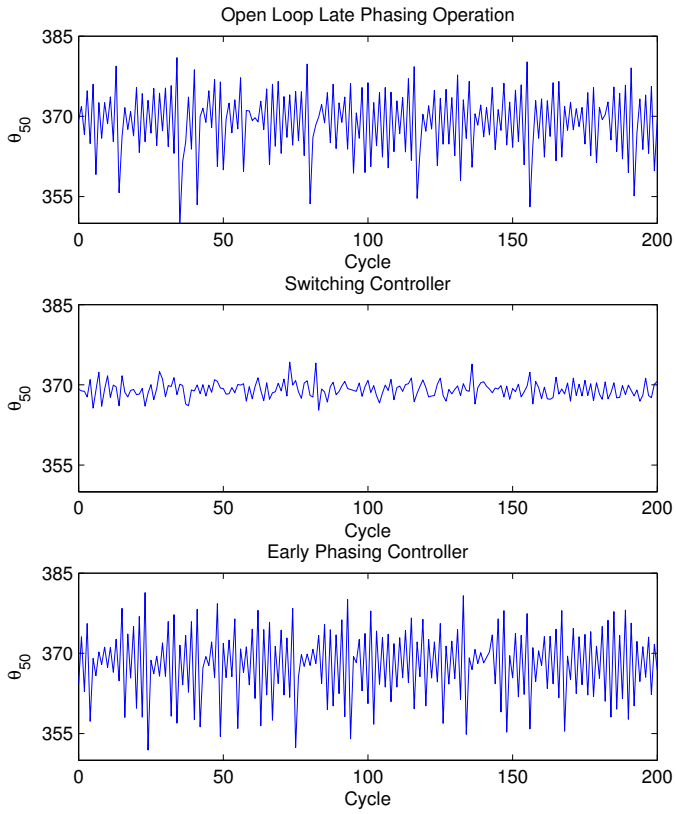

Figure 5.1: Open- vs. closed-loop late phasing operation: θ_{50}

actuation.

With this setup, the switching controller is tasked to track two steady-state θ_{50} commands and a reference trajectory that spans the entire operating range. Three local Kalman filters are implemented to give state estimates in each region based on the θ_{50} measurements. Note that these local estimators update a single set of shared state estimate, instead of each having their own state estimates.

5.2.1 Late Phasing Steady-State Performance

Open loop late phasing operation shows a highly oscillatory response in Fig. 4.1 (shown again here in the top plot of Fig. 5.1 for convenience) and translates to a

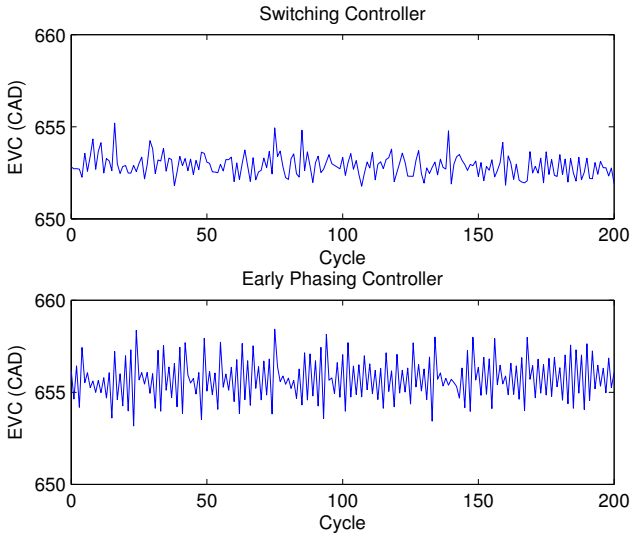

Figure 5.2: Closed-loop late phasing operation: EVC

negative real eigenvalue in the linearized model. A cycle-by-cycle feedback controller actively changes the dynamics around the ill-behaved equilibrium as shown by the closed-loop system poles in Table 5.1. In this experiment, the performance of the switching controller is evaluated on the testbed at a desired θ_{50} of 9 CAD after TDC. This ignition phasing is the same as the mean θ_{50} achieved in the top plot of Fig. 5.1. The closed-loop response with the switching controller is shown in the middle plot of Fig. 5.1. As can be seen, the switching controller successfully reduces the variance of θ_{50}. Compared to the open-loop, late-phasing experiment shown in the top plot, the switching controller reduces the standard deviation of θ_{50} by a factor of 2.6 while maintaining the same mean response.

To demonstrate the importance of capturing the change in HCCI dynamics, the bottom plot of Fig. 5.1 shows the early phasing region controller in Equation (5.3) tracking the same desired θ_{50} command. Generally, this controller does the *opposite* of the switching controller in the late phasing region, as suggested by the temperature control gains in Section 5. As a result, the standard deviation of θ_{50} increases slightly compared to open loop, the cylinder eventually misfires using this setup. The corresponding control actions for the two closed-loop controllers presented in this

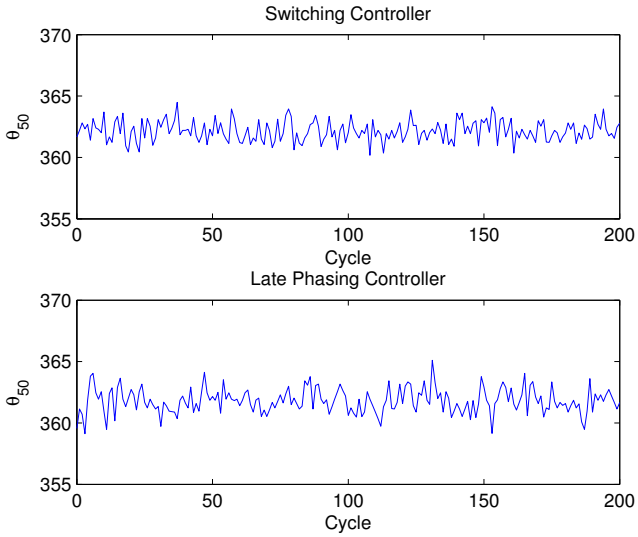

Figure 5.3: Closed-loop early phasing operation: θ_{50}

section are plotted in Fig. 5.2. Note that it takes less than a 3 CAD peak-to-peak exhaust valve timing movement for the switching controller to achieve the well-behaved combustion timing response in the middle plot of Fig. 5.1.

5.2.2 Early Phasing Steady-State Performance

In this experiment, the late-phasing controller in Equation (5.5) is compared against the switching controller. The desired θ_{50} in this experiment is 2 CAD after TDC, which is an early phasing operating point. Compared to the results of the switching controller shown in the top plot of Fig. 5.3, the late-phasing controller increases the standard deviation of combustion timing very slightly. However, the control actions of the two controllers shown in Fig. 5.4 suggest that the late-phasing controller uses much more control authority. In this experiment, the standard deviation of EVC with the late-phasing controller is 2.7 times greater than that of the switching controller. From an LQR cost standpoint where deviations of output and large control actions are both penalized, the switching control undoubtedly outperforms the late-phasing controller at this operating point.

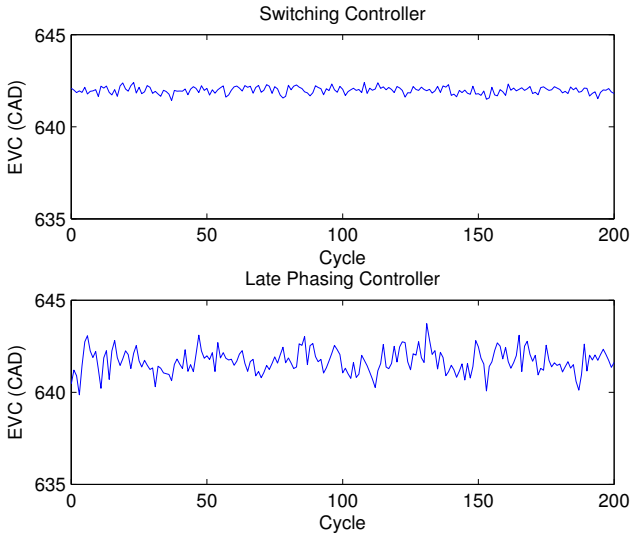

Figure 5.4: Closed-loop early phasing operation: EVC

5.2.3 Trajectory Tracking

In this experiment, the switching controller and the early-phasing controller track a desired θ_{50} trajectory indicated by the red lines in Fig. 5.5. As seen in the top plot of Fig. 5.5, the switching controller accurately tracks the desired trajectory, and is able to maintain a fairly small variance in θ_{50} throughout the experiment. In the bottom plot of Fig. 5.5, the early-phasing controller allows more combustion timing variance and finally does a very poor job of maintaining a constant combustion timing when the desired θ_{50} reaches 9 CAD after TDC. The input trajectories associated with this experiment are shown in Fig. 5.6.

As demonstrated in this section, the switching controller acknowledges the change in system behavior and applies the appropriate cycle-by-cycle control. The results show that it is able to track a wide range of desired θ_{50} command and improve the variance of combustion phasing over late-phasing, open-loop operation. Slightly different tuning of feedback controllers also show comparable results, suggesting that the performance demonstrated in this section is not, in general, sensitive to minor changes in the control gains.

Based on the switching linear model presented in Chapter 4, it is also possible to

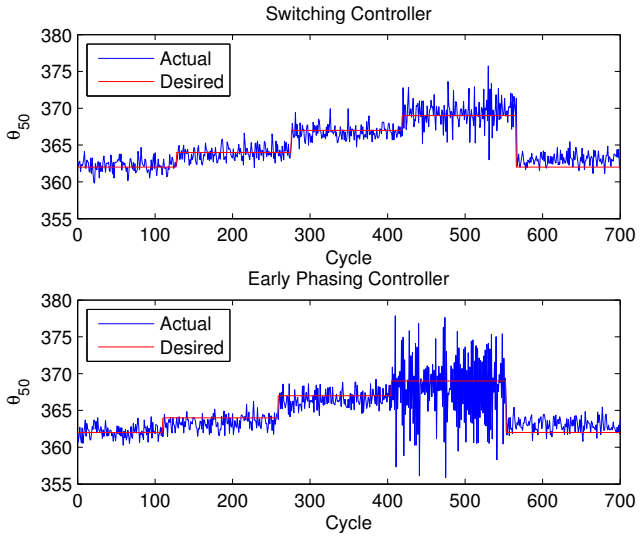

Figure 5.5: Trajectory tracking in closed-loop: blue-(actual θ_{50}), red-(desired θ_{50})

synthesis a model predictive controller (MPC) as presented by Widd *et al.* in [62]. Particularly, this formulation allow the controller to foresee how the system dynamics are going to change in the future and can plan the input trajectory proactively. As a result, the MPC in [62] shows less overshoot when a large step change in θ_{50} is commanded.

5.3 Stability of the Switching Linear Model

Although commonly employed in practice, it is well known that even switching between a number of *stable* linear systems can create *instability*. In this section, the stability properties of the switching linear model is established. Furthermore, while Equations (4.5) describe a simplified model, it is a reasonable approximation to the testbed as shown in Fig. 4.9. Therefore, the following stability analysis can be viewed as a preliminary investigation of global stability of the recompression HCCI.

In Section 5.3.1, the problem of finding a Lyapunov function for the switching linear model is phrased as a semi-definite program (SDP). This shows that the model

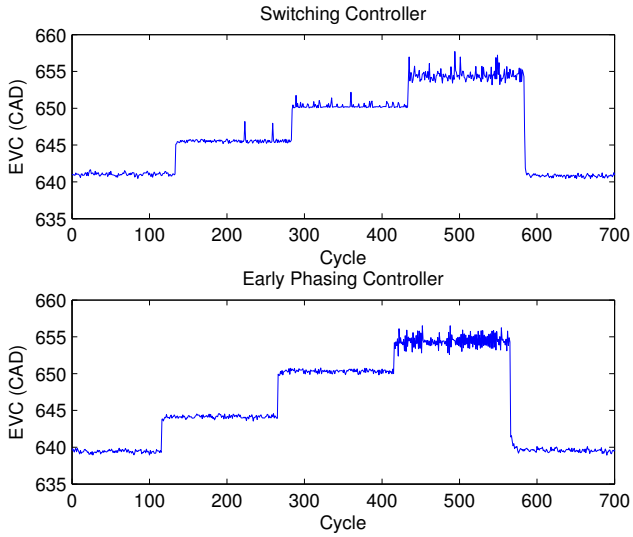

Figure 5.6: Trajectory tracking in closed-loop: EVC

is exponentially stable about the origin, i.e. about $x = \mathbf{0}$. Since the model in Equations (4.5) is fundamentally nonlinear, this stability statement does not automatically generalize to other equilibria achieved by non-zero constant inputs. In Section 5.3.2, another SDP formulation is demonstrated to establish general stability statements about equilibria other than the origin.

5.3.1 Exponential Stability about the Origin

Define a quadratic Lyapunov function V:

$$V_k = x_k^T \cdot P \cdot x_k \tag{5.15}$$

where

P *is a symmetric positive definite matrix*

k *is the cycle index*

To prove that the states of Equations (4.5) return to the origin at an exponential rate of γ, the following dissipation rate equation needs to hold for all x_k:

$$\begin{aligned}\Delta V_k &= V_k - V_{k+1} \\ &= x_k^T \cdot P \cdot x_k - x_{k+1}^T \cdot P \cdot x_{k+1} \\ &\geq \gamma \cdot V_k \\ &= \gamma \cdot x_k^T \cdot P \cdot x_k, \qquad for\ all\ x_k\ and\ some\ \gamma > 0 \end{aligned} \tag{5.16}$$

Substituting the system dynamics (4.5) into Equation (5.16) assuming zero input gives the following inequality:

$$\begin{aligned} &x_k^T \cdot P \cdot x_k - x_k^T \cdot A_i^T \cdot P \cdot A_i \cdot x_k - d_i^T \cdot P \cdot d_i - 2 \cdot d_i^T \cdot P \cdot A_i \cdot x_k \\ &\quad \geq \gamma \cdot x_k^T \cdot P \cdot x_k, \qquad if\ x_k \in \Omega_i \end{aligned} \tag{5.17}$$

where Ω_i is defined in Equation (4.6).

Equation (5.17) means that, at any time step k, the value of the Lyapunov function should decrease according to (5.16). Furthermore, the propagation of x_k follows one of the three sets of linear dynamics depending on which region x_k resides. Alternatively, (5.17) can be expressed in a quadratic form:

$$\begin{aligned} &\begin{bmatrix} x_k \\ 1 \end{bmatrix}^T \begin{bmatrix} P - A_i^T \cdot P \cdot A_i - \gamma \cdot P & -A_i^T \cdot P \cdot d_i \\ -d_i^T \cdot P \cdot A_i & -d_i^T \cdot P \cdot d_i \end{bmatrix} \begin{bmatrix} x_k \\ 1 \end{bmatrix} \geq 0, \\ &\quad if\ x_k \in \Omega_i, \quad i = 1, 2, 3 \end{aligned} \tag{5.18}$$

Note that (5.18) is a set of three inequalities. However, only one of them needs to hold at any given time step, since the state can only exist in only one of three regions at any time step. This additional constraint is addressed in the following subsections.

Partition of State Space

The three operating regions are defined previously in Equation (4.6). These partitions of the state space can be expressed in a format that is more convenient to the

formulation. In general, the regions described in Equation (4.6) can be expressed as follows:

$$
\begin{aligned}
& x_k \in \Omega_i \quad if: \\
& \begin{bmatrix} x_k \\ 1 \end{bmatrix}^T \begin{bmatrix} \mathbf{0} & n \\ n^T & -T_{i,l} \end{bmatrix} \begin{bmatrix} x_k \\ 1 \end{bmatrix} \geq 0 \\
& and \\
& \begin{bmatrix} x_k \\ 1 \end{bmatrix}^T \begin{bmatrix} \mathbf{0} & -n \\ -n^T & T_{i,u} \end{bmatrix} \begin{bmatrix} x_k \\ 1 \end{bmatrix} \geq 0
\end{aligned} \tag{5.19}
$$

where

$$n = \begin{bmatrix} 0 & 0.5 \end{bmatrix}^T$$

With the three regions defined in (5.19), the three dissipation inequalities (5.18) can be expressed as:

$$
\begin{bmatrix} x_k \\ 1 \end{bmatrix}^T \begin{bmatrix} P - A_i^T \cdot P \cdot A_i - \gamma \cdot P & -A_i^T \cdot P \cdot d_i \\ -d_i^T \cdot P \cdot A_i & -d_i^T \cdot P \cdot d_i \end{bmatrix} \begin{bmatrix} x_k \\ 1 \end{bmatrix} \geq 0 \tag{5.20}
$$

$$
\begin{aligned}
& whenever \\
& \begin{bmatrix} x_k \\ 1 \end{bmatrix}^T \begin{bmatrix} \mathbf{0} & n \\ n^T & -T_{i,l} \end{bmatrix} \begin{bmatrix} x_k \\ 1 \end{bmatrix} \geq 0 \\
& \begin{bmatrix} x_k \\ 1 \end{bmatrix}^T \begin{bmatrix} \mathbf{0} & -n \\ -n^T & T_{i,u} \end{bmatrix} \begin{bmatrix} x_k \\ 1 \end{bmatrix} \geq 0
\end{aligned}
$$

A sufficient condition for (5.20) can be obtained by replacing the 1 in the formulation with a general variable v:

$$\begin{bmatrix} x_k \\ v \end{bmatrix}^T \begin{bmatrix} P - A_i^T \cdot P \cdot A_i - \gamma \cdot P & -A_i^T \cdot P \cdot d_i \\ -d_i^T \cdot P \cdot A_i & -d_i^T \cdot P \cdot d_i \end{bmatrix} \begin{bmatrix} x_k \\ v \end{bmatrix} \geq 0 \qquad (5.21)$$

whenever

$$\begin{bmatrix} x_k \\ v \end{bmatrix}^T \begin{bmatrix} \mathbf{0} & n \\ n^T & -T_{i,l} \end{bmatrix} \begin{bmatrix} x_k \\ v \end{bmatrix} \geq 0$$

$$\begin{bmatrix} x_k \\ v \end{bmatrix}^T \begin{bmatrix} \mathbf{0} & -n \\ -n^T & T_{i,u} \end{bmatrix} \begin{bmatrix} x_k \\ v \end{bmatrix} \geq 0$$

Apparently, for any pair of $x_k = \mathbf{a}$ and $v = b \neq 0$ that satisfy (5.21), $x_k = \mathbf{a}/b$ satisfies (5.20).

This means that if the states are in the i_{th} HCCI region defined by the bottom two inequalities of (5.21), then the dissipation rate of the Lyapunov function satisfies the top inequality of (5.21). Furthermore, this dissipation rate is based on the linear dynamics specific to the i_{th} HCCI region.

The S-Procedure

A proof of the S-Procedure can be found in [63]. Essentially, the S-Procedure aims at answering the following question:

For all z, when does $z^T \cdot Q_1 \cdot z \geq 0$, $z^T \cdot Q_2 \cdot z \geq 0$, ..., $z^T \cdot Q_n \cdot z \geq 0$ imply $z^T \cdot Q_0 \cdot z \geq 0$?
where Q_0, Q_1, ..., Q_n are symmetric matrices.

In other words, when do the non-negativities of multiple quadratic forms imply the non-negativity of a single quadratic form?

A sufficient condition given by the S-Procedure is the existence of non-negative scalars

τ_1, τ_2, ..., τ_n such that the following matrix inequality holds:

$$Q_0 \succeq \tau_1 \cdot Q_1 + \tau_2 \cdot Q_2 + \ldots + \tau_1 \cdot Q_n \tag{5.22}$$

Using the S-Procedure, a sufficient condition for (5.21) can be expressed as:

$$\begin{bmatrix} P - A_i^T \cdot P \cdot A_i - \gamma \cdot P & -A_i^T \cdot P \cdot d_i \\ -d_i^T \cdot P \cdot A_i & -d_i^T \cdot P \cdot d_i \end{bmatrix} \succeq \tau_i \begin{bmatrix} \mathbf{0} & n \\ n^T & -T_{i,l} \end{bmatrix} + \phi_i \begin{bmatrix} \mathbf{0} & -n \\ -n^T & T_{i,u} \end{bmatrix} \tag{5.23}$$

$$\tau_i \geq 0, \quad \phi_i \geq 0 \tag{5.24}$$

For each HCCI region, a pair of non-negative τ and ϕ is required to guarantee (5.21). Note that (5.23) is affine in the variables P, τ and ϕ. Therefore, the problem of simultaneously finding P, τ and ϕ to satisfy (5.23) can be phrased as a semi-definite programming (SDP) problem which is a class of convex optimization problems [63]. *CVX* [64], a software that solves convex optimization problems in Matlab, is used to simultaneously find P, τ and ϕ that satisfy the following feasibility problem for all $i = 1, 2, 3$:

$$\begin{aligned} &\textit{Find} \quad P,\ \tau_i,\ \phi_i \\ &\textit{subject to} \\ &\tau_i \geq 0 \\ &\phi_i \geq 0 \\ &\begin{bmatrix} P - A_i^T \cdot P \cdot A_i - \gamma \cdot P & -A_i^T \cdot P \cdot d_i \\ -d_i^T \cdot P \cdot A_i & -d_i^T \cdot P \cdot d_i \end{bmatrix} \succeq \tau_i \begin{bmatrix} \mathbf{0} & n \\ n^T & -T_{i,l} \end{bmatrix} + \phi_i \begin{bmatrix} \mathbf{0} & -n \\ -n^T & T_{i,u} \end{bmatrix} \end{aligned} \tag{5.25}$$

The dissipation rate γ is supplied to the above SDP and can be increased until the formulation can no longer find a P to satisfy (5.25). This formulation can be readily generalized to discuss closed loop stability by replacing system matrices A_i with $A_i - B_i \cdot K_i$. Using this method, a P that proves exponential stability of both the

open and closed loop system is found:

$$P = \begin{bmatrix} 0.4286 & 1.0508 \\ 1.0508 & 27.8916 \end{bmatrix}$$

The dissipation rate, γ, associated with this Lyapunov function is 0.5816.

5.3.2 General Stability Statement

Since the switching mechanism in (4.5) is fundamentally nonlinear, the stability statement established around the origin is not readily generalizable to other equilibria. In this section, this problem is addressed in a two-step process. First, the equilibrium achieved by a steady state input is derived. In the second step, all the initial conditions are shown to eventually converge to this unique equilibrium. As before, the following analysis is easily generalized to discuss closed loop stability by replacing A_i with $A_i - B_i \cdot K_i$ in the formulation.

With the temperature thresholds for each region chosen according to (4.9) and (4.11), a constant input u_{ss} results in an unique equilibrium, x_{ss}. Assuming this equilibrium, x_{ss}, resides in the j_{th} HCCI region, the following equation has to hold:

$$x_{ss} = A_j \cdot x_{ss} + B_j \cdot u_{ss} + d_j \qquad x_{ss} \in \Omega_j \tag{5.26}$$

Solving for x_{ss} gives:

$$x_{ss} = (I - A_j)^{-1} \cdot (B_j \cdot u_{ss} + d_j) \qquad x_{ss} \in \Omega_j \tag{5.27}$$

Define $\overline{x}_k = x_k - x_{ss}$. Essentially, $\overline{x}_k$ measures the deviation from the equilibrium x_{ss}. Our goal is to find a symmetric positive definite matrix P that satisfies the following:

$$\overline{V}_k = \overline{x}_k^T \cdot P \cdot \overline{x}_k \tag{5.28}$$

$$\Delta\overline{V}_k = \overline{x}_k^T \cdot P \cdot \overline{x}_k - \overline{x}_{k+1}^T \cdot P \cdot \overline{x}_{k+1} \geq \overline{x}_k^T \cdot Q \cdot \overline{x}_k \tag{5.29}$$

where

Q is a symmetric positive definite matrix

In other words, $\overline{V}_k$ is always decreasing when $\overline{x} \neq \mathbf{0}$, which shows $\overline{x}$ returns to the origin asymptotically, or, equivalently, x returns to x_{ss} asymptotically.

The switching linear model can be expressed in terms of $\overline{x}$ in place of x:

$$\begin{aligned} &\overline{x}_{k+1} = A_i \cdot \overline{x}_k + B_i \cdot u_k + d_i + (A_i - I) \cdot x_{ss} \\ &\text{if } \overline{x}_k \in \overline{\Omega}_i, \qquad i = 1, 2, 3 \end{aligned} \tag{5.30}$$

Note that the region definition, $\overline{\Omega}_i$, is different due to the change of coordinates from x to $\overline{x}$. Specifically:

$$\overline{\Omega}_i \triangleq \left\{ \overline{x} : S_i \overline{x} \leq \overline{R}_i \right\} \tag{5.31}$$

where

$$\begin{aligned} \overline{R}_i &= \begin{bmatrix} T_{i,u} \\ -T_{i,l} \end{bmatrix} - \begin{bmatrix} 0 & 1 \\ 0 & -1 \end{bmatrix} \cdot x_{ss} \\ &= \begin{bmatrix} \overline{T}_{i,u} \\ -\overline{T}_{i,l} \end{bmatrix} \end{aligned}$$

The switching thresholds for (5.30) are simply shifted by the equilibrium temperature, given in the second element of x_{ss}. These shifted thresholds are denoted as $\overline{T}_{i,u}$ and $\overline{T}_{i,l}$. As the input is held constant at u_{ss}, $\overline{x}$ propagates from cycle to cycle according to:

$$\overline{x}_{k+1} = A_i \cdot \overline{x}_k + z_i \quad \text{if } \overline{x}_k \in \overline{\Omega}_i, \qquad i = 1, 2, 3 \tag{5.32}$$

where

$$z_i = B_i \cdot u_{ss} + d_i + (A_i - I) \cdot x_{ss}$$

Much like the derivation in the previous section, the dissipation of the Lyapunov

function can be expressed in a quadratic form:

$$\begin{bmatrix} \overline{x}_k \\ 1 \end{bmatrix}^T \begin{bmatrix} P - A_i^T \cdot P \cdot A_i - Q & -A_i^T \cdot P \cdot z_i \\ -z_i^T \cdot P \cdot A_i & -z_i^T \cdot P \cdot z_i \end{bmatrix} \begin{bmatrix} \overline{x}_k \\ 1 \end{bmatrix} \geq 0, \qquad if\ \overline{x}_k \in \overline{\Omega}_i \tag{5.33}$$

Note the similarity between (5.33) and (5.18). Not surprisingly, proving stability for the equilibrium, x_{ss}, ultimately reduces to a formulation very similar to (5.25):

$$\begin{aligned} &Find \quad P,\ \tau_i,\ \phi_i \\ &\tau_i \geq 0 \\ &\phi_i \geq 0 \\ &\begin{bmatrix} P - A_i^T \cdot P \cdot A_i - Q & -A_i^T \cdot P \cdot z_i \\ -z_i^T \cdot P \cdot A_i & -z_i^T \cdot P \cdot z_i \end{bmatrix} \succeq \tau_i \begin{bmatrix} \mathbf{0} & n \\ n^T & -\overline{T}_{i,l} \end{bmatrix} + \phi_i \begin{bmatrix} \mathbf{0} & -n \\ -n^T & \overline{T}_{i,u} \end{bmatrix} \end{aligned} \tag{5.34}$$

However, finding a P for (5.34) only proves that x asymptotically converges to x_{ss}, which is a single equilibrium in the vast set of possible equilibria. In the remaining of this section, (5.34) is generalized such that a single P can prove a range of equilibria are asymptotically stable.

The last LMI in (5.34) can be re-written as:

$$\begin{bmatrix} P - A_i^T P A_i - Q & -A_i^T P z_i - \tau_i n + \phi_i n \\ -z_i^T P A_i - \tau_i n^T + \phi_i n^T & -z_i^T P z_i + \tau_i \overline{T} i, l - \phi_i \overline{T} i, u \end{bmatrix} \succeq 0 \tag{5.35}$$

A necessary and sufficient condition for (5.35) is:

$$\begin{bmatrix} P - Q & -\tau_i \cdot n + \phi_i \cdot n & A_i^T \\ -\tau_i \cdot n^T + \phi_i \cdot n^T & \tau_i \cdot \overline{T} i, l - \phi_i \cdot \overline{T} i, u & z_i^T \\ A & z_i & P^{-1} \end{bmatrix} \succeq 0 \tag{5.36}$$

$$P^{-1} \succ 0 \tag{5.37}$$

This is because (5.36) is positive semi-definite if and only if its Schur complement, χ, is positive semi-definite and P^{-1} is positive definite. The Schur complement χ is given as:

$$\begin{aligned}
\chi &= \begin{bmatrix} P-Q & -\tau_i \cdot n + \phi_i \cdot n \\ -\tau_i \cdot n^T + \phi_i \cdot n^T & \tau_i \cdot \overline{T}i, l - \phi_i \cdot \overline{T}i, u \end{bmatrix} - \begin{bmatrix} A_i^T \\ z_i^T \end{bmatrix} \cdot P \cdot \begin{bmatrix} A_i & z_i \end{bmatrix} \\
&= \begin{bmatrix} P-Q & -\tau_i \cdot n + \phi_i \cdot n \\ -\tau_i \cdot n^T + \phi_i \cdot n^T & \tau_i \cdot \overline{T}i, l - \phi_i \cdot \overline{T}i, u \end{bmatrix} - \begin{bmatrix} A_i^T \cdot P \cdot A_i & A_i^T \cdot P \cdot z_i \\ z_i^T \cdot P \cdot A_i & z_i^T \cdot P \cdot z_i \end{bmatrix} \\
&= \begin{bmatrix} P - A_i^T P A_i - Q & -A_i^T P z_i - \tau_i n + \phi_i n \\ -z_i^T P A_i - \tau_i n^T + \phi_i n^T & -z_i^T P z_i + \tau_i \overline{T}i, l - \phi_i \overline{T}i, u \end{bmatrix}
\end{aligned} \tag{5.38}$$

In the last line of (5.38), the Schur complement of the block matrix in (5.36) reduces to the block matrix in (5.35). Therefore, conditions (5.36) and (5.37) are indeed necessary and sufficient conditions for (5.35). Note that condition (5.37) is guaranteed automatically, since P is the Lyapunov function to be found which is positive definite. Condition (5.36) is no longer affine in P due to the existence of P^{-1}. Therefore, the problem cannot be readily phrased as a SDP. Defining a block diagonal matrix F:

$$F = \begin{bmatrix} I & 0 & 0 \\ 0 & I & 0 \\ 0 & 0 & P \end{bmatrix} \tag{5.39}$$

Multiplying (5.36) left and right by F does not change its definiteness. As a result, an equivalent condition for (5.36) is:

$$\begin{bmatrix} P-Q & -\tau_i \cdot n + \phi_i \cdot n & A_i^T \cdot P \\ -\tau_i \cdot n^T + \phi_i \cdot n^T & \tau_i \cdot \overline{T}i, l - \phi_i \cdot \overline{T}i, u & z_i^T \cdot P \\ P \cdot A & P \cdot z_i & P \end{bmatrix} \succeq 0 \tag{5.40}$$

The key difference between (5.40) and (5.35) is that the former is affine in z_i, while

the latter is quadratic in z_i. Furthermore, z_i is affine in u_{ss}:

$$\begin{aligned} z_i =& B_i \cdot u_{ss} + d_i + (A_i - I) \cdot x_{ss} \\ =& B_i \cdot u_{ss} + d_i + (A_i - I) \cdot (I - A_j)^{-1} \cdot (B_j \cdot u_{ss} + d_j) \\ =& \left[B_i + (A_i - I) \cdot (I - A_j)^{-1} \cdot B_j\right] \cdot u_{ss} + d_i + \left[(A_i - I) \cdot (I - A_j)^{-1}\right] \cdot d_j \end{aligned}$$

Therefore, (5.40) is affine in u_{ss}. Using the results in [65], if there exists a set of P, τ and ϕ that simultaneously satisfy (5.40) for two steady state inputs $u_{ss,1}$ and $u_{ss,2}$, then all the intermediate points between $u_{ss,1}$ and $u_{ss,2}$ are guaranteed to satisfy (5.40) for the same P, τ and ϕ. As a result, for the j_{th} HCCI region, a pair of $u_{ss,1}$ and $u_{ss,2}$ can be supplied to solve the following SDP:

$$\begin{aligned} &Find \quad P,\ \tau,\ \phi \\ &\tau_i \geq 0 \\ &\phi_i \geq 0 \\ &\begin{bmatrix} P - Q & -\tau_i \cdot n + \phi_i \cdot n & A_i^T \cdot P \\ -\tau_i \cdot n^T + \phi_i \cdot n^T & \tau_i \cdot \overline{T}i, l - \phi_i \cdot \overline{T}i, u & z_i^T \cdot P \\ P \cdot A & P \cdot z_i & P \end{bmatrix} \succeq 0 \\ &\begin{bmatrix} P - Q & -\tau_i \cdot n + \phi_i \cdot n & A_i^T \cdot P \\ -\tau_i \cdot n^T + \phi_i \cdot n^T & \tau_i \cdot \overline{T}i, l - \phi_i \cdot \overline{T}i, u & w_i^T \cdot P \\ P \cdot A & P \cdot w_i & P \end{bmatrix} \succeq 0 \\ &z_i = \left[B_i + (A_i - I) \cdot (I - A_j)^{-1} \cdot B_j\right] \cdot u_{ss,1} + d_i + \left[(A_i - I) \cdot (I - A_j)^{-1}\right] \cdot d_j \\ &w_i = \left[B_i + (A_i - I) \cdot (I - A_j)^{-1} \cdot B_j\right] \cdot u_{ss,2} + d_i + \left[(A_i - I) \cdot (I - A_j)^{-1}\right] \cdot d_j \end{aligned} \tag{5.41}$$

With this formulation, a Lyapunov function P found by the solver is paired with an interval of steady state inputs. Any equilibria achieved by the steady inputs within this interval are proven globally, asymptotically stable.

5.4 Conclusion

In this chapter, the three-region switching controller is shown to track a wide range of desired θ_{50} commands while maintaining a small variance in combustion timing. Particularly, the ill-behaved late phasing operating point shown in the bottom plot of Fig. 4.1 is rendered usable with appropriate cycle-by-cycle feedback. Essentially, the permissible operating range of recompression HCCI is expanded in closed loop. The effectiveness of this controller is based on the switching linear model presented in Chapter 4, which captures the qualitative change in system dynamics.

In the last part of this chapter, two SDP formulations are presented to guarantee that the switching control/model framework is stable. Since the three-region switching linear model is a reasonable approximation of the engine testbed, the stability analysis also provides a preliminary investigation of stability of recompression HCCI.

Chapter 6

The Linear Parameter Varying Model

In Chapter 5, the switching controller is proved stable with the switching linear model. It is desirable to further examine the stability of this controller when paired with the nonlinear model, which has richer dynamics compared to the switching linear model and more accurately reflects the physical system. Apart from the closed-loop behavior, it is also of interest to understand the fundamental stability and robustness characteristics of recompression HCCI.

Qualitatively, stability analysis aims to make collective statements about the boundedness of state trajectories *without* explicitly calculating every possible trajectory. Using this notion, robustness analysis aims to make this type of collective statement in the presence of model uncertainty and disturbance. However, this is not always easy with nonlinear systems, especially when the model complexity increases. While the nonlinear model is relatively simple among HCCI models, its algebraic complexity still poses a challenge in analyzing its state trajectory collectively. To address this, this chapter first examines the nonlinear model in greater detail and reveals an inherent structure in its state propagation equations (3.19). This insight suggests the possibility of approximating the NL model with a linear parameter varying (LPV)

model, which has the following general from:

$$x(k+1) = A(\rho) \cdot x(k) + B(\rho) \cdot u(k) \tag{6.1}$$

$$y(k) = C(\rho) \cdot x(k) \tag{6.2}$$

where ρ is a vector of varying parameters.

Essentially, both the oxygen and temperature state of the NL are first propagated by two fundamentally nonlinear equations, followed by two "linear-like" equations. As a result, the major nonlinearity of the NL model can be lumped into two varying parameters. By using a set of linear equations to approximate the "linear-like" stages of the NL model, a LPV model that has a similar format to Equation (6.1) can be obtained. This LPV model is evaluated in various simulations and shows very close agreement to the NL model in all cases, making it essentially equivalent to the nonlinear model.

In addition to its elegant structure, the LPV model presented in this chapter exhibits two important features. Firstly, one of the varying parameters is a "bowl-shaped" function of the states, or, in mathematical terms, a convex function of the model states. Without ever knowing its function value, a convex function embeds a number of properties in its graph. As a result, Chapter 7 presents an approach to collectively bound the state trajectories of the LPV model by exploiting the properties of convex functions. Secondly, the system matrices of the LPV model are affinely dependent on the other varying parameter, which is of known range and corresponds to a bounded model uncertainty. Chapter 7 further takes advantage of this property to make statements about the state trajectories in the presence of model uncertainty through checking a finite number of corner conditions.

6.1 What is Nonlinear about the Nonlinear Model?

The graphical analysis presented in Chapter 4 actually shows evidence of linearity in the breathing stage of the NL model. The map shown in Fig. 4.4 appears to be a family of *evenly-spaced parallel lines*. This suggests that part of the temperature

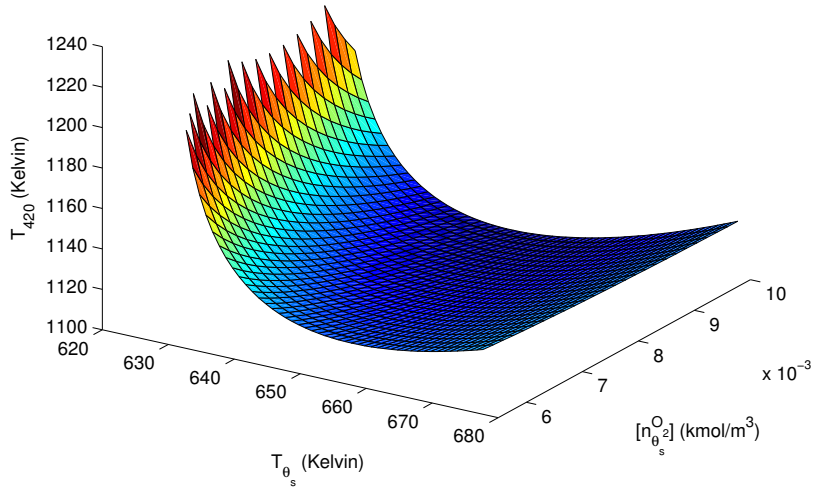

Figure 6.1: Temperature propagation during the combustion stage

propagation equation (3.19), g, is actually quite linear within the range of the variable values of interest.

To further expose the underlying structure of the nonlinear model, the temperature state propagation equation in (3.19) is again broken into two stages at the engine position of 300 CAD and 420 CAD. The characteristics of the two stages are examined *without* any of the simplifications used in Chapter 4.

6.1.1 Temperature Propagation: The Combustion Stage

The temperature propagation during the combustion stage, from 300 CAD to 420 CAD, is given as follows:

$$\begin{aligned} T_{420}(k) =& T_{\theta_s}(k) \cdot V_{\theta_s}^{\kappa_1 - 1} \cdot V_{ign}(k)^{\kappa_2 - \kappa_1} \cdot V_{eoc}(k)^{\kappa_3 - \kappa_2} \cdot V_{420}^{1-\kappa_3} \\ &+ \frac{E \cdot n_{\theta_s}^f(k) \cdot R \cdot V_{eoc}(k)^{\kappa_3 - 1} \cdot V_{420}^{1-\kappa_3} \cdot T_{\theta_s}(k)}{R \cdot T_{\theta_s}(k) \cdot (C_{v,f} - C_v) \cdot n_{\theta_s}^f + C_v \cdot p_{\theta_s} \cdot V_{\theta_s}} \end{aligned} \tag{6.3}$$

The first term on the right-hand-side (RHS) of Equation (6.3) is the temperature at 420 CAD in the absence of a combustion event, and the state temperature is simply propagated by a series of polytropic proceses to reach 420 CAD. The second term on the RHS is the contribution from the instantaneous energy addition at the end of combustion. Note that V_{ign} and V_{eoc} are both functions of the ignition timing, which, in turn, is an *implicit* function of both the oxygen content and temperature state based on the Arrhenius model (3.2). Nevertheless, it is convenient to assume that there exists an explicit function, g_{comb}, summarizing the relationship between the exhaust temperature and the model states:

$$T_{420}(k) = g_{comb}\big(T_{\theta_s}(k), n_{\theta_s}^{O_2}(k)\big) \tag{6.4}$$

This function, g_{comb}, greatly reduces the complexity of notations in this thesis. The temperature propagation during the combustion stage can be graphed within a range of state values of interest as shown in Fig. 6.1. The oxygen content state is divided by the cylinder volume at the state definition point, 300 CAD, and is plotted as an intensive property. The same normalization is used whenever the number of moles of gas is plotted in this thesis. The graph of g_{comb} shows that the exhaust temperature is much more sensitive to change in the temperature state than oxygen state, agreeing with the assumptions used in Chapter 4. The same "bowl-shaped" characteristics emerge in this 2-D map. The 1-D combustion map shown in Fig. 4.2 is a steady-state projection of Fig. 6.1.

This bowl-shaped feature is further characterized as the convexity of g_{comb} in Chapter 7. Qualitatively, g_{comb} being a convex function enforces certain trends in its mapping *without* knowing exactly what the function value is. This is very useful in Chapter 7 to make collective statements about the state trajectories.

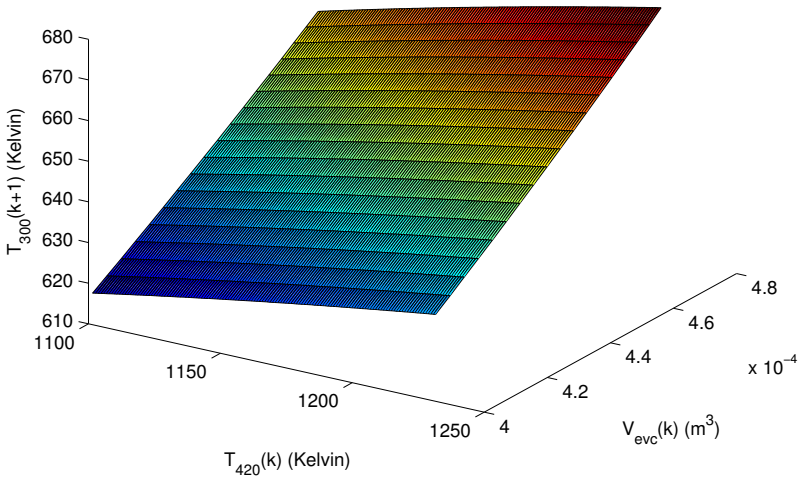

Figure 6.2: A 2-D slice of the temperature propagation during the breathing stage

6.1.2 Temperature Propagation: The Breathing Stage

The temperature propagation during the breathing stage, is given as follows:

$$T_{\theta_s}(k+1) = \frac{p^{im} \cdot {V_{ivc}}^{\kappa_7} \cdot {V_{\theta_s}}^{1-\kappa_7}}{R \cdot \left[n_{ivo}(k) + n^{ind}(k)\right]} \tag{6.5}$$

where

$$n_{ivo}(k) = p^{em\,\frac{1}{\kappa_4}} \cdot V_{420}^{\frac{1-\kappa_3}{\kappa_4}} \cdot R^{\frac{-1}{\kappa_4}} \cdot T_{420}(k)^{\frac{-1}{\kappa_4}} \cdot n_{\theta_s}(k)^{\frac{\kappa_4-1}{\kappa_4}} \cdot V_{evc}(k) \cdot V_{evo}(k)^{\frac{\kappa_3-\kappa_4}{\kappa_4}} \tag{6.6}$$

$$\begin{aligned} n^{ind}(k) =& \frac{C_v}{C_p \cdot R \cdot T^{im}} \Bigg[p^{im} \cdot V_{ivc} - p^{em} \cdot V_{evc}(k) - \frac{h \cdot R \cdot T^{wall}}{C_v} \\ &+ \frac{h}{2 \cdot C_v} R^{\frac{1}{\kappa_4}} \cdot p^{em\,\frac{\kappa_4-1}{\kappa_4}} \cdot V_{420}^{\frac{\kappa_3-1}{\kappa_4}} \cdot n_{\theta_s}(k)^{\frac{1-\kappa_4}{\kappa_4}} \cdot T_{420}(k)^{\frac{1}{\kappa_4}} \left(1 + (\frac{V_{evc}(k)}{V^{tdc}})^{\gamma-1}\right) V_{evo}(k)^{\frac{\kappa_4-\kappa_3}{\kappa_4}} \Bigg] \end{aligned} \tag{6.7}$$

As can be seen, the temperature state on cycle $k+1$ is a function of the exhaust temperature $T_{420}(k)$, exhaust valve timing $V_{evc}(k)$ and the total amount of gas at the

state definition point $n_{\theta_s}(k)$. Note that $n_{\theta_s}(k)$ can be further related to $T_{\theta_s}(k)$ based on the ideal gas law and the assumption that the pressure at the state definition point is fixed at $p^{im} \cdot \left(\frac{V_{ivc}}{V_{\theta_s}}\right)^{\kappa_7}$, i.e. the intake manifold pressure propagated by a polytropic compression. Therefore, the temperature propagation during the breathing stage can be expressed compactly as:

$$T_{\theta_s}(k+1) = g_{breath}\big(T_{\theta_s}(k), T_{420}(k), V_{evc}(k)\big) \tag{6.8}$$

This function, g_{breath}, is much more sensitive to change in $T_{420}(k)$ and $V_{evc}(k)$ than $T_{\theta_s}(k)$. Therefore, a 2-D slice of g_{breath} with $T_{420}(k)$ on the x-axis and $V_{evc}(k)$ on the y-axis is shown in Fig. 6.2. As can be seen, the breathing stage is indeed very linear in these two variables over a wide range of V_{evc} and T_{420}. Note that the V_{evc} range translates to EVC change of 17 CAD and the range of T_{420} in Fig. 6.2 covers the range of z-axis shown in Fig. 6.1. Different T_{θ_s} generate surfaces that are roughly parallel to the one shown in Fig. 6.2. Qualitatively, the linear-like behavior shown in Fig. 6.2 comes from the roughly linear nature in the energy balance during the mixing process.

In the temperature propagation equation of the NL model (3.19), g, a clear linear-nonlinear separation can be observed, with the major nonlinearity of the nonlinear model existing in the combustion stage. The full-cycle propagation equation, g, can be formed by combining g_{comb} and g_{breath}:

$$\begin{aligned} T_{\theta_s}(k+1) &= g(n_{\theta_s}^{O_2}(k),\ T_{\theta_s}(k),\ V_{EVC}(k)) \\ &= g_{breath}\Big(T_{\theta_s}(k),\ g_{comb}\big(T_{\theta_s}(k), n_{\theta_s}^{O_2}(k)\big),\ V_{evc}(k)\Big) \end{aligned}$$

6.1.3 Oxygen Content Propagation

Similar separation can be achieved with oxygen propagation equation. The full cycle equation for oxygen content is:

$$n_{\theta_s}^{O_2}(k+1) = \big(n_{\theta_s}^{O_2}(k) - \lambda_{stoich} \cdot n_{\theta_s}^{f}\big) \cdot \zeta + \chi \cdot n^{ind}(k) \tag{6.9}$$

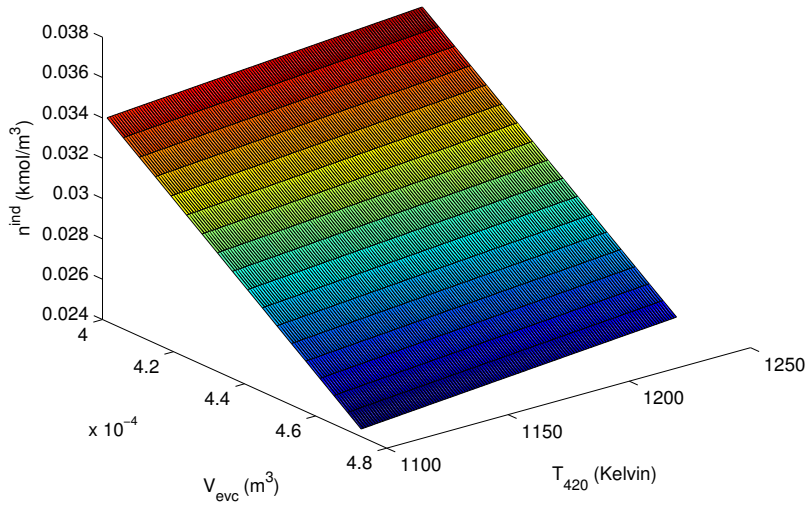

Figure 6.3: A 2-D slice of the inducted air as a function of V_{evc} and T_{420}

where

λ_{stoich} is the stoichiometric air-fuel ratio

ζ is the trapped ratio: the percentage of the amount exhaust trapped at EVC

n^{ind} is the amount of air inducted and is given in Equation (6.7) as a function of T_{θ_s}, V_{evc} and T_{420}

χ is the oxygen molar ratio in air

The term in the parenthesis on the RHS of equation (6.9) is the amount of leftover oxygen after combustion. When this amount is further multiplied by the trap ratio, the term represents the oxygen content at EVC. Therefore, the total oxygen amount on the *next* cycle is the sum of the oxygen content at EVC and the oxygen content inducted during the intake stroke.

It turns out that the amount of air inducted n^{ind}, is roughly linear in T_{θ_s}, V_{evc} and T_{420} as well. A 2-D slice of Equation (6.7) is shown in Fig. 6.3. On the other hand, the first term in Equation (6.9) is a product of $n_{\theta_s}^{O_2}$ and ζ. Since the trap ratio, ζ,

is a strong function of the EVC command, this represents the major nonlinearity in the oxygen propagation equation, i.e. a product of the state and the input, which is inherent to recompression HCCI due to the retained exhaust.

6.2 The Linear Parameter Varying HCCI Model

In the previous section, the nonlinear model exhibits a clear "linear-nonlinear" separation in both the oxygen content and temperature propagation equations. Particularly, each of the two states is first propagated by a nonlinear equation, the output of that nonlinear equation is then propagated by a "linear-like" equation to the state definition point on the next engine cycle. With this insight, a linear parameter varying (LPV) model can be formulated based on the nonlinear model. The first step in arriving at this model structure is to approximate the breathing stage equations with their linearizations. Specifically:

$$T_{\theta_s}(k+1) \cong C_1 + C_2 \cdot T_{\theta_s}(k) + C_3 \cdot T_{420}(k) + C_4 \cdot V_{evc}(k) \tag{6.10}$$

$$n^{ind}(k) \cong C_5 + C_6 \cdot T_{\theta_s}(k) + C_7 \cdot T_{420}(k) + C_8 \cdot V_{evc}(k) \tag{6.11}$$

where

C_1 is the equilibrium temperature state of the linearized point

$C_2 \sim C_4$ are the elements of the gradient of Equation (6.8) at the linearized point

C_5 is the equilibrium inducted air of the linearized point

$C_6 \sim C_8$ are the elements of the gradient of Equation (6.7) at the linearized point

Substituting Equation (6.11) into Equation (6.9) gives:

$$\begin{aligned} n_{\theta_s}^{O_2}(k+1) = &\left(n_{\theta_s}^{O_2}(k) - \lambda_{stoich} \cdot n_{\theta_s}^{f}\right) \cdot \zeta \\ &+ \chi \cdot C_5 + \chi \cdot C_6 \cdot T_{\theta_s}(k) + \chi \cdot C_7 \cdot T_{420}(k) + \chi \cdot C_8 \cdot V_{evc}(k) \end{aligned}$$

With this, a linear parameter varying model is formed:

$$\begin{bmatrix} n^{O_2}(k+1) \\ T_{\theta_s}(k+1) \end{bmatrix} = \begin{bmatrix} \zeta(k) & \chi \cdot C_6 \\ 0 & C_2 \end{bmatrix} \cdot \begin{bmatrix} n^{O_2}(k) \\ T_{\theta_s}(k) \end{bmatrix} + \begin{bmatrix} \chi \cdot C_7 \\ C_3 \end{bmatrix} \cdot T_{420}(k) + \begin{bmatrix} \chi \cdot C_8 \\ C_4 \end{bmatrix} \cdot V_{evc}(k) + \begin{bmatrix} \chi \cdot C_5 - \zeta(k) \cdot \lambda_{stoich} \cdot n^f_{\theta_s} \\ C_1 \end{bmatrix} \quad (6.12)$$

The trap ratio, ζ, and the exhaust temperature, T_{420}, are the varying parameters in this model. The output equation of this LPV model remains the same as the nonlinear model, that is

$$\theta_{50}(k) = \theta_{ign}(k) + 0.5 \cdot \theta^{durn}$$

where

$$\theta_{ign} = \left\{ \theta_\tau \;\middle|\; K_{th} = \int_{\theta_s}^{\theta_\tau} A \cdot e^{\frac{-E_a}{R \cdot T_\theta}} \cdot [n^{O_2}_{\theta_s}]^a \cdot [n^f_{\theta_s}]^b \cdot \frac{1}{\omega} \mathrm{d}\theta \right\}$$

Introducing the following notations:

$$\begin{aligned} A(\zeta) &= \begin{bmatrix} 0 & \chi \cdot C_6 \\ 0 & C_2 \end{bmatrix} + \zeta \cdot \begin{bmatrix} 1 & 0 \\ 0 & 0 \end{bmatrix} \\ B_1 &= \begin{bmatrix} \chi \cdot C_8 \\ C_4 \end{bmatrix} \\ B_2 &= \begin{bmatrix} \chi \cdot C_7 \\ C_3 \end{bmatrix} \\ d(\zeta) &= \begin{bmatrix} \chi \cdot C_5 \\ C_1 \end{bmatrix} + \zeta \cdot \begin{bmatrix} -\lambda_{stoich} \cdot n^f_{\theta_s} \\ 0 \end{bmatrix} \\ x &= \begin{bmatrix} n^{O_2}_{\theta_s} \\ T_{\theta_s} \end{bmatrix} \\ u &= V_{evc} \end{aligned} \quad (6.13)$$

Equation (6.12) can therefore be expressed compactly as:

$$x_{k+1} = A(\zeta) \cdot x_k + B_1 \cdot u_k + B_2 \cdot T_{420,k} + d(\zeta) \tag{6.14}$$

The model shown in Equation (6.14) does not exactly fit the general LPV definition shown in (6.1) due to the existence of the bias term $d + B_2 \cdot T_{420}$. However, based on the obvious resemblance in model structure, the HCCI model shown in (6.14) is still referred to as the LPV model in this thesis. Note that in (6.14), the A matrix is only a function of the trap ratio, whereas the bias in the equation depends on both varying parameters, i.e. the trap ratio and the exhaust temperature.

One important feature of (6.14) is that every system matrix is affinely dependent on the trap ratio, ζ. In addition, the trap ratio is typically bounded in the interval of [0.5 0.6] for recompression HCCI, i.e., 50∼60% of the exhaust is trapped in the cylinder. Therefore, any ζ in this range can be expressed as the convex combination of the two extremes of the interval, i.e.

$$\begin{aligned} \zeta &= \sum_{i=1}^{2} \theta_i \cdot \zeta^i, \quad \sum_{i=1}^{2} \theta_i = 1, \quad \theta_i \geq 0, \quad i = 1, 2 \\ \zeta^1 &= 0.5, \quad \zeta^2 = 0.6 \end{aligned}$$

Using the A matrix as an example, any allowable $A(\zeta)$ can be therefore expressed as:

$$\begin{aligned} A(\zeta) &= A\big(\sum_{i=1}^{2} \theta_i \cdot \zeta^i\big), \quad \sum_{i=1}^{2} \theta_i = 1, \quad \theta_i \geq 0, \quad i = 1, 2 \\ &= \sum_{i=1}^{2} \theta_i \cdot A\big(\zeta^i\big), \quad \sum_{i=1}^{2} \theta_i = 1, \quad \theta_i \geq 0, \quad i = 1, 2 \end{aligned}$$

Essentially, the above means that any allowable $A(\zeta)$ can be expressed as the convex combination of the two A matrices evaluated at the two extremes of ζ. This is very useful in Chapter 7 to show that even when the system states are propagated by an infinite number of possible system matrices due to the bounded uncertainty in the trap ratio, collective statements about the state trajectories can still be made by

checking a finite number of corner conditions.

6.3 Model Validation

In this section, the LPV model is subjected to various input and environmental parameter trajectories to show that it is essentially equivalent to the nonlinear model.

6.3.1 Sequence of Step Changes in EVC

Assuming the trap ratio, ζ, and the exhaust temperature, T_{420}, are known, the state trajectories of the LPV model are compared to those of the nonlinear model when subjected to the same step changes in EVC. The results are shown in Fig. 6.4 and Fig. 6.5.

In this particular test, the maximum error in the oxygen content is 4.01×10^{-6} $kmol/m^3$ and is three orders of magnitude smaller than the mean oxygen content shown in Fig. 6.4. This level of accurate agreement in the oxygen state is seen in all other numerical examples presented in this chapter. Therefore, the amount of inducted air, n^{ind}, is indeed very linear in T_{θ_s}, T_{420} and V_{evc} as proposed in Equation (6.11).

On the other hand, the temperature trajectory in Fig. 6.5 shows larger discrepancy compared to the oxygen trajectory but the two models still agree with each other well in transients and in steady state. In this particular test, the maximum error in the temperature is 0.49 Kelvin and the RMS error in the entire sequence is 0.29 Kelvin.

The θ_{50} response of the two models and the EVC trajectory used in this test is shown in Fig. 6.6 and in Fig. 6.7, respectively. The maximum difference in θ_{50} in this particular test is 0.29 CAD which is good across a range of maximum variation of roughly 10 CAD as shown in Fig. 6.6.

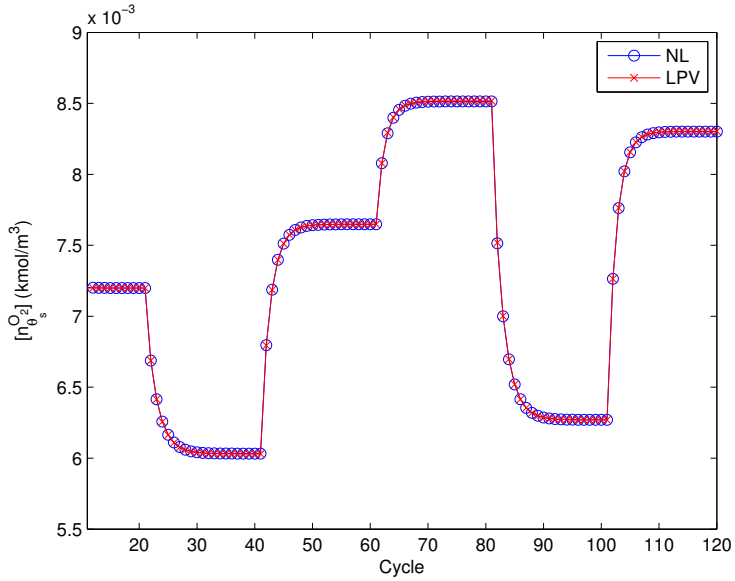

Figure 6.4: $[n_{\theta_s}^{O_2}]$ trajectory of the LPV and NL when subjected to the same EVC trajectory

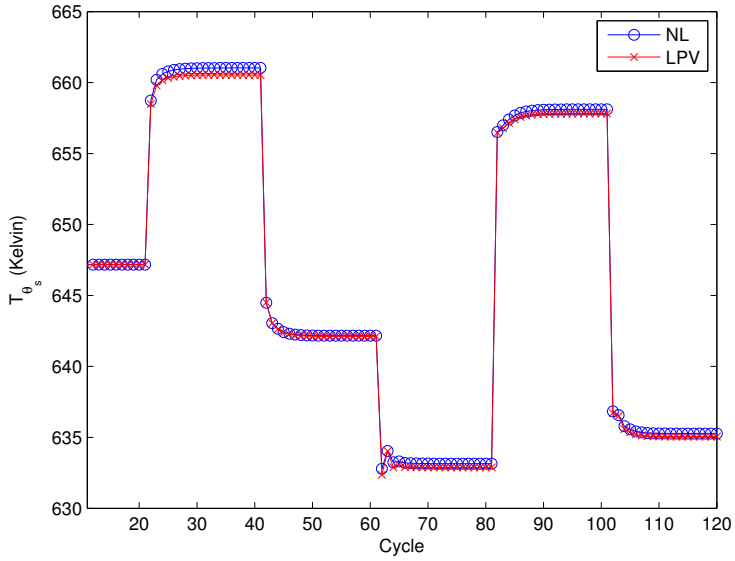

Figure 6.5: T_{θ_s} trajectory of the LPV and NL when subjected to the same EVC trajectory

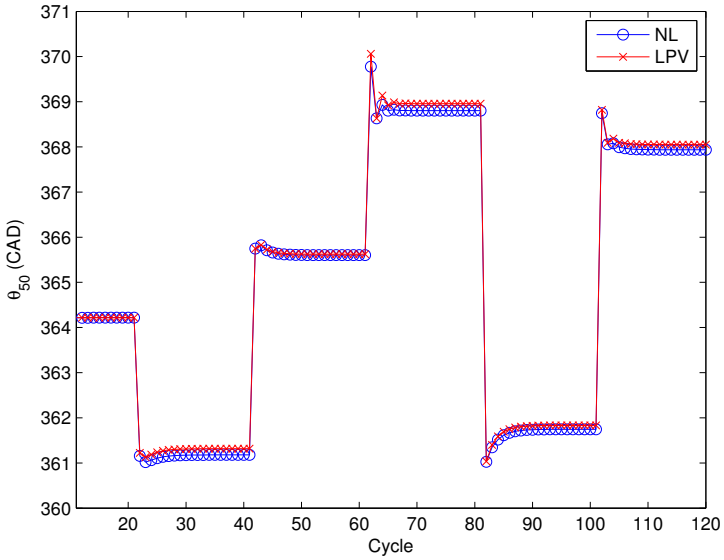

Figure 6.6: θ_{50} trajectory of the LPV and NL when subjected to the same EVC trajectory

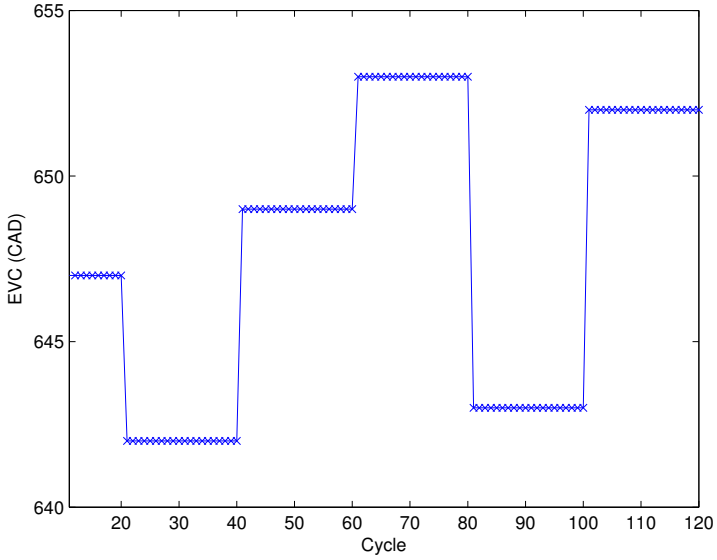

Figure 6.7: EVC trajectory

6.3.2 Random EVC Trajectory

In this section, a uniformly distributed EVC trajectory of 10000 cycle length is generated to drive the LPV and the nonlinear model. The lower and upper limits of the EVC command are 640 and 654 CAD, respectively. The resulting histograms of error in the oxygen content, temperature and θ_{50} of the two models are shown in Fig. 6.8, Fig. 6.9 an Fig. 6.10 (error is calculated as the values of the LPV minus those of the NL). All error in the oxygen state shown in Fig. 6.8 is three orders of magnitude smaller than the mean values of the two models and is, therefore, inconsequential. Even with this more dynamic EVC trajectory, the majority of the error in the temperature state is within a range of $\pm$ 0.5 Kelvin as shown in Fig. 6.9. The maximum error in temperature is roughly 0.8 Kelvin and occurs very infrequently. In Fig. 6.10, the difference in θ_{50} is small as well. The majority of the error is within a range of $\pm$ 0.25 CAD. The histogram of error in the temperature state, Fig. 6.9, shows a negative bias, indicating that the LPV model is more likely to underestimate the temperature state. As a result, the histogram of error in θ_{50}, Fig. 6.10, shows a positive bias, since underestimating the temperature state leads to overestimating θ_{50} in the LPV model.

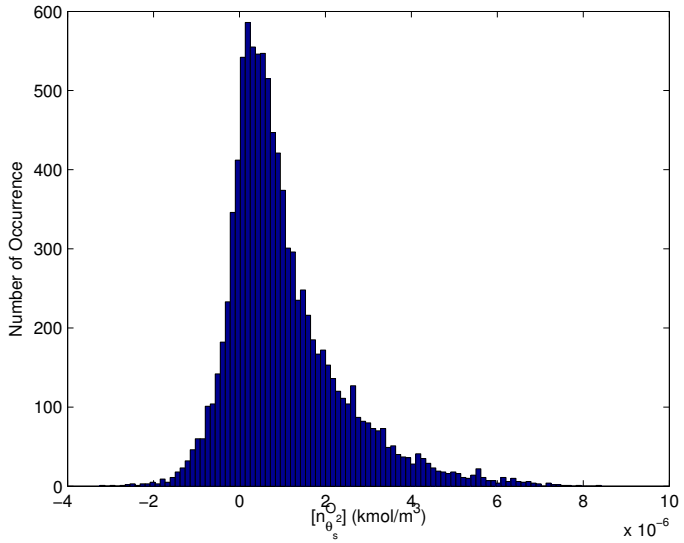

Figure 6.8: Histogram of error in $[n_{\theta_s}^{O_2}]$ between the LPV and NL

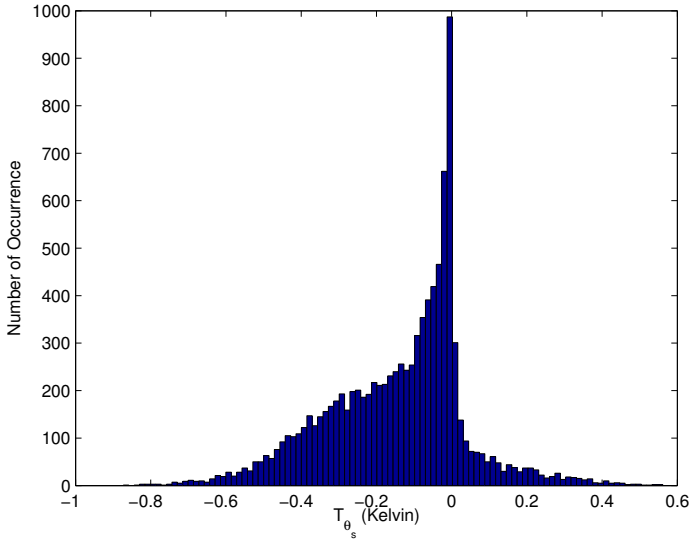

Figure 6.9: Histogram of error in T_{θ_s} between the LPV and NL

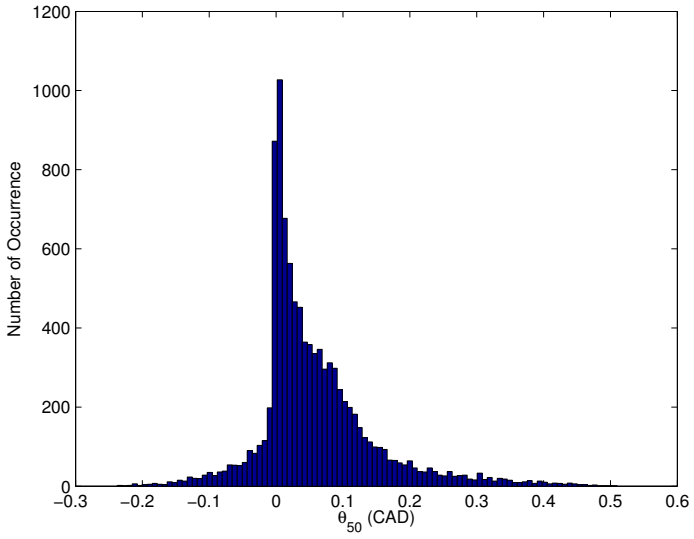

Figure 6.10: Histogram of error in θ_{50} between the LPV and NL

6.3.3 EVC and Environmental Parameter Variation Trajectories

The nonlinear model is a physics-based model which readily captures the effect of varying environmental parameters on the two states. This feature is particularly desirable if one wants to understand the robustness characteristics of HCCI, i.e. how variations in environmental parameters such as intake manifold pressure, cylinder wall temperature, etc. influence the boundedness of the model states. However, these physical links present in the nonlinear models become less obvious in the LPV model when the breathing stage is linearized about an operating point. As a platform for robustness analysis, it is desirable to recover these links in the LPV model. One intuitive method is to update the linearizations with the environmental parameters experienced by the engine in a given cycle. In other words, the elements of the gradients, $C_1 \sim C_8$, shown in Equations (6.10) and (6.11) are functions of the environmental parameters and are updated on a cycle-by-cycle basis. In this section, the EVC, intake manifold pressure, intake air temperature and cylinder wall temperature are simultaneously varied as shown in Fig. 6.11. The resulting state and output

trajectories are plotted in Fig. 6.12, Fig. 6.13 and Fig. 6.14. As can be seen, the responses of the LPV model agree well with those of the nonlinear model both in transients and in steady state. By updating the linearizations as functions of the environmental parameters, the LPV model can capture the effect of these parameters just as the physics-based nonlinear model. Similar to the observations in Section 6.3.2, the LPV model generally underestimates the temperature state in Fig. 6.13 and, consequently, overestimates θ_{50} in Fig. 6.14. Note that the responses shown here are intended to show the agreement between the two models. Further experimental studies are needed to verify these effects are quantitatively correct when compared to the testbed responses.

Since $C_1 \sim C_8$ are not generally affine functions of these environmental parameters, the useful format of system matrices being affinely dependent on varying parameters is lost. However, it should be possible to examine how a bounded change in an environmental parameter affects the ranges of C_i. For example, assuming the intake pressure is allowed to vary between a range of $\pm$ 5 kPa, and this variation further translates to a $\pm$ 0.2 change in C_2 only. Then an additional varying parameter, η_{C_2}, can be introduced and bounded to be $-0.2 \leq \eta_{C_2} \leq 0.2$. The A matrix shown in Equation (6.13) can be re-written as being affinely dependent on both the trap ratio, ζ, and η_{C_2}, i.e.,

$$A(\zeta, \eta_{C_2}) = \begin{bmatrix} 0 & \chi \cdot C_6 \\ 0 & C_2 \end{bmatrix} + \zeta \cdot \begin{bmatrix} 1 & 0 \\ 0 & 0 \end{bmatrix} + \eta_{C_2} \cdot \begin{bmatrix} 0 & 0 \\ 0 & 1 \end{bmatrix} \tag{6.15}$$

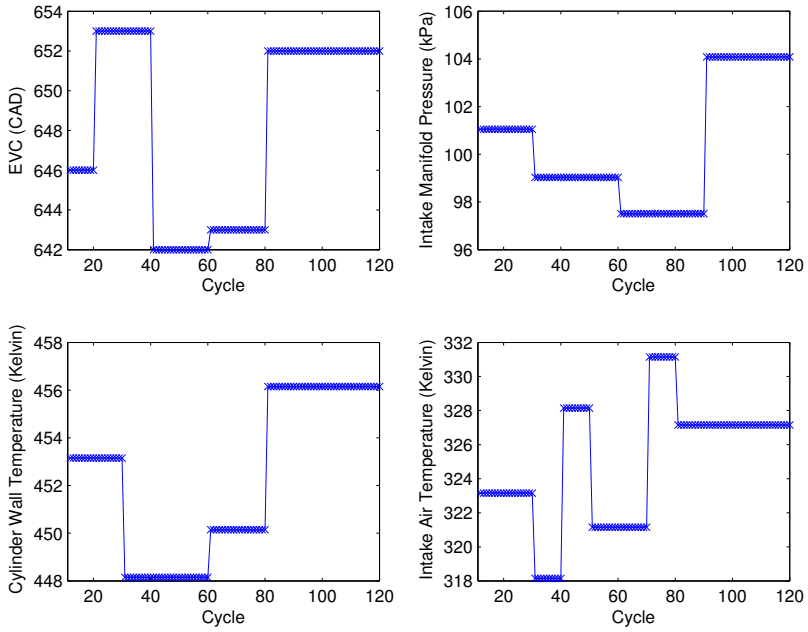

Figure 6.11: EVC and environmental parameter trajectories

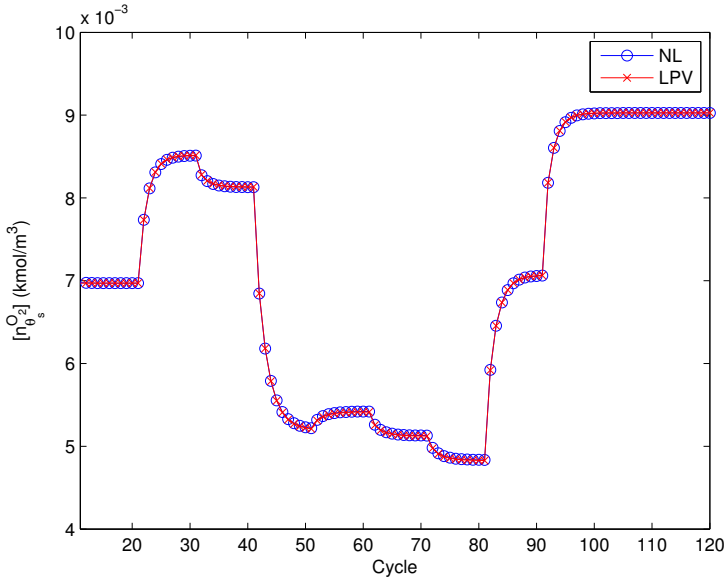

Figure 6.12: $n_{\theta_s}^{O_2}$ response: step changes in EVC and environmental parameters

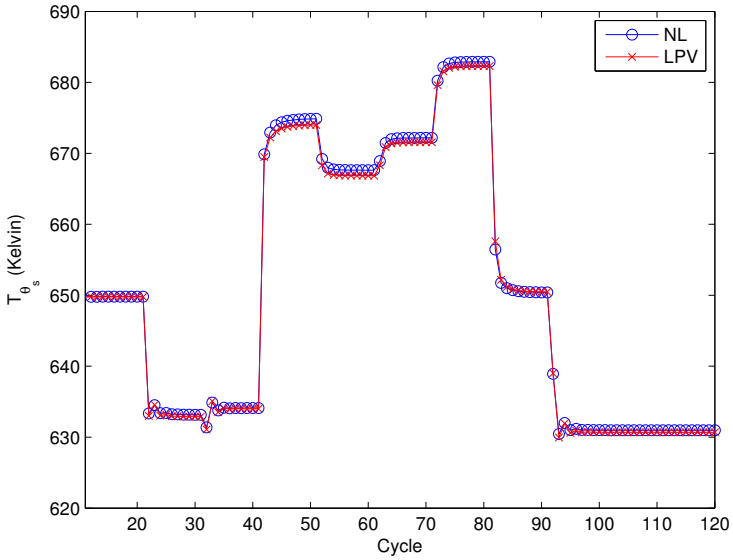

Figure 6.13: T_{θ_S} response: step changes in EVC and environmental parameters

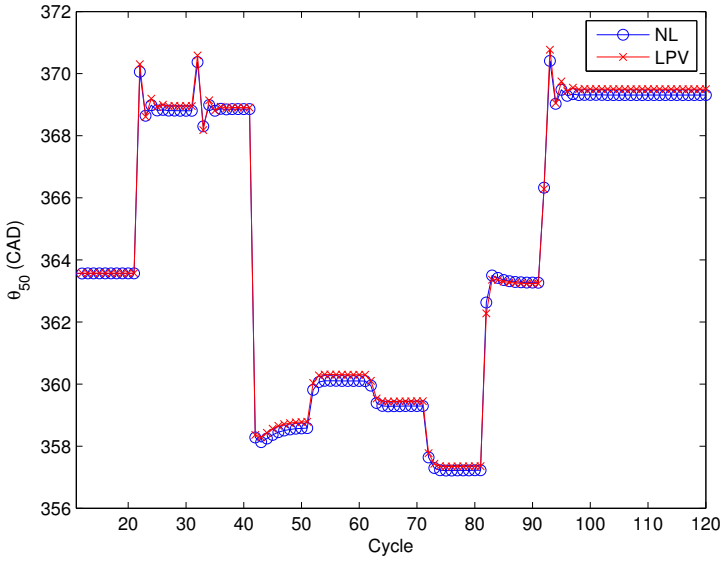

Figure 6.14: θ_{50} trajectory: step changes in EVC and environmental parameters

6.3.4 Comparison with the Testbed

In this last test, the LPV model, the nonlinear model and the engine testbed are subjected to the same randomly generated EVC trajectory. The θ_{50} responses of the two models and testbeds are plotted in Fig. 6.15. For this test, the RMS error in θ_{50} between the LPV model and the testbed is 1.390 CAD. The RMS error between the nonlinear model and the testbed is essentially the same at 1.388 CAD. The two models indeed yield very similar error when compared to the testbed. In fact, when the same EVC trajectory was tested in a different test run, the LPV model gives slightly lower RMS error at 1.356 CAD when compared to that of the nonlinear model at 1.361 CAD. To argue either the LPV model or the nonlinear model is a better approximation to the testbed is pointless, because the day-to-day variation of the testbed is far greater than the difference between the models. Therefore, it is reasonable to assume that basing the stability and robustness analysis on the LPV is, for all practical intents and purposes, equivalent to using the nonlinear model.

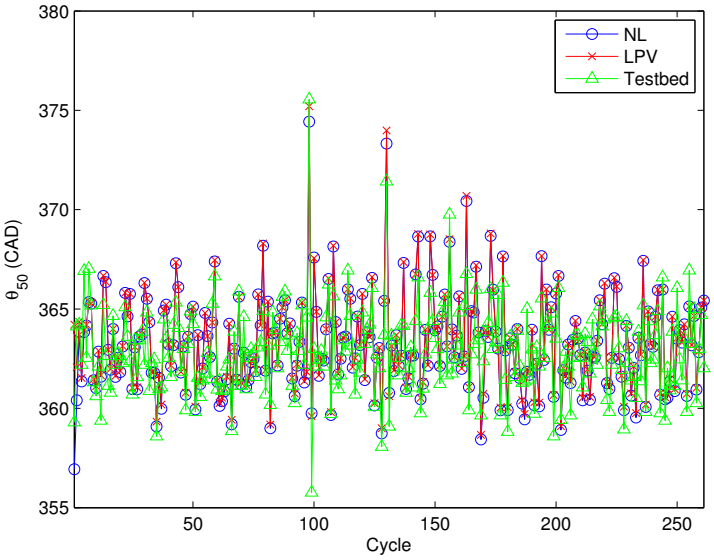

Figure 6.15: θ_{50} trajectory: LPV vs. NL vs. test bed (data set 1)

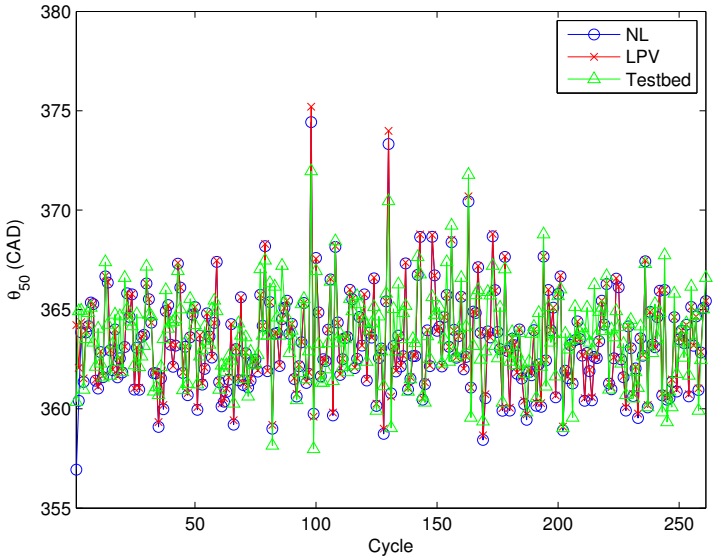

Figure 6.16: θ_{50} trajectory: LPV vs. NL vs. test bed (data set 2)

6.4 Conclusion

In this chapter, a linear parameter varying model is formulated with the explicit aim of providing a tractable platform for stability and robustness analysis. The elegant structure of the LPV model shown in Equation (6.14) is the result of understanding the dominant nonlinearity present in the nonlinear model developed by Ravi *et al.*. Roughly speaking, the nonlinearity in the temperature propagation equation exists in the combustion stage. This nonlinearity can be lumped into the exhaust temperature, T_{420}, and propagated by a linear breathing stage to the state definition point on the *next* engine cycle. A similar "linear-nonlinear" separation is shown in the oxygen content equation. The proposed LPV model is evaluated in various simulation scenarios and shows close agreement to the nonlinear model in all cases. Furthermore, the links between the environmental parameters and the system states readily available in the nonlinear model can be captured in the LPV model through updating the breathing stage linearizations as functions of these parameters. Finally, comparisons between the testbed and the two models demonstrate that the LPV and NL models can give

equivalent insights into HCCI stability and robustness. Of course, the LPV presents an elegant structure which is more amenable for stability and robustness analysis.

Chapter 7

Stability and Robustness Analysis of HCCI

In this chapter, a stability algorithm is presented to make collective statements on the boundedness of the state trajectories of the LPV model, shown below for convenience:

$$x_{k+1} = A(\zeta) \cdot x_k + B_1 \cdot u_k + B_2 \cdot T_{420,k} + d(\zeta)$$

A brief description of this algorithm's objective and the type of conclusion it makes is first given below. The mathematical background of this algorithm is presented later in the chapter. Specifically, the problem statement of this stability algorithm is as follows:

Problem statement: Stability algorithm

Given a bounded set, Φ_k. Find another bounded set, Φ_{k+1}, such that all $x_{k+1} \in \Phi_{k+1}$ for any $x_k \in \Phi_k$.

The above problem can be sovled recursively to find bounded sets for each cycle. Essentially, an initial bounded set, Φ_0, is first specified, the algorithm then finds a Φ_1 that houses all x_1, for any $x_0 \in \Phi_0$. Next, assuming x_1 can originate anywhere in Φ_1, the algorithm finds a Φ_2 that houses all x_2, and the recursion can go on indefinitely.

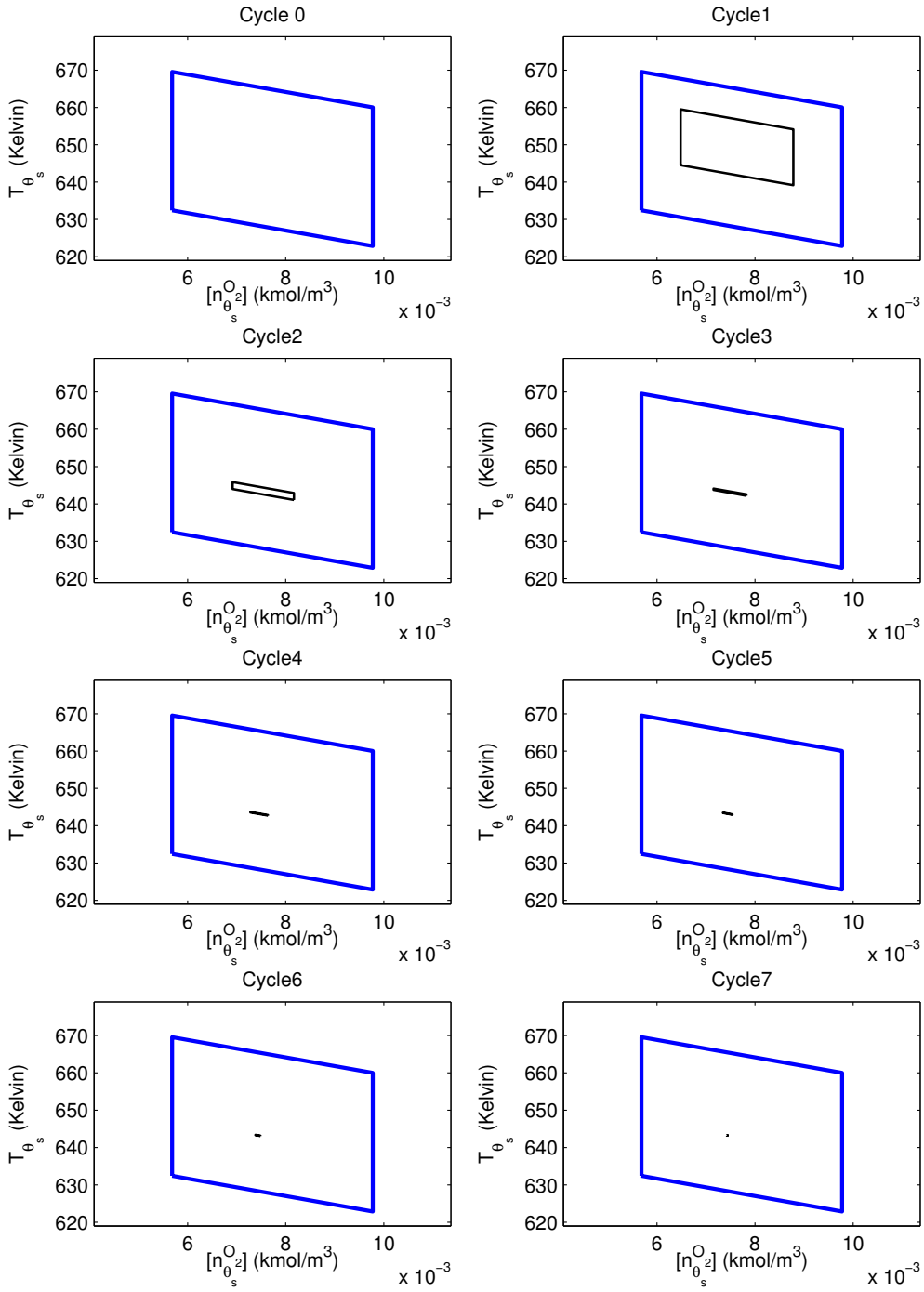

Figure 7.1: Stability analysis: bounded sets for cycle $0 \sim 7$

An example of the bounded sets generated by this algorithm with a constant EVC is shown in Fig. 7.1. In the first subplot (cycle 0), the parallelogram represents the initial bounded set, Φ_0, and is shown in every subplot in Fig. 7.1 as a reference. Each of the subplots shows another parallelogram, representing the bounded set on each cycle. As can be seen, every state trajectory originates from the initial bounded set quickly converges to the very small bounded set shown in the bottom right subplot in 7 cycles. An immediate question arises: How are the state trajectories bounded beyond cycle 7? The stability algorithm answers this question with the concept of an invariant set. Essentially, if the bounded set, Φ_{k+1}, is enclosed by the bounded set on the previous cycle, Φ_k, then Φ_{k+1} is an invariant set. This is proven later in the chapter, but an intuitive way to see this is by examining the bounded sets on two consecutive cycles as shown in Fig. 7.2. In this figure, Φ_{k+1} is a subset of Φ_k (or enclosed by Φ_k). Therefore any trajectory that enters Φ_{k+1} is in Φ_k as well. Since any trajectory that enters Φ_k is going to enter Φ_{k+1} on the next cycle, it follows that any trajectory that enters Φ_{k+1} can never leave.

This invariant-set concept is central to the stability algorithm, since it can conclude the boundedness of the state trajectories for *all* cycles by running a finite number of recursions. Every bounded set shown in Fig. 7.1 is actually enclosed by the bounded set on the previous cycle, as a result, every one of them is an invariant set. Thus, it can be concluded that the state trajectories beyond cycle 7 never leave the bounded (invariant) set shown in the last subplot, which has a very small size. Since engine operation is always perturbed by some level of disturbance, it is inconsequential to require the state trajectories converging to a single equilibrium. With a generalized definition of Lyapunov stability as presented by Ye *et al.* and Jiang *et al.* [66, 67], where stability is defined with respect to an invariant set, asymptotic stability with respect to the smallest invariant set in Fig. 7.1 can be concluded based on these sequential invariant sets. In this analysis, the varying parameter, $T_{420,k}$, is determined by the combustion temperature map, g_{comb}, which is a convex function of the states. This property is crucial in the formulation of this algorithm. Qualitatively, g_{comb} being convex means that the state trajectories originating from a polytope can be collectively and efficiently computed. The other varying parameter, the trap ratio,

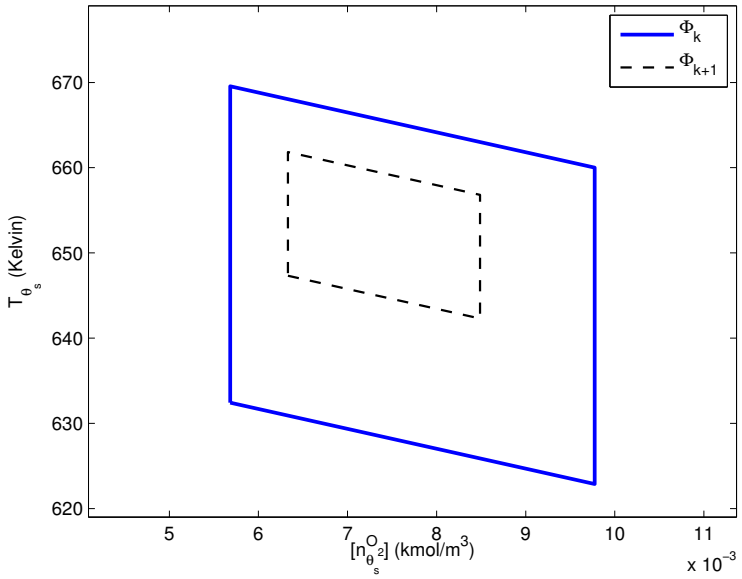

Figure 7.2: Bounded sets on two consecutive cycles

ζ, is assumed constant. This is reasonable during open-loop, steady-state operation, since ζ is predominantly influenced by EVC. Later in the chapter, ζ is allowed to vary in an interval when the stability algorithm is generalized to include model uncertainty.

To derive this recursive algorithm, some knowledge of convex sets and functions is required and it is briefly summarized in Section 7.1. In Section 7.2, the recursive stability algorithm is formulated. Using this algorithm, an additional example is presented to compare the boundedness of the state trajectories in open- and closed-loop late phasing operation. In the second half of this chapter, this algorithm is generalized to include bounded uncertainties in the system matrices A, B_1, B_2 and d, and in the combustion temperature map g_{comb}. Particularly, the effect of varying trap ratio can be discussed with this generalized robustness algorithm.

7.1 Some Definitions and Properties

The derivation of the stability algorithm requires the knowledge of the following definitions and properties of convex sets and functions. These are excerpted from the

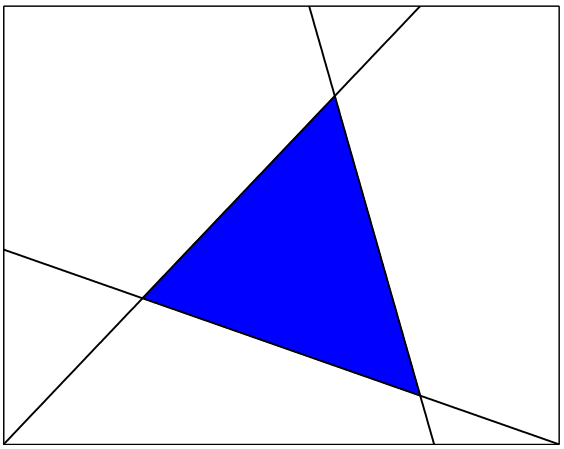

Figure 7.3: A polyhedron in R^2

convex optimization textbook by Boyd [63] and have direct relevance to this thesis. The variables shown in this section are strictly for presenting these mathematical concepts and should not be confused with variables outside this section that share the same name.

7.1.1 Convex Sets

Definition

A set, S, is convex if the line segment between any two points in S lies in S, i.e., if for any x_1 and $x_2 \in S$, and any θ with $0 \leq \theta \leq 1$:

$$\theta \cdot x_1 + (1 - \theta) \cdot x_2 \in S \tag{7.1}$$

The LHS of the above is the convex combination of the two points, x_1 and x_2, which is the line segment between these two points.

The convex sets used in this thesis are briefly described as follows.

Example 1: Hyperplane

A hyperplane is a set of points defined by a linear equality. Therefore, a hyperplane, V, is:

$$V = \left\{ x \,\middle|\, a^T \cdot x = b \right\} \tag{7.2}$$

A hyperplane is a line in R^2. In R^3, a hyperplane is actually a plane.

Example 2: Polyhedron

A polyhedron is a set of points defined by a finite number of linear equalities and inequalities. Therefore, a polyhedron, W, is:

$$W = \left\{ x \,\middle|\, {a_i}^T \cdot x \leq b_i, \quad i = 1, ..., m, \quad {c_j}^T \cdot x = d_j, \quad j = 1, ..., n \right\} \tag{7.3}$$

An example in R^2 is given in Fig. 7.3. This particular polyhedron shown is defined by three linear inequalities and is the blue shaded region in the figure. This is obviously a convex set, since the line segment between any two points in the shaded area always lies in the shaded area. When a polyhedron is further bounded, it is referred to as a polytope. In this thesis, the polyhedra presented are actually all polytopes.

Alternatively, the polyhedron (polytope) shown in Fig. 7.3 can be expressed as the set of points that are the convex combination of the three vertices, x_i^{vtx}:

$$W = \left\{ x \,\middle|\, x = \sum_i \theta_i \cdot x_i^{vtx}, \quad \sum_i \theta_i = 1, \quad \theta_i \geq 0, \quad i = 1, 2, 3 \right\} \tag{7.4}$$

7.1.2 Convex and Concave Functions

In this section, the definition and various properties of convex and concave functions are explained. As will be presented, convex and concave functions share a lot of similar properties.

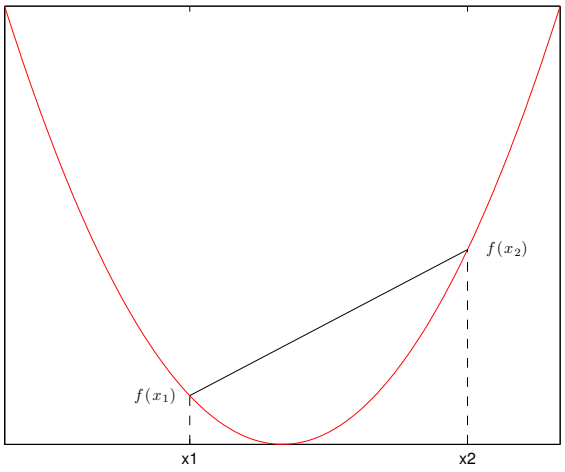

Figure 7.4: An example of a 1-D convex function

Definition

A function, f, is convex if its domain is convex and if for all x_1, $x_2 \in \mathbf{dom}f$ and θ with $0 \leq \theta \leq 1$, the following inequality holds:

$$f\left(\theta x_1 + (1-\theta)x_2\right) \leq \theta f(x_1) + (1-\theta)f(x_2) \tag{7.5}$$

Geometrically, (7.5) means that when a convex function is restricted within a line segment, the chord of the convex function is always above its graph. An example 1-D convex function is given in Fig. 7.4.

On the other hand, a function, f, is concave if $-f$ is a convex function. Therefore, a linear (or affine) function is both convex and concave.

Property 1: First-order condition

If a function, f, is differentiable (i.e., ∇f exists every point in $\mathbf{dom}f$), then f is convex if and only if

$$f\left(x\right) \geq f\left(x_1\right) + \nabla f(x_1)^T \cdot (x - x_1) \tag{7.6}$$

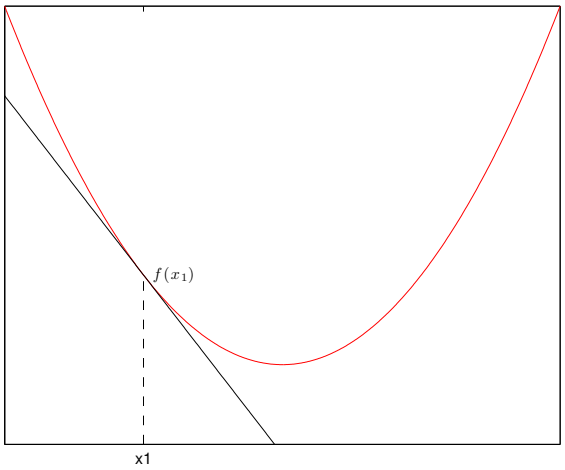

Figure 7.5: First-order condition for a differentiable 1-D convex function

Geometrically, this simply means that the linearization of a convex function is a global under-estimator of the convex function. A 1-D example of this first-order property is given in Fig. 7.5. As can be seen, the linearization shown in black is under the convex function shown in red in Fig. 7.5.

Property 2: Subgradients and convex function

If a function, $f : R^n \rightarrow R$, is convex then there exists a non-vertical supporting hyperplane to **epi**f (the epigraph of f) at every point along the graph of the function. The epigraph of f is defined as:

$$\textbf{epi}f = \left\{(x,t) \;\middle|\; x \in \textbf{dom}f,\;\; f(x) \leq t\right\} \tag{7.7}$$

This means that for all $x_i \in$ **dom** f there exists a supporting hyperplane to **epi**f defined by g_i that satisfies the following:

$$f(x) \geq f(x_i) + g_i^T \cdot (x - x_i) \tag{7.8}$$

g_i are called the subgradients of the function. Note that, if f is differentiable, then the

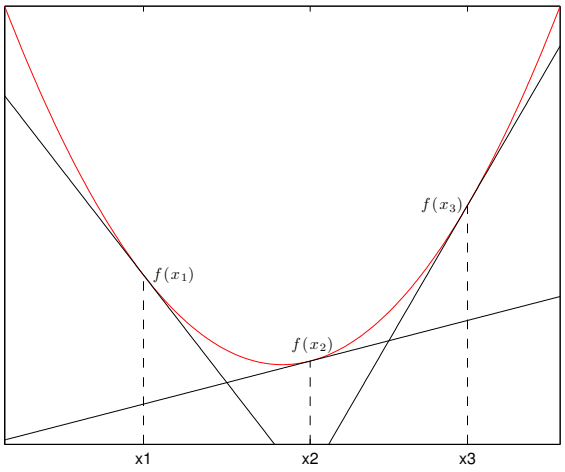

Figure 7.6: Supporting hyperplanes to the epigraph of a 1-D convex function

gradient $\nabla f(x_i) = g_i$ is a natural choice as a subgradient. Equation (7.8) is illustrated in Fig. 7.6. As can be seen, at each point on the convex function's graph, there exists a supporting hyperplane shown in black to the function's epigraph. Any of these hyperplanes is a global under-estimator of the convex function as can be interpreted in (7.8) and observed in Fig. 7.6. It is also obvious that the point-wise maximum of these hyperplanes is a global under-estimator of the convex function:

$$f(x) \geq \max_i \left\{ f(x_i) + g_i^T \cdot (x - x_i) \right\} \tag{7.9}$$

The point-wise maximum of these hyperplanes shown in Fig. 7.6 is further traced out as the solid black line in Fig. 7.7. The subgradients and the supporting hyperplanes they define are useful in examining a function's convexity when the function is only known at a number of sample points. For example, if samples from a 1-D function are given as shown in the left plot in Fig. 7.8. Then a necessary condition for the function being convex is that, at each sample point, a line can be found to lie under all other sample points as shown in the right figure in Fig. 7.8.

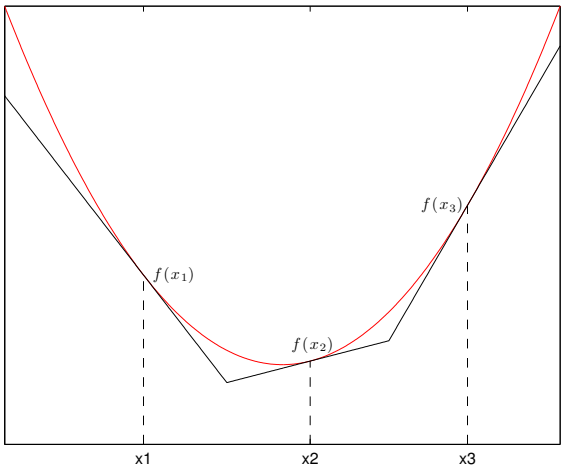

Figure 7.7: Point-wise maximum of the hyperplanes for a 1-D convex function

Property 3: Function value over a line segment

When a convex function is restricted within a line segment in its domain, then the function value cannot exceed the values at the two end points of the line segment. This property comes directly from the definition. If a convex function is restricted within a line segment defined by two end points x_1 and x_2, then according to the definition of a convex function:

$$f\left(\theta x_1 + (1-\theta)x_2\right) \leq \theta f(x_1) + (1-\theta) f(x_2) \qquad for\ \ 0 \leq \theta \leq 1$$

Furthermore, the weighted average of two values cannot exceed the higher of the two:

$$\theta f(x_1) + (1-\theta) f(x_2) \leq \max_{i=1,2} \{f(x_i)\} \qquad for\ \ 0 \leq \theta \leq 1$$

Therefore, the end result is:

$$f\left(\theta x_1 + (1-\theta)x_2\right) \leq \max_{i=1,2} \{f(x_i)\} \qquad for\ \ 0 \leq \theta \leq 1$$

A 1-D illustration of this property is shown in Fig. 7.9. This property can be further

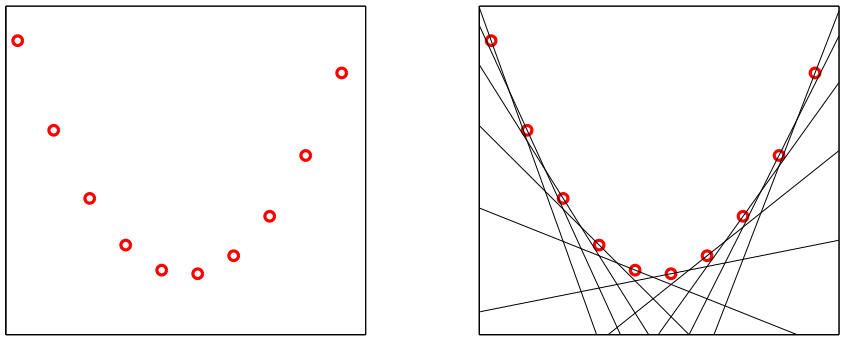

Figure 7.8: Convexity test based on function value samples

generalized to discuss the maximum function value for a convex function over a polytope. For example, f is a 2-D convex function and is restricted in its domain within the polytope shown in Fig. 7.3. It follows that the maximum function value of f over this polytope always occurs at one of the three vertices, i.e.,

$$\max_i \left\{ f(x_i^{vtx}) \right\} \geq f(x), \quad \forall x \in W, \quad i = 1, 2, 3$$

$$W = \left\{ x \;\middle|\; x = \sum_i \theta_i \cdot x_i^{vtx}, \quad \sum_i \theta_i = 1, \quad \theta_i \geq 0, \quad i = 1, 2, 3 \right\}$$

This can be proven rigorously, but a quick way to visualize is by first picking an arbitrary point in the polyhedron as shown by the red circle in Fig. 7.10. Next, draw an arbitrary line segment passing through the point and extending to the edges of the polytope as shown in the figure. Using the property of this section, the function value at the initial circle has to be lower than the value at one of the end points of the line segment, i.e., at the two red squares. It should be obvious that the function values at these two red squares will be further lower than the function values at one of the three vertices. Similarly, the minimum function value of a concave function restricted within a line segment always occurs at one of the end points. Therefore, the minimum function value of a concave function over a polytope always occurs at the vertices.

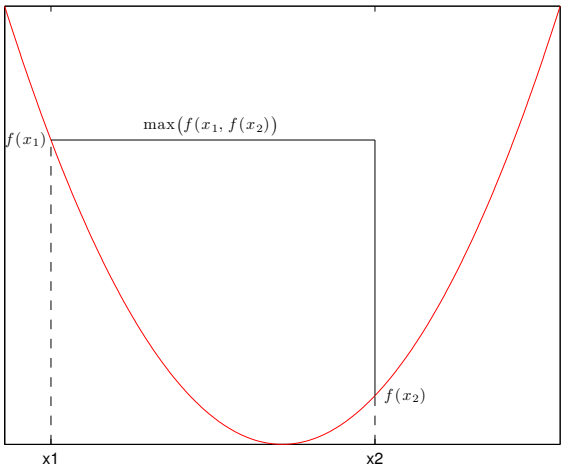

Figure 7.9: Maximum function value over a line segment

Property 4: Non-negative weighted sum of convex functions

This property comes from two facts: Non-negative scaling of a convex function yields a convex function. And the sum of convex functions yields a convex function too.

As a result, if f_i are all convex functions and w_i are non-negative scalars, then the function h is convex:

$$h = w_1 \cdot f_1 + ... + w_n \cdot f_n \tag{7.10}$$

Similarly, the non-negative weighted sum of concave functions yields a concave function as well.

7.2 The Recursive Stability Algorithm

The recursive stability algorithm used to generate Fig. 7.1 is formulated in this section. This algorithm generates collective statements about the state trajectories

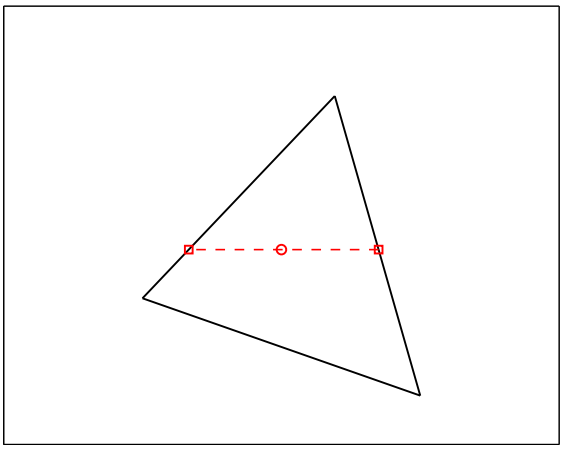

Figure 7.10: A convex function over a polyhedron

of the LPV model, which is given again in Equation (7.11) below:

$$x_{k+1} = A(\zeta) \cdot x_k + B_1 \cdot u_k + B_2 \cdot T_{420,k} + d(\zeta) \tag{7.11}$$

where

$$x = \begin{bmatrix} n_{\theta_s}^{O_2} \\ T_{\theta_s} \end{bmatrix}$$

$$u = V_{evc}$$

$$T_{420,k} = g_{comb}(x_k) \quad \textit{is the exhaust temperature}$$

$$\zeta \quad \textit{is the trap ratio}$$

In this section, the EVC command is assumed known and of fixed value. Furthermore, the trap ratio, ζ, is assumed a constant as well. As the trap ratio is dominantly influenced by the EVC command, using a constant trap ratio to discuss the stability properties under constant EVC is reasonable. The full effect of varying trap ratio on the state trajectories is discussed later in the chapter when the stability algorithm is generalized to include model uncertainties. As will be shown later, the statements on

the state trajectories made with varying trap ratio is analogous to the results with a constant ζ. Therefore, assuming a constant trap ratio here help build both physical and mathematical intuitions before introducing the more general derivation.

The other varying parameter, T_{420}, is incorporated into the stability analysis with no simplifications. The stability algorithm in the following sections relies on the property that the exhaust temperature, $T_{420,k} = g_{comb}(x_k)$, is a convex function of the states. The following subsection first examines the convexity of g_{comb}.

7.2.1 Convexity of g_{comb}

To make the stability algorithm possible, the convexity of g_{comb} needs to be established. Due to the use of the Arrhenius model, g_{comb} does not readily have an explicit form. This makes an analytical convexity proof difficult to come by. However, the values of g_{comb} can be easily simulated and sampled by a computer throughout the state space. The convexity of the function can then be examined via **Property 2** in Section 7.1.2, i.e., by finding a subgradient at each sample point such that the associated hyperplane lies under all other sample points as illustrated in Fig. 7.8. It is possible to use other ignition models instead of the Arrhenius integral in the following stability algorithm as long as it yields a convex relationship between T_{420} and the states. Later in this chapter when model uncertainties are included, this convexity requirement is further relaxed and the combustion temperature map only needs to be bounded above and below by two convex functions. As the "bowl-shaped" characteristics of g_{comb} come from the physical effect of decreased heat transfer and work output due to retarded ignition phasing, other ignition models should give similar "bowl-shaped" characteristics and satisfy this mild constraint (bounded above and below by convex functions).

To provide completeness, roughly 2500 sample points of g_{comb} were generated and forms a dense grid in the state space. Using the convex optimization software CVX, a subgradient can indeed be found for each of the 2500 sample points. In other words,

2500 q_i were found to satisfy the following:

$$T_{420}^{s,j} \geq T_{420}^{s,i} + {q_i}^T \cdot (x^{s,j} - x^{s,i}), \qquad \forall i = 1, ...n, \ \ \forall j = 1, ...n$$

where $(x^{s,i}, \ T_{420}^{s,i})$ is a sample point of the function g_{comb}, i.e.,

$$T_{420}^{s,i} = g_{comb}(x^{s,i}), \qquad i = 1, ..., n$$

7.2.2 The Nominal Firing Zone

With g_{comb} established as a convex function, the following stability algorithm is possible. The first step in this algorithm is defining a "nominal firing zone", denoted Φ_0. This is a polytope in the state space that houses *all* initial conditions of interest. Choosing the nominal firing zone as a ploytope bears mathematical significance and is shown later in this section. Essentially, all state trajectories originating from a polytope in the state space (there are *infinite* number of possible state trajectories from this polytope), can be bounded collectively by solving a *finite* number of linear programs and checking a *finite* number of corner conditions.

The particular firing zone shown in this thesis is defined with two vectors, e_1 and C:

$$e_1 = \begin{bmatrix} 1 & 0 \end{bmatrix}^T$$
$$C = \begin{bmatrix} \frac{\partial h}{\partial n_{\theta_s}^{O_2}} & \frac{\partial h}{\partial T_{\theta_s}} \end{bmatrix}^T \Big|_{n_{\theta_s}^{O_2} = n_{\theta_{s,ss}}^{O_2}, T_{\theta_s} = T_{\theta_{s,ss}}}$$

As shown above, e_1 is one of the vectors that makes up the standard basis for R^2, as commonly defined in linear algebra textbooks. Therefore, $e_1^T \cdot x$ gives the first element of the state vector, i.e., the oxygen content state. The vector C is defined similarly to the output matrix of the linearized model of the NL, since it is the gradient of the nonlinear output equation, h, of the NL model. Therefore, $C^T \cdot x$ gives the combustion timing (in a linear sense).

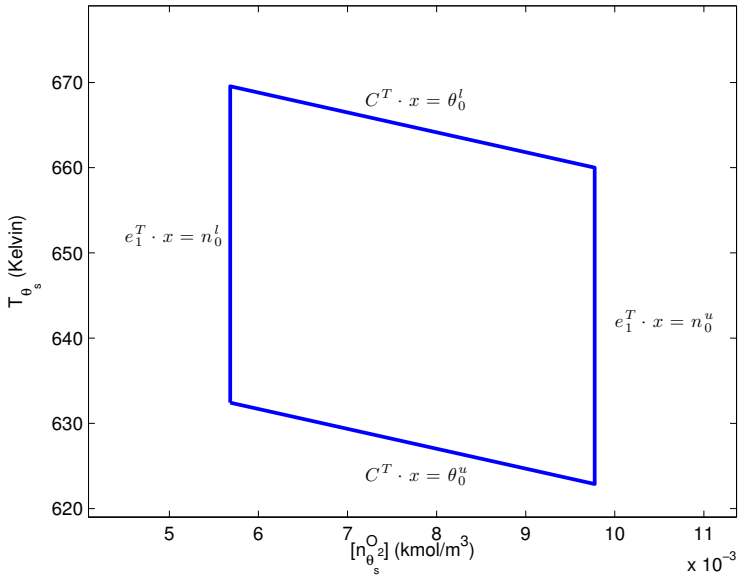

Figure 7.11: The nominal firing zone

The nominal firing zone, Φ_0, is given as follows:

$$\Phi_0 = \left\{ x \;\middle|\; {e_1}^T \cdot x \leq n_0^u, \quad {e_1}^T \cdot x \geq n_0^l, \quad C^T \cdot x \leq \theta_0^u, \quad C^T \cdot x \geq \theta_0^l \right\} \tag{7.12}$$

The first two inequalities in (7.12) constrain the in-cylinder oxygen content between a pair of upper and lower bounds, i.e., n_0^u and n_0^l. The usage of the variable n is to remind the readers that these bounds are related to the number of moles of oxygen. The last two inequalities in (7.12) translates to a pair of bounds on the combustion timing (in a linear sense). The choice of using the variable θ^u and θ^l signifies that $C^T \cdot x$ is associated with combustion timing, θ_{50}. The subscripts, 0, attached to these bounds mean that they are for the initial conditions on cycle 0.

The physical interpretation behind this nominal firing zone is apparent. The oxygen content bounds represent a range of acceptable air-fuel ratio, since too lean a mixture can lead to misfire and too rich a mixture can lead to incomplete combustion which is inefficient. In addition, the combustion timing obviously needs to be bounded above by a late phasing threshold, away from the misfire region, and bounded below

by an early phasing threshold for acceptable rate of pressure rise. This nominal firing zone is the region enclosed by the parallelogram shown in Fig. 7.11 and the four boundaries are indicated in the figure. The nominal firing zone shown in Fig. 7.11 represents a rather "wide" set of initial conditions. Specifically, this zone translates to a range of λ between 1.2 and 2.1 (as seen in the cylinder, which is higher than the λ calculated with the steady-state air and fuel flow rate), and a range of θ_{50} between 359 CAD and 380 CAD. Of course, the size of this nominal firing zone can be modified for the particular scenario to be discussed, i.e., including *all* initial conditions of interest in that particular scenario.

7.2.3 Bounded Set on the Next Cycle

With all acceptable initial conditions, x_0, inside the nominal firing zone, the objective of the stability algorithm is to find a region in the state space, which is similar in shape to Φ_0, that houses all x_1. Or, more generally, finding a bounded set Φ_{k+1} that houses all x_{k+1}, assuming x_k can originate anywhere in Φ_k. Specifically, the problem statement of this algorithm is as follows:

Problem statement: Stability algorithm

Given Φ_k, find Φ_{k+1}, such that all $x_{k+1} \in \Phi_{k+1}$ for all $x_k \in \Phi_k$, where

$$\Phi_k = \left\{ x \;\middle|\; {e_1}^T \cdot x \leq n_k^u, \quad {e_1}^T \cdot x \geq n_k^l, \quad C^T \cdot x \leq \theta_k^u, \quad C^T \cdot x \geq \theta_k^l \right\}$$

$$\Phi_{k+1} = \left\{ x \;\middle|\; {e_1}^T \cdot x \leq n_{k+1}^u, \quad {e_1}^T \cdot x \geq n_{k+1}^l, \quad C^T \cdot x \leq \theta_{k+1}^u, \quad C^T \cdot x \geq \theta_{k+1}^l \right\}$$

$$x_{k+1} = A \cdot x_k + B_1 \cdot u_k + B_2 \cdot g_{comb}(x_k) + d$$

A subtlety in the above expressions is that the A and d matrices are no longer functions of the trap ratio, since ζ is assumed constant here. The above problem translates to finding a set of bounds n_{k+1}^u, n_{k+1}^l, θ_{k+1}^u and θ_{k+1}^l that define Φ_{k+1}.

Finding n^u_{k+1} and θ^l_{k+1}

The upper bound on the oxygen content, n^u_{k+1}, and the lower bound on the combustion timing, θ^l_{k+1}, can be chosen according to **Theorem 7.1** and **Theorem 7.2**. These theorems are stated and proved as follow:

Theorem 7.1 *Suppose the four vertices of Φ_k are $x_k^{vtx,i}$, for $i = 1, ..., 4$, then n^u_{k+1} can be chosen according to Equation* (7.13).

$$n^u_{k+1} = \max_{i=1,...,4} \left\{ e_1^T A \cdot x_k^{vtx,i} + e_1^T B_1 \cdot u_k + e_1^T B_2 \cdot g_{comb}(x_k^{vtx,i}) + e_1^T d \right\} \tag{7.13}$$

Proof:

n^u_{k+1} needs to satisfy the following inequality:

$$\begin{aligned} n^u_{k+1} &\geq e_1^T \cdot x_{k+1} \\ &= e_1^T A \cdot x_k + e_1^T B_1 \cdot u_k + e_1^T B_2 \cdot g_{comb}(x_k) + e_1^T d, \quad \forall x_k \in \Phi_k \end{aligned} \tag{7.14}$$

Excluding the $e_1^T B_2 \cdot g_{comb}(x_k)$ term, the RHS of (7.14) is affine in x_k. This means that these terms combine to form a convex function of x_k (or concave, since it is affine). Furthermore, since $e_1^T B_2$ is positive and g_{comb} is convex, $e_1^T B_2 \cdot g_{comb}(x_k)$ remains a convex function of x_k. This is because the non-negative scaling of a convex function still yields a convex function. As a result, the RHS of (7.14) is the sum of convex functions, which is a convex function itself. Therefore, the maximum value of the RHS of (7.14) over Φ_k, which is a polytope, always occurs at one of the four vertices of Φ_k (**Property 3** in Section 7.1.2). This gives the following:

$$\begin{aligned} &\max_{i=1,...,4} \left\{ e_1^T A \cdot x_k^{vtx,i} + e_1^T B_1 \cdot u_k + e_1^T B_2 \cdot g_{comb}(x_k^{vtx,i}) + e_1^T d \right\} \\ &\qquad \geq e_1^T A \cdot x_k + e_1^T B_1 \cdot u_k + e_1^T B_2 \cdot g_{comb}(x_k) + e_1^T d, \qquad \forall x_k \in \Phi_k \end{aligned}$$

As a result, the following holds:

$$\begin{aligned} n_{k+1}^u &= \max_{i=1,\dots,4} \left\{ e_1^T A \cdot x_k^{vtx,i} + e_1^T B_1 \cdot u_k + e_1^T B_2 \cdot g_{comb}(x_k^{vtx,i}) + e_1^T d \right\} \\ &\geq e_1^T A \cdot x_k + e_1^T B_1 \cdot u_k + e_1^T B_2 \cdot g_{comb}(x_k) + e_1^T d, \qquad \forall x_k \in \Phi_k \\ &= e_1^T \cdot x_{k+1} \end{aligned} \tag{7.15}$$

The above shows that choosing n_{k+1}^u as stated in **Theorem 7.1** indeed gives a valid upper bound on the oxygen content on the next cycle. □

Similarly, the lower bound on combustion timing on the next cycle, θ_{k+1}^l, can be chosen according to **Theorem 7.2**.

Theorem 7.2 *Suppose the four vertices of* Φ_k *are* $x_k^{vtx,i}$*, for* $i = 1, ..., 4$*, then* θ_{k+1}^l *can be chosen according to Equation* (7.16).

$$\theta_{k+1}^l = \min_{i=1,\dots,4} \left\{ C^T A \cdot x_k^{vtx,i} + C^T B_1 \cdot u_k + C^T B_2 \cdot g_{comb}(x_k^{vtx,i}) + C^T d \right\} \tag{7.16}$$

Proof:
The proof for this theorem is similar to the previous one. The difference is that the argument here is made with concave functions instead of convex functions.
θ_{k+1}^l needs to satisfy the following inequality:

$$\begin{aligned} \theta_{k+1}^l &\leq C^T \cdot x_{k+1} \\ &= C^T A \cdot x_k + C^T B_1 \cdot u_k + C^T B_2 \cdot g_{comb}(x_k) + C^T d, \quad \forall x_k \in \Phi_k \end{aligned} \tag{7.17}$$

Excluding the $C^T B_2 \cdot g_{comb}(x_k)$ term, the RHS of (7.17) is affine in x_k. This means that these terms combine to form a concave function of x_k. Furthermore, since $C^T B_2$ is negative and g_{comb} is convex, $C^T B_2 \cdot g_{comb}(x_k)$ is a concave function of x_k. As a result, the RHS of (7.17) is the sum of concave functions, which is a concave function itself. Therefore, the minimum value of the RHS of (7.17) over Φ_k, which is a polytope,

always occurs at one of the four vertices of Φ_k. This gives the following:

$$\begin{aligned}\min_{i=1,\ldots,4} \left\{C^T A \cdot x_k^{vtx,i} + C^T B_1 \cdot u_k + C^T B_2 \cdot g_{comb}(x_k^{vtx,i}) + C^T d\right\} \\ \leq C^T A \cdot x_k + C^T B_1 \cdot u_k + C^T B_2 \cdot g_{comb}(x_k) + C^T d, \qquad \forall x_k \in \Phi_k\end{aligned}$$

As a result, the following holds:

$$\begin{aligned}\theta_{k+1}^l &= \min_{i=1,\ldots,4} \left\{C^T A \cdot x_k^{vtx,i} + C^T B_1 \cdot u_k + C^T B_2 \cdot g_{comb}(x_k^{vtx,i}) + C^T d\right\} \\ &\leq C^T A \cdot x_k + C^T B_1 \cdot u_k + C^T B_2 \cdot g_{comb}(x_k) + C^T d, \qquad \forall x_k \in \Phi_k \\ &= C^T \cdot x_{k+1} \end{aligned} \tag{7.18}$$

The above shows that choosing θ_{k+1}^l as stated in **Theorem 7.2** indeed gives a valid lower bound on the combustion timing on the next cycle. □

Finding n_{k+1}^l and θ_{k+1}^u

Two of the four bounds needed to define Φ_{k+1} are given in the previous section, the remaining two bounds, n_{k+1}^l and θ_{k+1}^u, are given here. For finding these two boundaries, **Property 2** in Section 7.1.2 is used, i.e., the fact that g_{comb} is bounded below by the hyperplanes defined by the subgradients. As pointed out, each one of these hyperplanes is a global under-estimator of the convex function as shown in Fig. 7.6. Furthermore, the point-wise maximum of a number of the hyperplanes forms a global lower bound still, as shown in Fig. 7.7. As a result, the subgradients (and the hyperplanes they defined) can be used in the following method for finding n_{k+1}^l and θ_{k+1}^u.

m hyperplanes are first chosen to form a global lower bound for g_{comb}, that is:

$$T_{420,k} = g_{comb}(x_k) \geq \max_{i=1,\ldots,m} \left\{T_{420}^{s,i} + {q_i}^T \cdot (x_k - x^{s,i})\right\} \tag{7.19}$$

where $(x^{s,i},\ T_{420}^{s,i})$ are sample points of g_{cmob}. Equation (7.19) can be written equivalently as m simultaneous inequalities:

$$T_{420,k} = g_{comb}(x_k) \geq T_{420}^{s,i} + {q_i}^T \cdot (x_k - x^{s,i}), \quad \forall i = 1, ..., m \tag{7.20}$$

n_{k+1}^l and θ_{k+1}^u can be obtained according to **Theorem 7.3** and **Theorem 7.4**.

Theorem 7.3 *Suppose J_n^* is the optimal objective of the linear program (LP) shown in* (7.21), with x_k and r_k as the optimization variables, then n_{k+1}^l can be chosen as $n_{k+1}^l = J_n^* + e_1^T B_1 \cdot u_k + e_1^T d$

$$\begin{aligned} &minimize \quad e_1^T A \cdot x_k + e_1^T B_2 \cdot r_k \\ &subject\ to: \\ &x_k \in \Phi_k \\ &r_k \geq T_{420}^{s,i} + {q_i}^T \cdot (x_k - x^{s,i}), \quad \forall i = 1, ..., m \end{aligned} \tag{7.21}$$

The full proof of this theorem is deferred until Appendix C. Note that the constraint of $x_k \in \Phi_k$ in the problem (7.21) is a set four linear inequalities. As a result, the optimization problem shown has a linear objective and $m + 4$ linear inequality constraints, which is indeed a LP. Some key points in the proof are described as follows. Suppose the LP in (7.21) is sovled with the optimizers x_k^* and r_k^* with the optimal objective J_n^*. Then the following optimality condition holds:

$$r_k^* = \max_{i=1,...,m} \left\{ T_{420}^{s,i} + {q_i}^T \cdot (x_k^* - x^{s,i}) \right\}$$

The above condition means that the r_k* always ends up exactly on the point-wise maximum of the m hyperplanes chosen to form the global lower bound for g_{comb}.

Furthermore, it can be shown that

$$\begin{aligned} J_n^* &= e_1^T A \cdot x_k^* + e_1^T B_2 \cdot \max_{i=1,\ldots,m} \left\{ T_{420}^{s,i} + {q_i}^T \cdot (x_k^* - x^{s,i}) \right\} \\ &\leq e_1^T A \cdot x_k + e_1^T B_2 \cdot \max_{i=1,\ldots,m} \left\{ T_{420}^{s,i} + {q_i}^T \cdot (x_k - x^{s,i}) \right\}, \quad \forall x_k \in \Phi_k \end{aligned}$$

With the knowledge that $e_1^T B_2 > 0$, the following can be concluded:

$$\begin{aligned} n_{k+1}^l &= e_1^T A \cdot x_k^* + e_1^T B_1 \cdot u_k + e_1^T B_2 \cdot \max_{i=1,\ldots,m} \left\{ T_{420}^{s,i} + {q_i}^T \cdot (x_k^* - x^{s,i}) \right\} + e_1^T d \\ &\leq e_1^T A \cdot x_k + e_1^T B_1 \cdot u_k + e_1^T B_2 \cdot \max_{i=1,\ldots,m} \left\{ T_{420}^{s,i} + {q_i}^T \cdot (x_k - x^{s,i}) \right\} + e_1^T d, \quad \forall x_k \in \Phi_k \\ &\leq e_1^T A \cdot x_k + e_1^T B_1 \cdot u_0 + e_1^T B_2 \cdot g_{comb}(x_k) + e_1^T d, \quad \forall x_k \in \Phi_k \\ &= e_1^T \cdot x_{k+1} \end{aligned}$$

As shown above, n_{k+1}^l is indeed a lower bound on oxygen content on the next cycle.

The upper bound on combustion timing, θ_{k+1}^u, can be found in a similar manner according to **Theorem 7.4**.

Theorem 7.4 *Suppose J_θ^* is the optimal objective of the linear program (LP) shown in* (7.22), with x_k and r_k as the optimization variables, then θ_{k+1}^u can be chosen as $\theta_{k+1}^u = J_\theta^* + C^T B_1 \cdot u_k + C^T d$

$$\begin{aligned} &\textit{maximize} \quad C^T A \cdot x_k + C^T B_2 \cdot r_k \\ &\textit{subject to}: \\ &x_k \in \Phi_k \\ &r_k \geq T_{420}^{s,i} + {q_i}^T \cdot (x_k - x^{s,i}), \quad \forall i = 1, ..., m \end{aligned} \tag{7.22}$$

With the knowledge of $C^T B_2 < 0$, the proof for **Theorem 7.4** is similar to the one for **Theorem 7.3** shown in Appendix C. The above two LPs along with the method for obtaining n_{k+1}^u and θ_{k+1}^l give the four bounds required to define Φ_{k+1}, the bounded set where all x_{k+1} reside in.

7.2.4 A Recursive Scheme

Given the nominal firing zone shown in Section 7.2.2, the above approach can be used recursively to generate the sequence of bounded sets shown in Fig. 7.1. In general, assuming all x_k reside in Φ_k, then Φ_{k+1} can be ascertained by checking the vertices of Φ_k and solving two LPs. Note that the particular EVC command used in Fig. 7.1 results in the state trajectories converging to the small bounded set near the bottom of the bowl in the combustion temperature map in Fig. 6.1, i.e., the "sweet spot" region described in Chapter 4.

7.2.5 Invariant Sets

As explained in the opening section of this chapter, invariant sets are central in this recursive algorithm to show the boundedness of the state trajectories for *all* cycles. Specifically, if the bounded set Φ_{k+1} is a subset of Φ_k (enclosed by Φ_k), then Φ_{k+1} is an invariant set. This is stated in **Theorem 7.5** and proved below.

Theorem 7.5 *If $\Phi_{k+1} \subseteq \Phi_k$, and for any $x_k \in \Phi_k$ implies $x_{k+1} \in \Phi_{k+1}$, then Φ_{k+1} is an invariant set.*

Proof:

It is obvious that any $x_{k+1} \in \Phi_{k+1}$ also satisfy $x_{k+1} \in \Phi_k$, since Φ_{k+1} is a subset of Φ_k. Furthermore, any $x_{k+1} \in \Phi_k$ implies $x_{k+2} \in \Phi_{k+1}$, this is guaranteed by the problem statement of the stability algorithm. The same argument can be used on all subsequent cycles and show that $x_i \in \Phi_{k+1}$ for all $i \geq k+1$, i.e., Φ_{k+1} is an invariant set.□

To summarize, the recursive stability algorithm operates in the following manner:

- Define a nominal firing zone Φ_0.
- Proceed to find the bounded sets Φ_k recursively by solving two LPs and checking the vertices of Φ_{k-1} in each recursion. (Based on **Theorem 7.1, 7.2, 7.3 and 7.4**)

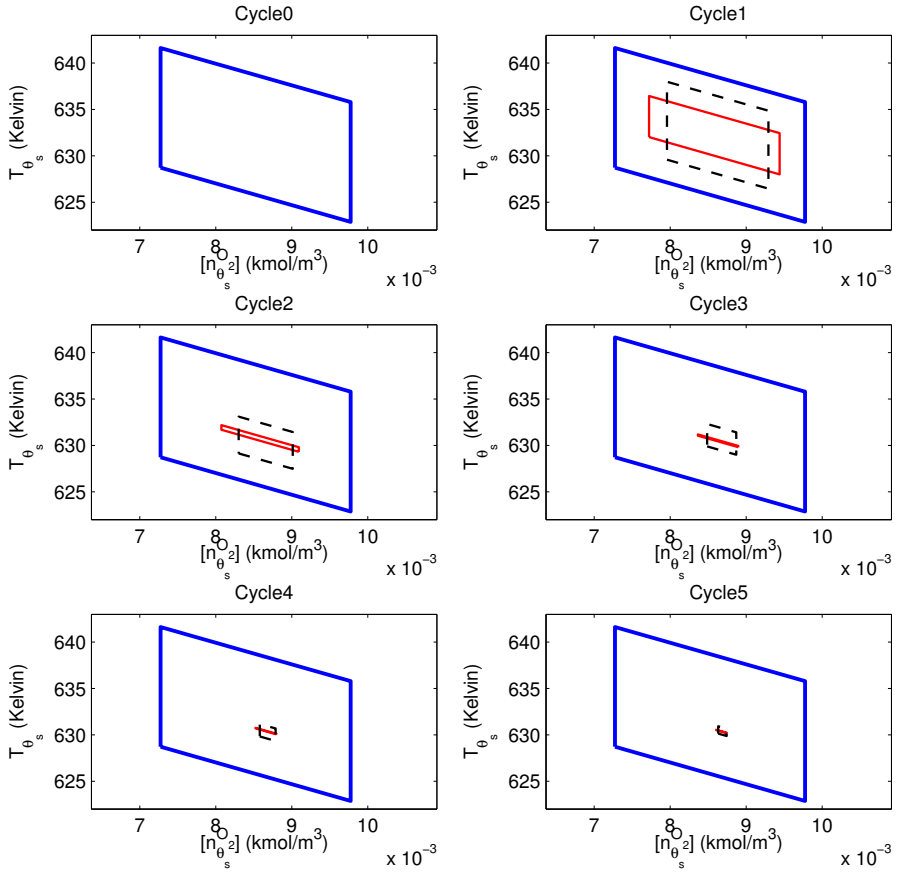

Figure 7.12: Stability analysis (fixed trap ratio): open- and closed-loop comparison around a late-phasing point: black dashed-(open loop), red solid-(closed loop)

- If there exists a Φ_k that is completely enclosed by Φ_{k-1}, then Φ_k is a proven invariant set. This means that all initial conditions inside Φ_0 converges within Φ_k at precisely cycle k and stays there for *all* subsequent cycles.

- If the size of the invariant set is satisfactorily small, the recursion can be terminated. If not, continue the recursion in search of smaller invariant sets.

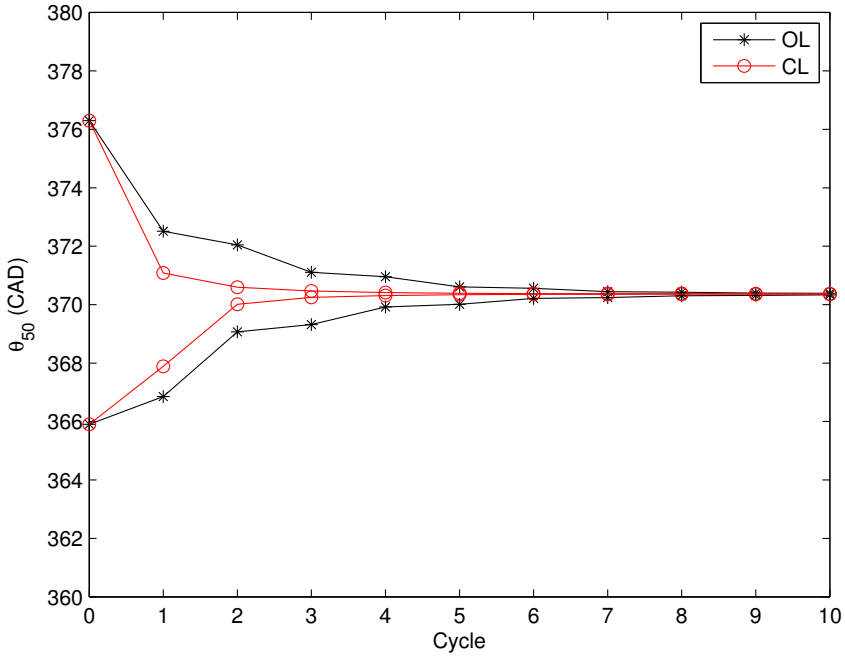

Figure 7.13: θ_{50} bounds (fixed trap ratio): open- and closed-loop comparison around a late-phasing point.

7.2.6 Stability Analysis: OL vs. CL Late-Phasing Operation

The late-phasing local controller shown in Chapter 5 is able to regulate the oscillatory combustion timing response around a late phasing operating point. Note that this feedback controller is based on the quadratic cost shown in Equation (5.2), with an aggressive tuning to regulate combustion timing ($Q \gg R$). In this example, the open- and closed-loop system response is examined with the recursive stability algorithm. The two cases start from the same nominal firing zone shown in blue in the first subplot in Fig. 7.12, and the resulting bounded sets are shown with the black dashed line representing the open-loop case, and the red solid line representing the closed-loop case. As can be seen, the feedback controller generally shrinks the bounded sets in the "combustion timing" direction much more aggressively than the open-loop case. However, the controller is allowing a slower convergence of oxygen content to make the fast combustion timing convergence possible. The nonlinear model output equation,

$\theta_{50} = h(x)$, can be further evaluated over the bounded sets shown in Fig. 7.12 to generate θ_{50} bounds on each cycle for the two cases. These bounds are shown in Fig. 7.13. Corroborating the previous insight, the feedback controller is indeed shrinking the combustion timing bounds much more quickly than the open loop case. These observations match well to the way that the weights are tuned in the quadratic cost function (5.2). It should be noted that the LQR controller is only aware of the local linearized dynamics, but it is shown to improve the combustion timing response even when it is paired with the more complicated LPV model (which is almost equivalent to the nonlinear model).

In this analysis, the trap ratio, ζ, is assumed a constant, which does not capture the full detail of the two scenarios. Particularly, the EVC is actually changing in the closed-loop scenario due to the feedback control law. In the next section, the recursive algorithm is generalized to include model uncertainty and is able to take the varying trap ratio into account.

7.3 Generalization: Robustness Analysis

In this section, the recursive stability algorithm is modified to accommodate model uncertainties and generalized as a robustness analysis. Recall that the LPV model has the following format:

$$x_{k+1} = A(\zeta) \cdot x_k + B_1 \cdot u_k + B_2 \cdot g_{comb}(x_k) + d(\zeta)$$

In this section, the model uncertainties can exist in the system matrices, or in the combustion temperature map, g_{comb}, as described below.

7.3.1 Uncertainties in the System Matrices

The immediate need to allow model uncertainties in the system matrices is to account for the effect of varying trap ratio, ζ. In this generalization, the trap ratio is allowed to vary in an interval, $\zeta \in [\zeta^1 \ \ \zeta^2]$. Note that any ζ in this interval can be expressed

as the convex combination of the two extremes:

$$\zeta = \sum_{i=1}^{2} \theta_i \cdot \zeta^i, \quad \sum_{i=1}^{2} \theta_i = 1, \quad \theta_i \geq 0, \quad i = 1, 2$$

As shown in Equation (6.13) in Chapter 6, the A and d matrix of the LPV model are affinely dependent on the trap ratio. Therefore, $A(\zeta)$ for any $\zeta \in [\zeta^1 \ \zeta^2]$ can be expressed as follows:

$$\begin{aligned} A(\zeta) &= A\big(\sum_{i=1}^{2} \theta_i \cdot \zeta^i\big), \quad \sum_{i=1}^{2} \theta_i = 1, \quad \theta_i \geq 0, \quad i = 1, 2 \\ &= \sum_{i=1}^{2} \theta_i \cdot A\big(\zeta^i\big), \quad \sum_{i=1}^{2} \theta_i = 1, \quad \theta_i \geq 0, \quad i = 1, 2 \end{aligned} \tag{7.23}$$

The above means that any allowable $A(\zeta)$ can be expressed as the convex combination of the two A matrices evaluated at the two extremes of ζ. Similarly, any allowable $d(\zeta)$ can be expressed as follows:

$$d(\zeta) = \sum_{i=1}^{2} \theta_i \cdot d\big(\zeta^i\big), \quad \sum_{i=1}^{2} \theta_i = 1, \quad \theta_i \geq 0, \quad i = 1, 2 \tag{7.24}$$

Note that there are infinite number of $A(\zeta)$ and $d(\zeta)$ in the allowable range of ζ. It will be shown later that the state trajectories propagated by these infinite number of system matrices can be bounded by checking the system behavior at the two extremes of ζ.

It is further possible to include varying parameters other than the trap ratio in the formulation, as long as the system matrices A, B_1, B_2 and d are affinely dependent on these additional varying parameters. For example, the A matrix can be affinely

dependent on a vector of p varying parameters, $\eta = \begin{bmatrix} \eta_1 & ... & \eta_p \end{bmatrix}^T$:

$$\begin{aligned} A(\eta) &= A_0 + \eta_1 \cdot A_1 + \eta_2 \cdot A_2 + ... + \eta_p \cdot A_p \\ \eta_i &\leq \eta_i^{max}, \quad \forall i = 1, ..., p \\ \eta_i &\geq \eta_i^{min}, \quad \forall i = 1, ..., p \end{aligned} \tag{7.25}$$

The derivation in the following sections can be easily modified to accommodate the case with additional varying parameters shown in (7.25). As a result, the proposed method to include the uncertain environmental parameters shown in Equation (6.15) in Section 6.3.3 fits into this framework.

7.3.2 Uncertainties in the Combustion Temperature Map

Previously, the exhaust temperature is assumed to be a convex function of the states in the recursive stability algorithm, i.e.,

$$\begin{aligned} T_{420,k} &= g_{comb}(x_k) \\ g_{comb} &\ is\ convex \end{aligned}$$

In reality, there are a number of things that can influence g_{comb}. To name a couple, uncertain fuel quality and heat transfer characteristics can influence the amount of effective energy addition to the in-cylinder gas, which in turn affects the exhaust temperature T_{420}. Therefore, it is natural to allow perturbations in the nominal combustion temperature map g_{comb}. In the robustness analysis, $T_{420,k}$ is not known exactly besides being bounded above and below by two convex functions:

$$\begin{aligned} g_{comb}^l(x_k) \leq T_{420,k} &\leq g_{comb}^u(x_k) \\ g_{comb}^l &\ and\ g_{comb}^u\ are\ both\ convex \end{aligned} \tag{7.26}$$

Qualitatively, this requirement enforces the combustion temperature to maintain its general "bowl shape".

7.3.3 Robustness Analysis: Bounded Set on the Next Cycle

Just as the stability algorithm, the robustness analysis starts from a nominal firing zone, Φ_0, and proceeds to find the bounded set for each cycle. The difference is that the system matrices are affinely dependent on the trap ratio in a bounded range, and the exhaust temperature map is not known exactly except being bounded above and below by convex functions. The problem statement of this robustness algorithm is given as follows:

Problem statement: Robustness algorithm

Given Φ_k, find Φ_{k+1}, such that all $x_{k+1} \in \Phi_{k+1}$ for all $x_k \in \Phi_k$, where

$$\begin{aligned}
\Phi_k &= \left\{ x \;\middle|\; {e_1}^T \cdot x \le n_k^u, \quad {e_1}^T \cdot x \ge n_k^l, \quad C^T \cdot x \le \theta_k^u, \quad C^T \cdot x \ge \theta_k^l \right\} \\
\Phi_{k+1} &= \left\{ x \;\middle|\; {e_1}^T \cdot x \le n_{k+1}^u, \quad {e_1}^T \cdot x \ge n_{k+1}^l, \quad C^T \cdot x \le \theta_{k+1}^u, \quad C^T \cdot x \ge \theta_{k+1}^l \right\} \\
x_{k+1} &= A(\zeta) \cdot x_k + B_1 \cdot u_k + B_2 \cdot T_{420,k} + d(\zeta) \\
\zeta^1 &\le \zeta \le \zeta^2, \quad g_{comb}^l(x_k) \le T_{420,k} \le g_{comb}^u(x_k)
\end{aligned}$$

This again translates to finding a set of bounds n_{k+1}^u, n_{k+1}^l, θ_{k+1}^u and θ_{k+1}^l that define Φ_{k+1}.

Finding n_{k+1}^u and θ_{k+1}^l

The upper bound on the oxygen content, n_{k+1}^u, and the lower bound on the combustion timing, θ_{k+1}^l, can be chosen according to **Theorem 7.6** and **Theorem 7.7**. These theorems are stated and proved as follow:

Theorem 7.6 *Suppose the four vertices of Φ_k are $x_k^{vtx,i}$, for $i = 1, ..., 4$, then n_{k+1}^u can be chosen according to Equation* (7.27).

$$n_{k+1}^u = \max_{j=1,2} \left\{ \max_{i=1,...,4} \left\{ e_1^T A(\zeta^j) \cdot x_k^{vtx,i} + e_1^T B_1 \cdot u_k + e_1^T B_2 \cdot g_{comb}^u(x_k^{vtx,i}) + e_1^T d(\zeta^j) \right\} \right\} \tag{7.27}$$

Proof:

n^u_{k+1} needs to satisfy the following inequality for any $\zeta \in [\zeta^1 \ \ \zeta^2]$ and any $x_k \in \Phi_k$:

$$\begin{aligned} n^u_{k+1} &\geq e_1^T \cdot x_{k+1} \\ &= e_1^T A(\zeta) \cdot x_k + e_1^T B_1 \cdot u_k + e_1^T B_2 \cdot T_{420,k} + e_1^T d(\zeta) \end{aligned} \tag{7.28}$$

Since $e_1^T B_2 > 0$ and T_{420} is bounded above by g^u_{comb}, the last line of Equation (7.28) can be bounded above as follows:

$$\begin{aligned} &e_1^T A(\zeta) \cdot x_k + e_1^T B_1 \cdot u_k + e_1^T B_2 \cdot g^u_{comb}(x_k) + e_1^T d(\zeta) \\ &\qquad \geq e_1^T A(\zeta) \cdot x_k + e_1^T B_1 \cdot u_k + e_1^T B_2 \cdot T_{420,k} + e_1^T d(\zeta) \end{aligned} \tag{7.29}$$

Therefore, if n^u_{k+1} is chosen to be greater than the LHS of (7.29) for any $\zeta \in [\zeta^1 \ \ \zeta^2]$ and any $x_k \in \Phi_k$, then it satisfies (7.28). Recalling the relationship shown in Equation (7.23) and (7.24), the LHS of (7.29) can be further expressed as follows, for some θ that satisfies $\sum_{j=1}^2 \theta_j = 1$ and $\theta_j \geq 0, \ \ j = 1, 2$:

$$\begin{aligned} &e_1^T A(\zeta) \cdot x_k + e_1^T B_1 \cdot u_k + e_1^T B_2 \cdot g^u_{comb}(x_k) + e_1^T d(\zeta) \\ &\quad = e_1^T \sum_{j=1}^{2} \theta_j \cdot A(\zeta^j) \cdot x_k + e_1^T B_1 \cdot u_k + e_1^T B_2 \cdot g^u_{comb}(x_k) + e_1^T \sum_{j=1}^{2} \theta_j \cdot d(\zeta^j) \\ &\quad = \sum_{j=1}^{2} \theta_j \cdot \left[e_1^T A(\zeta^j) \cdot x_k + e_1^T B_1 \cdot u_k + e_1^T B_2 \cdot g^u_{comb}(x_k) + e_1^T d(\zeta^j) \right] \end{aligned} \tag{7.30}$$

For any $j = 1, 2$ and $x_k \in \Phi_k$, the maximum of the term inside the brackets in the last line of (7.30) always occurs at one of the vertices, $x_k^{vtx,i}$, of Φ_k. This is because $e_1^T B_2 > 0$ and g^u_{comb} is a convex function of x_k. As a result, the term inside the brackets in the last line of (7.30) is convex in x_k for any $j = 1, 2$. Thus, the following inequality holds for any $j = 1, 2$ and $x_k \in \Phi_k$:

$$\begin{aligned} &\max_{i=1,\ldots 4} \left\{ e_1^T A(\zeta^j) \cdot x_k^{vtx,i} + e_1^T B_1 \cdot u_k + e_1^T B_2 \cdot g^u_{comb}(x_k^{vtx,i}) + e_1^T d(\zeta^j) \right\} \\ &\qquad \geq e_1^T A(\zeta^j) \cdot x_k + e_1^T B_1 \cdot u_k + e_1^T B_2 \cdot g^u_{comb}(x_k) + e_1^T d(\zeta^j) \end{aligned} \tag{7.31}$$

The LHS of (7.31) can be further bounded above for any $j = 1, 2,$:

$$\max_{j=1,2}\left\{\max_{i=1,\ldots,4}\left\{e_1^T A(\zeta^j)\cdot x_0^{vtx,i} + e_1^T B_1\cdot u_0 + e_1^T B_2\cdot g_{comb}^u(x_0^{vtx,i}) + e_1^T d(\zeta^j)\right\}\right\}$$
$$\geq \max_{i=1,\ldots 4}\left\{e_1^T A(\zeta^j)\cdot x_k^{vtx,i} + e_1^T B_1\cdot u_k + e_1^T B_2\cdot g_{comb}^u(x_k^{vtx,i}) + e_1^T d(\zeta^j)\right\} \quad (7.32)$$

Choosing n_{k+1}^u as the LHS of (7.32), and combining all of the above results, the following holds for any $\zeta^1 \leq \zeta \leq \zeta^2$, $x_k \in \Phi_k$, and some θ that satisfies $\sum_{j=1}^2 \theta_j = 1$ and $\theta_j \geq 0,\ \ j = 1, 2$:

$$\begin{aligned}
e_1^T\cdot x_{k+1} &= e_1^T A(\zeta)\cdot x_k + e_1^T B_1\cdot u_k + e_1^T B_2\cdot T_{420,k} + e_1^T d(\zeta)\\
&\leq e_1^T A(\zeta)\cdot x_k + e_1^T B_1\cdot u_k + e_1^T B_2\cdot g_{comb}^u(x_k) + e_1^T d(\zeta)\\
&= \sum_{j=1}^2 \theta_j\cdot\left[e_1^T A(\zeta^j)\cdot x_k + e_1^T B_1\cdot u_k + e_1^T B_2\cdot g_{comb}^u(x_k) + e_1^T d(\zeta^j)\right]\\
&\leq \sum_{j=1}^2 \theta_j\cdot\left[\max_{i=1,\ldots 4}\left\{e_1^T A(\zeta^j)\cdot x_k^{vtx,i} + e_1^T B_1\cdot u_k + e_1^T B_2\cdot g_{comb}^u(x_k^{vtx,i}) + e_1^T d(\zeta^j)\right\}\right]\\
&\leq \sum_{j=1}^2 \theta_j\cdot\max_{j=1,2}\left\{\max_{i=1,\ldots 4}\left\{e_1^T A(\zeta^j)\cdot x_k^{vtx,i} + e_1^T B_1\cdot u_k + e_1^T B_2\cdot g_{comb}^u(x_k^{vtx,i}) + e_1^T d(\zeta^j)\right\}\right\}\\
&= \max_{j=1,2}\left\{\max_{i=1,\ldots 4}\left\{e_1^T A(\zeta^j)\cdot x_k^{vtx,i} + e_1^T B_1\cdot u_k + e_1^T B_2\cdot g_{comb}^u(x_k^{vtx,i}) + e_1^T d(\zeta^j)\right\}\right\}\\
&= n_{k+1}^u
\end{aligned}$$

which shows choosing n_{k+1}^u according to **Theorem 7.6** indeed gives a valid upper bound on the oxygen content on the next cycle.□

Similarly, the lower bound on combustion timing, θ_{k+1}^l, can be chosen according to **Theorem 7.7**, which is shown below.

Theorem 7.7 *Suppose the four vertices of* Φ_k *are* $x_k^{vtx,i}$*, for* $i = 1, ..., 4$*, then* θ_{k+1}^l

can be chosen according to Equation (7.33).

$$\theta_{k+1}^{l} = \min_{j=1,2} \left\{ \min_{i=1,...,4} \left\{ C^T A(\zeta^j) \cdot x_k^{vtx,i} + C^T B_1 \cdot u_k + C^T B_2 \cdot g_{comb}^{u}(x_k^{vtx,i}) + C^T d(\zeta^j) \right\} \right\} \tag{7.33}$$

The proof is neglected since it is very similar to the one presented for **Theorem 7.6**.

Finding n_{k+1}^{l} and θ_{k+1}^{u}

For finding these two boundaries, the concept of bounding $T_{420,k}$ below by hyperplanes in the stability algorithm is reused. The only difference is that these hyperplanes first form a global lower bound for g_{comb}^{l}, which, in turn, is a global lower bound for T_{420}.

Specifically, m hyperplanes defined by the subgradients, q_i, are chosen at the m sample points, $x^{s,i}$, of g_{comb}^{l}. Next, the point-wise maximum of these hyperplanes forms a global lower bound on the $T_{420,k}$:

$$\begin{aligned} T_{420,k} &\geq g_{comb}^{l}(x_k) \\ &\geq g_{comb}^{l}(x_k^{s,i}) + {q_i}^T \cdot (x_k - x^{s,i}), \quad \forall i = 1, ..., m \end{aligned} \tag{7.34}$$

Note that these q_i always exist, because g_{comb}^{l} is a convex function as specified in the problem formulation. With these hyperplanes, n_{k+1}^{l} and θ_{k+1}^{u} can be found according to **Theorem 7.8** and **Theorem 7.9** as shown below.

Theorem 7.8 *Suppose, for each $j = 1, 2$, $J_{n,j}^{*}$ are the optimal objectives of the LPs shown in* (7.35), with x_k and r_k as the optimization variables, then n_{k+1}^{l} can be chosen according to Equation (7.36).

$$\begin{aligned} &\textit{minimize} \quad e_1^T A(\zeta^j) \cdot x_k + e_1^T B_2 \cdot r_k \\ &\textit{subject to}: \\ &x_k \in \Phi_k \\ &r_k \geq g_{comb}^{l}(x_k^{s,i}) + {q_i}^T \cdot (x_k - x^{s,i}), \quad \forall i = 1, ..., m \end{aligned} \tag{7.35}$$

$$n_{k+1}^{l} = \min_{j=1,2} \left\{ J_{n,j}^{*} + e_1^T B_1 \cdot u_k + e_1^T d(\zeta^j) \right\} \tag{7.36}$$

The above theorem (**Theorem 7.8**) can be proved by combining the results shown in the proof for **Theorem 7.3** and **Theorem 7.6**. Essentially, for each $j = 1, 2$, the term in the curly brackets shown in Equation (7.36) is the minimum oxygen content on the next cycle, assuming the system matrices $A(\zeta)$ and $d(\zeta)$ are evaluated at the two extremes of ζ. This can be shown with a derivation similar to the proof for **Theorem 7.3** (shown in Appendix C). It follows that the lower of the two minimum values with ζ at the two extremes is a common lower bound for any ζ in $[\zeta^1 \ \ \zeta^2]$. This can shown by using an argument analogous to the proof for **Theorem 7.6**.

Similarly, **Theorem 7.9** can be used to find θ_{k+1}^{u}:

Theorem 7.9 *Suppose, for each* $j = 1, 2$, $J_{\theta,j}^{*}$ *are the optimal objectives of the LPs shown in* (7.37), with x_k and r_k as the optimization variables, then θ_{k+1}^{u} can be chosen according to Equation (7.38).

$$\begin{aligned} &maximize \quad C^T A(\zeta^j) \cdot x_k + C^T B_2 \cdot r_k \\ &subject\ to: \\ &x_k \in \Phi_k \\ &r_k \geq g_{comb}^{l}(x_k^{s,i}) + {q_i}^T \cdot (x_k - x^{s,i}), \quad \forall i = 1, ..., m \end{aligned} \tag{7.37}$$

$$\theta_{k+1}^{u} = \max_{j=1,2} \left\{ J_{\theta,j}^{*} + C^T B_1 \cdot u_k + C^T d(\zeta^j) \right\} \tag{7.38}$$

Combining **Theorem 7.6**, **7.7**, **7.8** and **7.9** completely specifies the bounded set Φ_{k+1}. As can be seen, finding Φ_{k+1} for the varying trap ratio case requires checking twice as many vertices and solving twice as many LPs compared to the stability algorithm with a constant ζ. More generally, the size of the problem doubles every

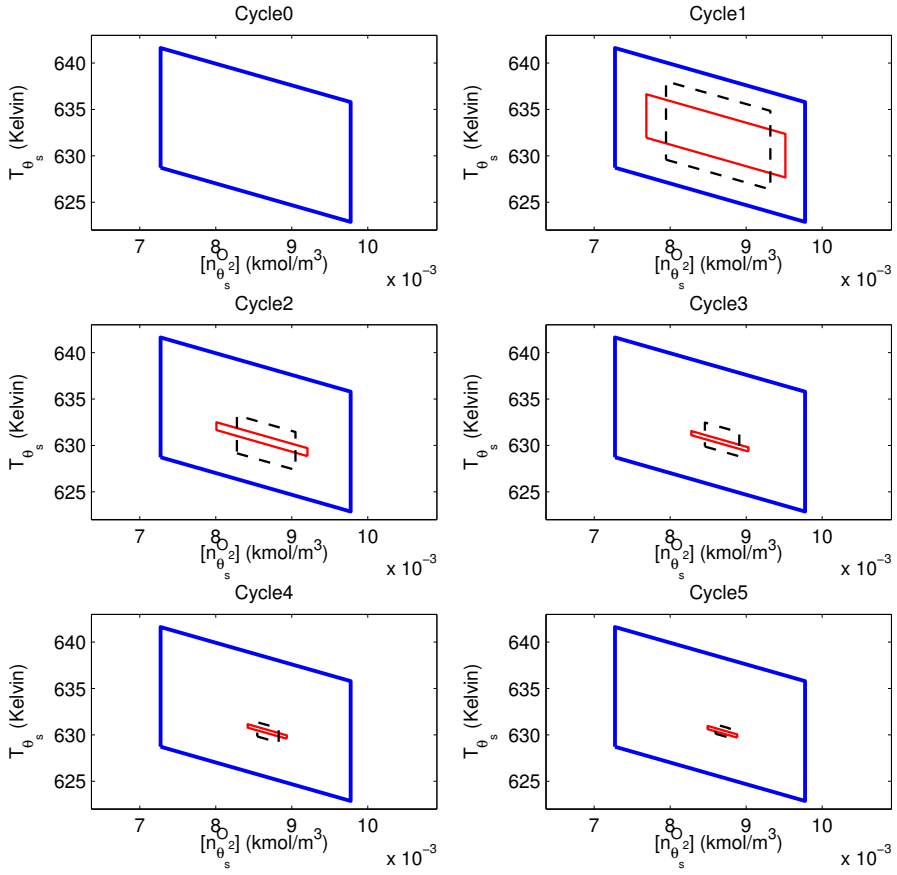

Figure 7.14: Robustness analysis (varying trap ratio): open- and closed-loop comparison around a late-phasing point: black dashed-(open loop), red solid-(closed loop)

time a new varying parameter is introduced to influence the system matrices.

7.3.4 Robust Analysis Examples

Using the recursive robustness algorithm developed, two robustness analysis examples are presented in this section.

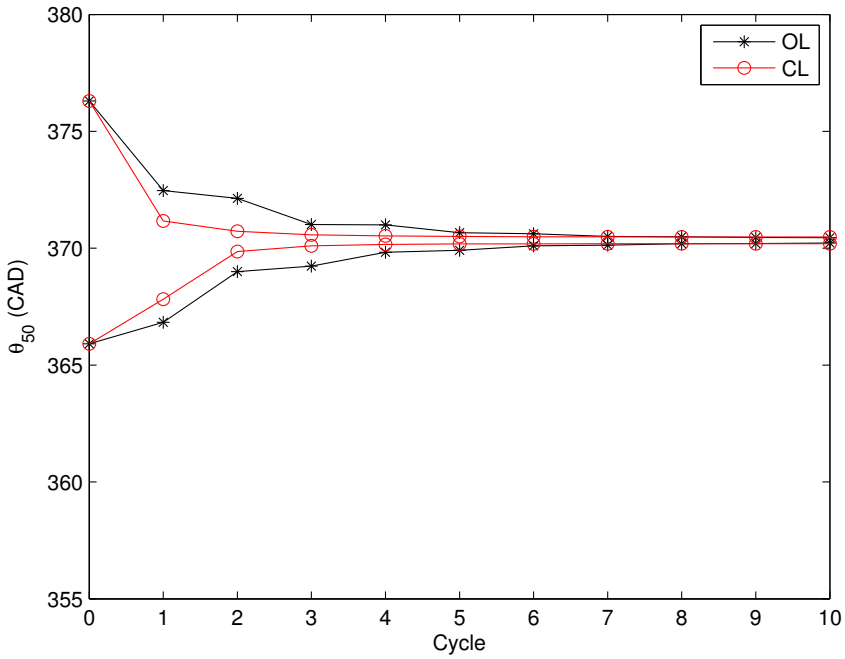

Figure 7.15: θ_{50} bounds (varying trap ratio): open- and closed-loop comparison around a late-phasing point.

Uncertainty in Trap Ratio: OL vs CL Late Phasing Operation

In this example, the late-phasing, open- and closed-loop analysis shown in Section 7.2.6 is revisited with the full detail of varying trap ratio. Due to the feedback controller changing the EVC, the trap ratio for the closed-loop late phasing scenario is assumed to be within the range of [0.495 0.525]. This range is estimated through observing the trap ratio of the nonlinear model. For the open-loop case, the trap ratio is bounded within the range of [0.505 0.515]. The smaller range in open loop is due to the fact that EVC is not changing in this case, and the trap ratio is only slightly perturbed around the nominal value by T_{θ_s} and T_{420}. Note that the full 15 CAD range of EVC movement useful on the experimental test bed roughly translates to a range of trap ratio of [0.49 0.61]. In this example, there is no uncertainty assumed in the combustion temperature map.

The resulting bounded sets are shown in Fig. 7.14 with the open-loop case shown

in the black, dashed line and the the closed-loop case shown in the red solid line. As can be seen, the qualitative behavior of the two cases remain unchanged. In general, the controller still shrinks the bounded sets in the "combustion timing" direction more aggressively than the open loop case. As before, the output equation of the nonlinear model can operate on each of the bounded sets shown in Fig. 7.14 and generate θ_{50} bounds for the two cases. These θ_{50} bounds are shown in Fig. 7.15. Again, the closed-loop controller can regulate combustion timing much more quickly compared to the open-loop case. The steady-state θ_{50} bounds in this case is wider compared to the bounds with a constant trap ratio shown in Fig. 7.13. Due to the uncertainty in the trap ratio in this robustness analysis, it is impossible for the algorithm to further decrease the size of the bounded sets and the θ_{50} bounds.

Bounded Disturbance on the Temperature State

Engine data typically exhibits some stochastic characteristics, as can be seen in all of the test bed responses shown in this thesis. One approach to account for this cycle-to-cycle variation in a deterministic model is by injecting a random disturbance. In this section, a cycle-to-cycle temperature disturbance, w_k, is assumed to influence the state propagation equation:

$$x_{k+1} = A(\zeta) \cdot x_k + B_1 \cdot u_k + B_2 \cdot g_{comb}(x_k) + d(\zeta) + e_2 \cdot w_k \tag{7.39}$$

where $e_2 = \begin{bmatrix} 0 & 1 \end{bmatrix}^T$ and $-T_{dis} \leq w_k \leq T_{dis}$

This disturbance, w_k, is bounded by a maximum magnitude but is otherwise unknown. Note that equation (7.39) readily fits the format of the robustness analysis, since the w_k can be viewed as an additional varying parameter and the system matrices (the bias term) is affinely dependent on it. In this example, no uncertainty exists in the combustion temperature map g_{comb}. The LPV model under the influence of w_k is examined at three sets of conditions: open-loop early-phasing operation as shown in the top plot of Fig. 4.1, open-loop late-phasing operation as shown in the bottom plot of Fig. 4.1, and closed-loop late-phasing operation as seen in the top plot of

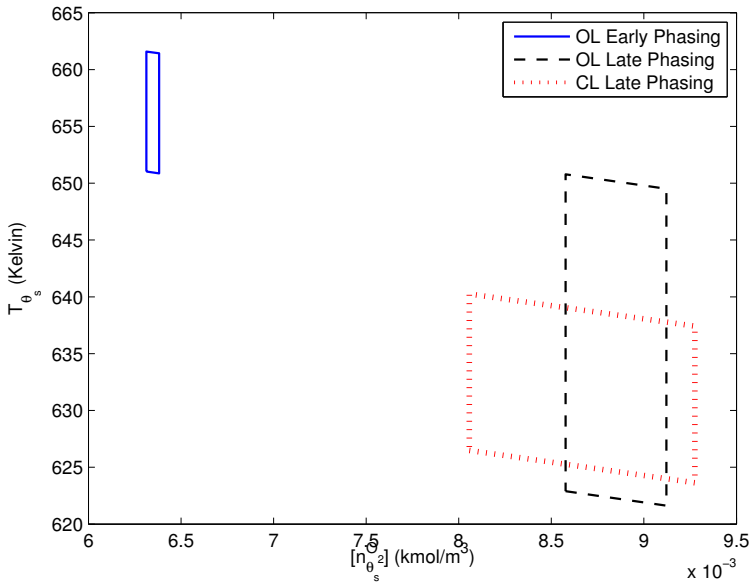

Figure 7.16: Steady-state invariant sets with bounded temperature disturbance: blue-(open loop, early phasing), black-(open loop, late phasing), red-(closed loop, late phasing)

Fig. 5.1. The engine data at these three sets of conditions is re-plotted in blue in Fig. 7.17. For the two open-loop cases, the trap ratios are allowed to vary in a range of ± 0.05 with respect to the nominal values. For the closed-loop case, ζ is within a bound of ± 0.15 with respect to the nominal value to account for the changing EVC.

The next step in this robustness analysis is determining an appropriate maximum magnitude, T_{dis}, of the disturbance w_k. To that end, a magnitude is first assumed and run through the robust algorithm with the first sets of conditions, i.e., open-loop early-phasing operation. The resulting steady-state invariant set can be used to generate a steady-state θ_{50} bound. This bound is then compared to the peak-to-peak variations exhibited in the test bed data, and the magnitude of w_k is tuned until the analytical θ_{50} bound matches reasonably well to the data. The same magnitude of w_k is then used for the other two scenarios. With this approach, the magnitude of w_k is found to be $-4.75\ \ Kelvin \leq w_k \leq 4.75\ \ Kelvin$.

The three resulting steady-state invariant sets for each cases is shown in Fig. 7.16.

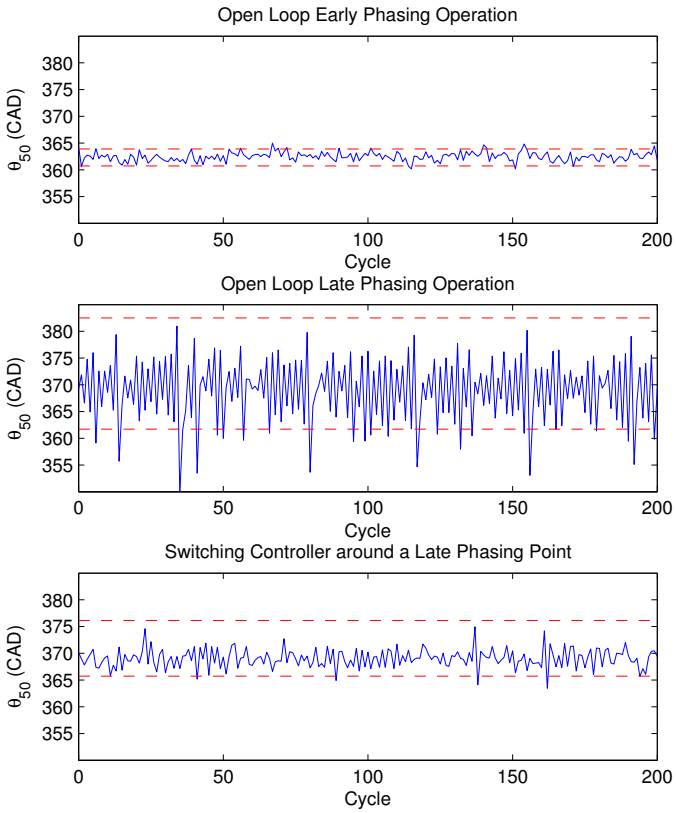

Figure 7.17: Steady-state θ_{50} bounds with bounded temperature disturbance

As can be seen, the invariant set for the open-loop early-phasing condition (blue) occupies the upper left corner of Fig. 7.16, which has higher temperature and lower oxygen content (due to the higher amount of trapped exhaust that is inhibiting fresh air induction). The relatively well-behaved early-phasing operation can be seen in the size of the steady-state invariant set, which is far smaller than the two invariant sets for late-phasing operation. The two late-phasing invariant sets match the intuition from observing the engine data and from the previous stability analysis around the late phasing point. As can be seen, the invariant set with the feedback controller is tighter in the "combustion timing" direction, but wider in the oxygen content direction. Three sets of steady-state θ_{50} bounds corresponding to three steady-state invariant sets shown in Fig. 7.16 can be calculated. These θ_{50} bounds are shown as

the red dashed lines, and are over-plotted with the engine data in Fig. 7.17. The qualitative behavior of the θ_{50} bounds match well to the intuition, i.e., the bounds are the tightest during early-phasing operation, the widest during open-loop late-phasing operation, and the feedback controller is able to shrink the θ_{50} bounds in closed-loop. Quantitatively, the θ_{50} bounds are reasonable too. In the top and bottom plot of Fig. 7.17, the engine data mostly lies within the red analytical bounds. In the middle plot, there are more data points exceeding the analytical lower bound on θ_{50}, and these data points are often preceded by a late combustion timing on the *previous* cycle. These excursions outside the bounds may be because the nonlinear model, which is based on various simplifying assumptions, does not capture some of the more complex behavior on the test bed when the combustion timing is extremely late.

7.4 Comparison of Stability Statements

Before the chapter is concluded, the stability statements obtained with the recursive algorithm and with the SDP in (5.25) are compared graphically. Note that these two analysis approaches establish stability statements for two different models, i.e., the LPV model and three-region switching linear model.

For the switching linear model, the positive-definite matrix, P, obtained with the SDP in (5.25) satisfies the following condition:

$$\overline{x}_k^T \cdot P \cdot \overline{x}_k - \overline{x}_{k+1}^T \cdot P \cdot \overline{x}_{k+1} \geq \gamma \cdot \overline{x}_k^T \cdot P \cdot \overline{x}_k \tag{7.40}$$

where $\overline{x}$ is the system states of the switching linear model, and γ is the corresponding dissipation rate. Therefore, given a set of initial conditions, $\overline{x}_0$, defined by the α-sublevel set of the Lyapunov function:

$$\overline{x}_0 = \left\{ s \;\middle|\; s^T \cdot P \cdot s \leq \alpha \right\} \tag{7.41}$$

the state trajectories of the switching linear model can be bounded with the inequality shown in (7.40) on a cycle-by-cycle basis. Specifically, the system states on the n_{th}

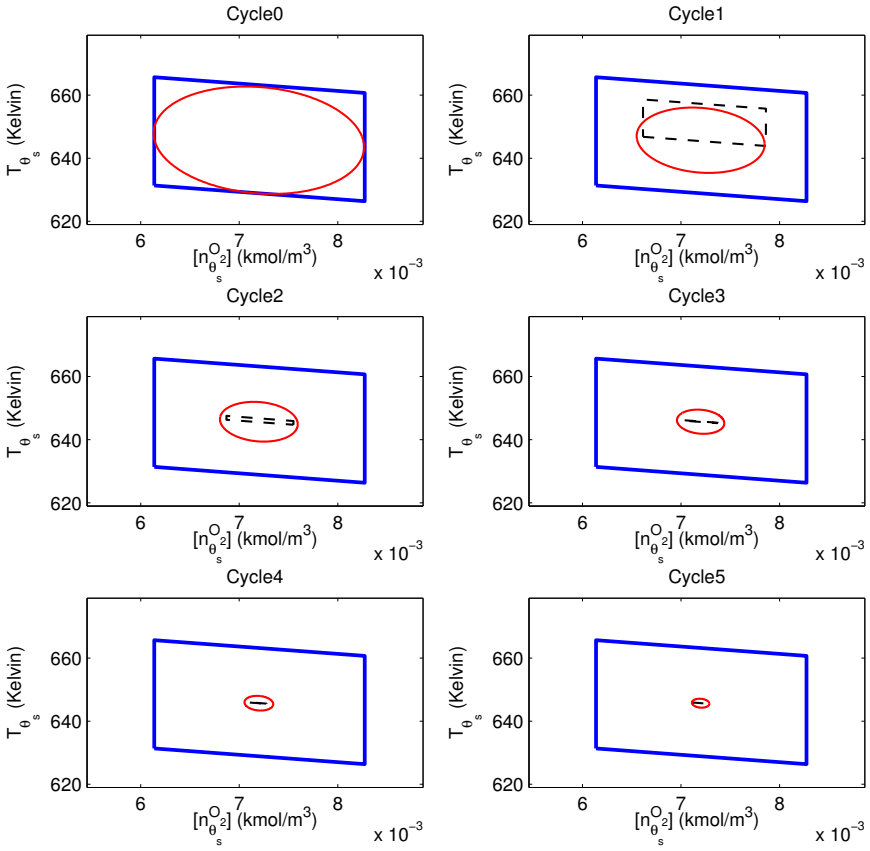

Figure 7.18: Comparison of stability statements

cycle, $\overline{x}_n$, satisfy the following inequality:

$$\overline{x}_n^T \cdot P \cdot \overline{x}_n \leq (1-\gamma)^n \cdot \alpha \tag{7.42}$$

Essentially, the above inequality defines a sequence of ellipsoids in the state space that bounds the state trajectories of the switching linear model, and is plotted in Fig. 7.18. In the same figure, a sequence of polytopes that bounds the state trajectories of the LPV model is also plotted. The nominal firing zone is the area enclosed by the blue solid line (shown in every subplot as a reference), which is chosen to have a similar size to the initial ellipsoid shown in the first subplot. The sequence of

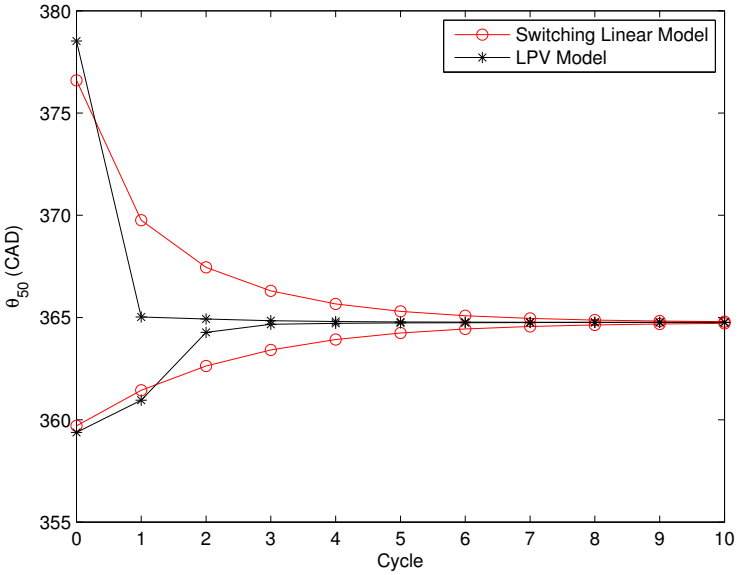

Figure 7.19: θ_{50} bounds: switching linear model vs. LPV model

polytopes defined by the black dashed lines shows how the state trajectories of the LPV model converge.

As shown in Fig. 7.18, the convergence rates of the oxygen state with the two approaches are very similar for all cycles. This is because the oxygen dynamics show very little change over the state space, and across the two models (the oxygen dynamics are dictated by the fact that fifty to sixty percent of the exhaust is trapped in recompression HCCI).

The convergence of the temperature state first shows a similar rate on Cycle 1 for the two approaches, which is evident in the size of the ellipsoid and polytope in the "temperature state direction" in the second subplot of Fig. 7.18. However, the LPV model shows a much faster temperature convergence on Cycle 2 and thereafter. This is because the polytope for Cycle 1 is roughly within the range of the "sweet spot" region, and the recursive algorithm concludes that the temperature dynamics are strongly converging there. On the other hand, the SDP in (5.25) finds a single Lyapunov function and dissipation rate, γ, that works for *all* three local linearized models. Therefore, it is restricted by the slowest temperature convergence rate of the

three local models. In general, the ellipsoid shrinks slower than the polytopes in the "temperature state direction" in Fig. 7.18.

The output equation of the nonlinear model can be further applied to the sequence of ellipsoids and polytopes shown in Fig. 7.18 to give two sets of θ_{50} bounds for the switching linear model and LPV model, respectively. These θ_{50} bounds are shown in Fig. 7.19. Since the recursive algorithm generally concludes a faster temperature convergence, it is not surprising to see that the θ_{50} bounds of the LPV model shrinks much more quickly compared to those of the switching linear model.

7.5 Conclusion

In this chapter, a stability algorithm is presented to show the convergence of the two thermo-chemical conditions captured by the LPV model, i.e., oxygen content and temperature at 300 CAD. This algorithm relies on the "part linear and part bowl-shaped" structure of the LPV model. Essentially, the bowl-shaped combustion temperature map translates to the convexity of the state propagation equations and is exploited to make the proposed stability algorithm possible. Furthermore, this approach is readily generalizable to include model uncertainties and establish robustness statements of recompression HCCI. In the robustness analysis, the convexity of the combustion temperature map is relaxed and the system matrices can be affinely dependent on a set of varying parameters. Using this robustness analysis tool, the θ_{50} bounds corresponding to the steady-state invariant sets relate reasonably well to the test bed data. This is further evidence that the LPV model indeed captures the key characteristics of recompression HCCI, and that the robustness statements are sufficiently tight to be useful in practice.

Chapter 8

Conclusions and Future Work

8.1 Conclusions

Internal combustion engines are expected to continue dominating the ground transportation sector in the near future. This thesis discusses two technologies that can improve the efficiency and pollution of IC engines: an electro-hydraulic valve system and homogeneous charge compression ignition. However, each of them poses some challenges in controls. For the EHVS, the response time delay and the nonlinear dynamics hinders the closed-loop tracking performance. For HCCI, combustion timing control and robustness analyses are crucial as HCCI lacks explicit ignition triggers and is sensitive to the in-cylinder thermo-chemical conditions.

In Chapter 2, system identification techniques are applied to the EHVS and the resulting ETFE shows that a third-order linear model with input delay can be used to approximate the system dynamics. Two model-based feedback controllers are compared in experiments and both of them cannot achieve as accurate position control as when using a mechanical cam. Fundamentally, the response time delay limits the achievable closed-loop bandwidth which translates to inadequate tracking performance. To address this problem, a repetitive controller is formulated. This controller generates a feedforward input trajectory adaptively to augment the feedback controller. The combined control law achieves excellent tracking performance in experiments under various operating conditions. The proposed control framework is stable

in both experiments and a stability analysis. Finally, a steady-state variance analysis on the mean tracking error is presented that can be used to examine the effect of valve position sensor noise on the presented control law.

Starting from Chapter 3, this thesis shifts its focus to recompression HCCI. In Chapter 3, the single-zone, nonlinear model developed by Ravi *et al.* [38] is first summarized, since it serves as a stepping stone for the work presented in this thesis. This nonlinear model captures the cycle-to-cycle propagation of the in-cylinder oxygen content and temperature, and defines a discrete-time two-state nonlinear model. In Chapter 4, two sets of open-loop combustion timing data from the testbed demonstrate that the cycle-to-cycle dynamics of recompression HCCI can change dramatically around different operating points. This further complicates the two main challenges in controlling HCCI combustion timing, i.e., the lack of explicit ignition triggers and the cycle-to-cycle coupling due to reutilizing the exhaust gas. To understand the change in the combustion timing dynamics, the temperature dynamics of the nonlinear model is subjected to a graphical analysis. The resulting visualization of the temperature trajectories reveals three types of qualitative temperature dynamics across a wide range of ignition phasing: smoothly decaying in the early phasing region, oscillatory in the late phasing region, and strongly converging in between. With this insight, a three-region switching linear model is proposed as a minimalist approach of capturing the qualitative change in system behavior for control purposes.

In Chapter 5, a three-region switching controller is presented based on the switching linear model. This controller successfully controls the θ_{50} in a wide range of conditions. Particularly, the highly oscillatory combustion timing response around the late phasing operating point shown in the bottom plot of Fig. 4.1 is rendered usable with the switching controller. Effectively, the permissible operating range of recompression HCCI is made wider in closed-loop. This chapter further presents two semi-definite programs to guarantee that the gain-scheduling formulation in the switching control/model is stable.

Chapter 6 presents a linear parameter varying model with the explicit aim of providing a tractable platform for stability and robustness analysis of recompression HCCI . Based on the nonlinear model, this LPV model lumps the key nonlinearity of

the nonlinear model into two varying parameters and uses linear equations to complete the state propagation from one cycle to the next. The result is a tremendous reduction in model complexity compared to the nonlinear model. The LPV is examined in various numerical examples and agrees well to the nonlinear model in all cases. When the LPV and the nonlinear model are further compared to the testbed data, the results show that the day-to-day variation of the testbed exceeds the difference between the two models. As a result, basing the stability and robustness analysis on the LPV model is essentially equivalent to using the nonlinear model.

In Chapter 7, a recursive stability algorithm is first presented to establish the convergence of the state trajectories of the LPV model. This stability algorithm takes advantage of the "bowl-shaped" relationship between the model states and the exhaust temperature, the varying parameter that summarizes the dominant nonlinearity in recompression HCCI. When the "bowl-shaped" relationship is formally characterized as a convex function, the problem of finding invariant sets can be solved very efficiently with the proposed recursive algorithm. This approach can be further generalized to include model uncertainties and becomes a tool for analyzing the robustness properties of HCCI, which, to the best of the author's knowledge, has not been reported yet in previous work. It is also shown that the robustness statements generated by the proposed algorithm relate reasonably well to the testbed data in both open and closed-loop.

8.2 Future Work

The repetitive controller shown in Chapter 2 shows excellent tracking performance in steady state, but it does take some finite time for the controller to converge to a new input trajectory when a different valve profile is switched. One possibility to address this is hinted by Equation (2.15), given again below:

$$\overline{y}^{(k)} = T_1 \cdot \overline{y}_{des} + T_2 \cdot \overline{u}_{rep}^{(k)}$$

Considering the first engine cycle, cycle 0, if perfect tracking is to be achieved, then the following condition holds: $\overline{y}^{(0)} = \overline{y}_{des}$. Substituting this condition into Equation (2.15) gives:

$$\overline{y}_{des} = T_1 \cdot \overline{y}_{des} + T_2 \cdot \overline{u}^{(0)}_{rep}$$

Rearranging the above gives:

$$(I - T_1) \cdot \overline{y}_{des} = T_2 \cdot \overline{u}^{(0)}_{rep}$$

Therefore, if the square matrix T_2 is invertible, it seems that one can obtain an educated guess on the initial repetitive control input trajectory, $\overline{u}^{(0)}_{rep}$, which can potentially make the repetitive controller converge faster.

In Chapter 4 and 5, the EVC is the only input that can control combustion timing. Since fully flexible variable valve actuation is generally considered too costly for production engines, it would be interesting to see if the three-region switching control/model framework can be generalized to include other more production-friendly inputs such as pilot injection timing and fuel quantity. Furthermore, the framework outlined in these two chapters is also generalizable to include more model regions than the three presented. It should not be surprising that increasing the model regions can further improve control performance. However, further experimental study is required to see if the incremental gain in performance justifies the increase in controller complexity. Lastly, the feedback control gain for the sweet spot region shown in Equation (5.4) is close to zero, suggesting that there is an operating region of recompression HCCI where combustion timing can be reliably controlled in open loop. This idea can be verified in experiments by setting the feedback gain of the sweet spot region to zero, while retaining the feed-forward control action.

Chapter 6 shows that the varying parameter, T_{420} (the exhaust temperature), summarizes the dominant nonlinearity in recompression HCCI and influences the states on the next engine cycle *linearly*. If this varying parameter can be estimated, it should be possible to use it as a feedback signal and design a linear feedback controller based on T_{420} (instead of the linear state feedback controllers in Chapter 5). This can potentially lead to an elegant, static linear feedback implementation

that works across a wide operating range.

Chapter 6 also shows that the LPV model can capture the effect of environmental parameters such as intake manifold pressure, intake air temperature and cylinder wall temperature on the two states by updating the linearizations of the breathing stage on a cycle-by-cycle basis. The resulting state trajectories follow closely those of the nonlinear model. While the author is confident that the nonlinear model captures the qualitative effect of these environmental parameters on the system states, it remains unclear if their effects make sense quantitatively. Further experimental studies need to be conducted to verify this. Once the effect of these environmental parameters is ascertained, the author envisions that the robustness algorithm presented in Chapter 7 can be used to see if recompression HCCI is robust to the range of environmental conditions that a production engine faces in its lifetime.

Appendix A

Derivation of the Nonlinear Model

Chapter 3 summarizes the equations in each of the seven sub-models of the nonlinear model. These equations propagate the in-cylinder oxygen content and temperature from the beginning to the end of a stage, and are derived in this appendix.

Stage 1: Polytropic compression from 300 CAD to ignition

The end of this stage is the ignition point defined by the Arrhenius reaction rate model shown in Equation (3.2). Once the ignition timing is determined, the cylinder volume at the start of combustion, V_{ign}, is known. The pressure propagation during this stage is assumed to follow a polytropic compression process, i.e.,

$$p_{\theta_s} \cdot V_{\theta_s}^{\kappa_1} = p_{ign} \cdot V_{ign}^{\kappa_1} \tag{A.1}$$

The parameter, κ_1, is the polytropic exponent during this stage and is assumed constant. In the rest of the model stages, a similar convention is adopted, i.e., κ_i is the polytropic exponent for **Stage** i. By using the ideal gas law, and assuming a constant total amount of gas in the cylinder, the temperature propagation during

this stage can be derived:

$$\begin{aligned} p_{\theta_s} \cdot V_{\theta_s}^{\kappa_1} &= p_{ign} \cdot V_{ign}^{\kappa_1} \\ \frac{T_{\theta_s} \cdot R \cdot n_{\theta_s}}{V_{\theta_s}} \cdot V_{\theta_s}^{\kappa_1} &= \frac{T_{ign} \cdot R \cdot n_{ign}}{V_{ign}} \cdot V_{ign}^{\kappa_1} \\ T_{\theta_s} \cdot V_{\theta_s}^{\kappa_1 - 1} &= T_{ign} \cdot V_{ign}^{\kappa_1 - 1} \end{aligned}$$

Rearranging terms give:

$$T_{ign} = T_{\theta_s} \cdot \left(\frac{V_{\theta_s}}{V_{ign}} \right)^{\kappa_1 - 1}$$

which gives the result shown in Equation (3.6) as desired.

The total amount of oxygen content in the cylinder during this stage is assumed constant, i.e.,

$$n_{ign}^{O_2} = n_{\theta_s}^{O_2}$$

Stage 2: Constant-duration combustion from ignition to end of combustion

Combustion is modelled as a two-step process with a constant duration. In the first step, the temperature at the ignition point, T_{ign}, is propagated to the end of combustion point assuming a polytropic process (without any energy addition from fuel oxidation):

$$T_{eoc}^{'} = T_{ign} \cdot \left(\frac{V_{ign}}{V_{eoc}} \right)^{\kappa_2 - 1} \tag{A.2}$$

In the above equation, the in-cylinder temperature is first propagated to an intermediate temperature, $T_{eoc}^{'}$, in this two-step combustion model. In the second step, this intermediate temperature is further related to the actual T_{eoc} by assuming an instantaneous energy conversion from fuel oxidation at the end of combustion point.

Gasoline is assumed to have the formula C_7H_{13}. The stoichiometric combustion reaction can be expressed as:

$$C_7H_{13} + 10.25 \cdot O_2 \rightarrow 7 \cdot CO_2 + 6.5 \cdot H_2O \tag{A.3}$$

By assuming a lean mixture typical in HCCI, the reaction starting with n_{ign}^{f} moles of gasoline and $n_{ign}^{O_2}$ moles of oxygen can be written as:

$$n_{ign}^{f} \cdot C_7H_{13} + n_{ign}^{O_2} \cdot O_2 \rightarrow 7 \cdot n_{ign}^{f} \cdot CO_2 + 6.5 \cdot n_{ign}^{f} \cdot H_2O \quad + (n_{ign}^{O_2} - 10.25 \cdot n_{ign}^{f}) \cdot O_2$$

Note that the total number of moles of gas in the cylinder is increased by an amount of $2.25 \cdot n_{ign}^{f}$ after the combustion. Since the energy conversion is assumed instantaneous at constant cylinder volume, there is no $p \cdot dV$ work during the reaction. The reaction is modelled as a simple energy addition without describing the chemical changes in the cylinder. As a result, applying the first law to the reaction gives:

$$U_{eoc} = U_{eoc}^{'} + Q^{comb} \tag{A.4}$$

where $U_{eoc}^{'}$ and U_{eoc} are the total internal energy of the in-cylinder gas immediately before and after the reaction, and Q^{comb} is the amount of energy addition to the in-cylinder gas. This energy addition is a function of the energy release from fuel oxidation as well as the heat transfer to the cylinder wall:

$$Q^{comb} = Q^{er} - Q^{ht}$$

For the purpose of this first law analysis, the energy release, Q^{er}, is calculated based on the lower heating value of the fuel:

$$Q^{er} = LHV_f \cdot n_{ign}^{f} \tag{A.5}$$

The amount of heat transfer, Q^{ht}, is modelled as a fixed percentage of the lower heating value of the fuel:

$$Q^{ht} = \epsilon \cdot LHV_f \cdot n^f_{ign} \tag{A.6}$$

where ϵ is a heat transfer parameter to be calibrated to the engine testbed. Combining Equation (A.4), (A.5) and (A.6) gives:

$$\begin{aligned} U_{eoc} &= U^{'}_{eoc} + Q^{comb} \\ &= U^{'}_{eoc} + (1-\epsilon) \cdot LHV_f \cdot n^f_{ign} \end{aligned} \tag{A.7}$$

Assuming that all the cylinder constituents other than the fuel have the same specific heat, C_v, and that the fuel has the the specific heat of $C_{v,f}$, Equation (A.7) can be written as:

$$\begin{aligned} & n_{eoc} \cdot C_v \cdot \left(T_{eoc} - T^{amb}\right) \\ & \quad = \left[\left(n^{'}_{eoc} - n^f_{ign}\right) \cdot C_v + n^f_{ign} \cdot C_{v,f}\right] \cdot \left(T^{'}_{eoc} - T^{amb}\right) + (1-\epsilon) \cdot LHV_f \cdot n^f_{ign} \end{aligned} \tag{A.8}$$

The ambient temperature, T^{amb}, is the reference temperature in this first law analysis. The total number of moles of gas immediately before combustion, $n^{'}_{eoc}$, is assumed to be equal to the amount of gas at the ignition and state definition point, i.e.,

$$n^{'}_{eoc} = n_{ign} = n_{\theta_s} \tag{A.9}$$

As pointed out previously, the total amount of gas after combustion is increased by an amount of $2.25 \cdot n^f_{ign}$. Furthermore, the amount of fuel at the ignition point, n^f_{ign}, is the same at the state definition point. These give:

$$\begin{aligned} n_{eoc} &= n^{'}_{eoc} + 2.25 \cdot n^f_{ign} \\ &= n_{\theta_s} + 2.25 \cdot n^f_{\theta_s} \end{aligned} \tag{A.10}$$

Combining Equation (A.8), (A.9) and (A.10) gives:

$$\begin{aligned}\left(n_{\theta_s}+2.25\cdot n^f_{\theta_s}\right)\cdot C_v\cdot\left(T_{eoc}-T^{amb}\right)\\ =\left[\left(n_{\theta_s}-n^f_{\theta_s}\right)\cdot C_v+n^f_{\theta_s}\cdot C_{v,f}\right]\cdot\left(T'_{eoc}-T^{amb}\right)+(1-\epsilon)\cdot LHV_f\cdot n^f_{\theta_s}\end{aligned} \tag{A.11}$$

Note that the term, $\left(n_{\theta_s}-n^f_{\theta_s}\right)\cdot C_v+n^f_{\theta_s}\cdot C_{v,f}$, in the above equation represents the product of the average specific heat and total amount of gas immediately before the reaction. Similarly, the term $\left(n_{\theta_s}+2.25\cdot n^f_{\theta_s}\right)\cdot C_v$ represents the product of the specific heat and total amount of gas after the reaction. Rearranging and solving for T_{eoc} gives:

$$\begin{aligned}T_{eoc}=&\frac{C_v\cdot n_{\theta_s}+(C_{v,f}-C_v)\cdot n^f_{\theta_s}}{C_v\cdot\left(n_{\theta_s}+2.25\cdot n^f_{\theta_s}\right)}\cdot T'_{eoc}\\ &+\frac{(1-\epsilon)\cdot LHV_f+(3.25\cdot C_v-C_{v,f})\cdot T^{amb}}{C_v\cdot\left(n_{\theta_s}+2.25\cdot n^f_{\theta_s}\right)}\cdot n^f_{\theta_s}\end{aligned} \tag{A.12}$$

A simplification can be made in Equation (A.12). Since $n^f_{\theta_s}\ll n_{\theta_s}$, it is reasonable to assume that the product of the specific heat and total amount of gas does not change significantly before and after the combustion, i.e.,

$$C_v\cdot n_{\theta_s}+(C_{v,f}-C_v)\cdot n^f_{\theta_s}\cong C_v\cdot\left(n_{\theta_s}+2.25\cdot n^f_{\theta_s}\right)$$

Using this simplification, Equation (A.12) can be combined with Equation (A.2) to give:

$$\begin{aligned}T_{eoc}=&T'_{eoc}+\frac{(1-\epsilon)\cdot LHV_f+(3.25\cdot C_v-C_{v,f})\cdot T^{amb}}{C_v\cdot n_{\theta_s}+(C_{v,f}-C_v)\cdot n^f_{\theta_s}}\\ =&T_{ign}\cdot\left(\frac{V_{ign}}{V_{eoc}}\right)^{\kappa_2-1}+\frac{(1-\epsilon)\cdot LHV_f+(3.25\cdot C_v-C_{v,f})\cdot T^{amb}}{C_v\cdot n_{\theta_s}+(C_{v,f}-C_v)\cdot n^f_{\theta_s}}\end{aligned} \tag{A.13}$$

which is the same results shown in Equation (3.8).

Since a lean mixture is assumed, the leftover oxygen content at the end of combustion point is calculated as:

$$n_{eoc}^{O_2} = n_{ign}^{O_2} - \lambda_{stoich} \cdot n_{\theta_s}^{f}$$

where $\lambda_{stoich} = 10.25$ is the stoichiometric oxygen-fuel ratio as observed in Reaction (A.3).

Stage 3: Polytropic expansion from EOC to EVO

The post-combustion expansion is assumed to be a polytropic process, as a result, the temperature propagation during this stage is:

$$T_{evo} = T_{eoc} \cdot \left(\frac{V_{eoc}}{V_{evo}}\right)^{\kappa_3 - 1}$$

The oxygen content during this stage is unchanged, i.e.,

$$n_{evo}^{O_2} = n_{eoc}^{O_2}$$

Stage 4: Polytropic blowdown and exhaust from EVO to EVC

The exhaust process is modelled as a two-step process as well. The first step is a polytropic blowdown process where the in-cylinder gas expands to the exhaust manifold pressure, p^{em}. Along with the ideal gas law, the temperature propagation during this stage can be obtained:

$$T_{evc} = T_{evo} \cdot \left(\frac{p^{em}}{p_{evo}}\right)^{1 - \frac{1}{\kappa_4}} \tag{A.14}$$

After the blowdown, the amount of gas trapped in the cylinder at EVC, n_{evc}, can be calculated based on the ideal gas law with the assumption that the pressure inside the cylinder is equal to the exhaust manifold pressure.

$$n_{evc} = \frac{p^{em} \cdot V_{evc}}{R \cdot T_{evc}}$$

The trap ratio, ζ, defined in Chapter 6, i.e., the ratio between the amount of gas at EVC and EVO, can be calculated as:

$$\zeta = \frac{n_{evc}}{n_{evo}} = \frac{p^{em} \cdot V_{evc}}{R \cdot T_{evc} \cdot n_{evo}} \tag{A.15}$$

The amount of oxygen at EVC is, therefore, given as follows:

$$n_{evc}^{O_2} = \zeta \cdot n_{evo}^{O_2}$$

which is the same relationship given in Equation (3.11).

Stage 5: Recompression from EVC to IVO

The total amount of gas is assumed constant during this stage.

$$n_{ivo} = n_{evc}$$

This is because the engine valves are closed during this stage and the quantity of fuel injection, which typically occurs during recompression, is negligible compared to the total amount of gas in the cylinder.

Assuming no net work is done on the in-cylinder gas, the first law analysis during recompression is expressed as:

$$U_{ivo} = U_{evc} - Q^{recomp} \tag{A.16}$$

where U_{evc} and U_{ivo} are the total internal energy of the in-cylinder gas at the beginning and end of recompression, and Q^{recomp} is the amount of heat transfer during this stage. As a simple construct to capture the wall temperature effect, Q^{recomp} is modelled as proportional to the difference between the wall temperature and average gas temperature during recompression.

$$Q^{recomp} = h \cdot \left(T^{avg} - T^{wall}\right) \tag{A.17}$$

where h is a lumped heat transfer parameter that can be adjusted to capture the testbed behavior. The average gas temperature, T^{avg}, is modelled as the arithmetic mean of the gas temperature at EVC and the isentropic gas temperature at TDC.

$$T^{avg} = \frac{1}{2} \cdot \left(T_{evc} + T_{evc} \cdot \left(\frac{V_{evc}}{V^{tdc}} \right)^{\gamma - 1} \right) \tag{A.18}$$

where γ is the specific heat ration of the in-cylinder gas.

Combining Equation (A.16), (A.17) and (A.18) gives:

$$\begin{aligned} n_{ivo} \cdot C_v \cdot \left(T_{ivo} - T^{amb} \right) =& n_{evc} \cdot C_v \cdot \left(T_{evc} - T^{amb} \right) \\ & - h \cdot \left(\frac{1}{2} \cdot \left(T_{evc} + T_{evc} \cdot \left(\frac{V_{evc}}{V^{tdc}} \right)^{\gamma - 1} \right) - T^{wall} \right) \end{aligned}$$

Since $n_{ivo} = n_{evc}$, rearranging terms in the equation above gives:

$$T_{ivo} = T_{evc} - \frac{h}{n_{ivo} \cdot C_v} \cdot \left(\frac{1}{2} \cdot T_{evc} \cdot \left(1 + \left(\frac{V_{evc}}{V^{tdc}} \right)^{\gamma - 1} \right) - T^{wall} \right)$$

which is the results shown in Equation (3.14).

The oxygen content during this stage is assumed constant, i.e.,

$$n_{ivo}^{O_2} = n_{evc}^{O_2}$$

Stage 6: Adiabatic induction from IVO to IVC

Fresh air is inducted into the cylinder during this stage at a constant pressure and temperature (assumed to be the intake manifold pressure, p^{im}, and temperature, T^{im}, respectively). The inducted air is assumed to mix with the cylinder constituents instantaneously at IVC. Assuming no other work interaction and heat transfer takes place, the increase in the total internal energy inside the cylinder is equal to the enthalpy in-flow of fresh air. This gives:

$$n_{ivc} \cdot C_v \cdot T_{ivc} - n_{ivo} \cdot C_v \cdot T_{ivo} = n^{ind} \cdot C_p \cdot T^{im} \tag{A.19}$$

The left side of the above equation represents the change in the total internal energy in the cylinder, and the right side represents the enthalpy inflow of fresh air.

Assuming the in-cylinder pressure at IVC is equal to the intake manifold pressure gives the relationship of $n_{ivc} \cdot T_{ivc} = \frac{p^{im} \cdot V_{ivc}}{R}$. Substituting this relationship into Equation (A.19) gives:

$$C_v \cdot \frac{p^{im} \cdot V_{ivc}}{R} - n_{ivo} \cdot C_v \cdot T_{ivo} = n^{ind} \cdot C_p \cdot T^{im} \tag{A.20}$$

Rearranging terms and solving for n^{ind} gives the amount of air inducted:

$$n^{ind} = \frac{C_v}{C_p \cdot R \cdot T^{im}} \cdot \left(p^{im} \cdot V_{ivc} - n_{ivo} \cdot R \cdot T_{ivo}\right) \tag{A.21}$$

Using the ideal gas law, the in-cylinder temperature at IVC, T_{ivc}, can be calculated based on n^{ind}:

$$T_{ivc} = \frac{p^{im} \cdot V_{ivc}}{R \cdot (n_{ivo} + n^{ind})} \tag{A.22}$$

The amount of oxygen in the cylinder at IVC is the sum of the oxygen content at IVO and the oxygen content in the inducted air:

$$n_{ivc}^{O_2} = n_{ivo}^{O_2} + \chi \cdot n^{ind} \tag{A.23}$$

where χ is the molar concentration of oxygen of air (around 0.2).

Stage 7: Polytropic compression from IVC to θ_s

During this stage, the temperature of the in-cylinder gas is propagated by a polytropic process. This gives:

$$T_{\theta_s}(k+1) = T_{ivc}(k) \cdot \left(\frac{V_{ivc}(k)}{V_{\theta_s}}\right)^{\kappa_7 - 1}$$

Note the cycle index k in the above equation. It signifies that the temperature propagation has completed a full cycle to reach the state definition point on the *next*

engine cycle.

The oxygen content does not change during this stage, i.e.,

$$n_{\theta_s}^{O_2}(k+1) = n_{ivc}^{O_2}(k)$$

Appendix B

Re-Normalization of the Linearized Models

In the following example, two linearizations are re-normalized to arrive at an unified state, input and output description. The case with three linearizations are straight forward given this example. Consider the following two linearized models:

$$\tilde{x}_1(k+1) = \tilde{A}_1 \cdot \tilde{x}_1(k) + \tilde{B}_1 \cdot \tilde{u}_1(k) \quad , \quad \tilde{y}_1(k) = \tilde{C}_1 \cdot \tilde{x}_1(k) \tag{B.1}$$

and

$$\tilde{x}_2(k+1) = \tilde{A}_2 \cdot \tilde{x}_2(k) + \tilde{B}_2 \cdot \tilde{u}_2(k) \quad , \quad \tilde{y}_2(k) = \tilde{C}_2 \cdot \tilde{x}_2(k) \tag{B.2}$$

Note that the $\tilde{x}_1$ and $\tilde{x}_2$ are normalized around different steady state oxygen concentration and temperature. Specifically:

$$\tilde{x}_1 = \begin{bmatrix} \frac{n_{\theta_s}^{O_2} - n_{\theta_s,1}^{O_2}}{n_{\theta_s,1}^{O_2}} \\ \frac{T_{\theta_s} - T_{\theta_s,1}}{T_{\theta_s,1}} \end{bmatrix} \quad and \quad \tilde{x}_2 = \begin{bmatrix} \frac{n_{\theta_s}^{O_2} - n_{\theta_s,2}^{O_2}}{n_{\theta_s,2}^{O_2}} \\ \frac{T_{\theta_s} - T_{\theta_s,2}}{T_{\theta_s,2}} \end{bmatrix} \tag{B.3}$$

where $n_{\theta_s,1}^{O_2}$, $T_{\theta_s,1}$ are the steady-state oxygen content and temperature for the first linearized system and $n_{\theta_s,2}^{O_2}$, $T_{\theta_s,2}$ are the steady-state values for the second linearized

system. To express $\tilde{x}_2$ in terms of $\tilde{x}_1$, the following transformation can be used:

$$\tilde{x}_2 = \alpha^{-1} \cdot (\tilde{x}_1 - \beta) \tag{B.4}$$

where

$$\alpha = \begin{bmatrix} \frac{O_{2,2}}{O_{2,1}} & 0 \\ 0 & \frac{T_2}{T_1} \end{bmatrix}, \quad \beta = \begin{bmatrix} \frac{O_{2,2}-O_{2,1}}{O_{2,1}} \\ \frac{T_2-T_1}{T_1} \end{bmatrix} \tag{B.5}$$

Since the two linear models have different steady state volume at EVC and different steady state θ_{50}, similar relationships between u_k and $\tilde{u}_k$ and between y_k and $\tilde{y}_k$ need to be established as well:

$$\tilde{u}_2 = \alpha_u^{-1} \cdot (\tilde{u}_1 - \beta_u) \tag{B.6}$$

$$\tilde{y}_2 = \alpha_y^{-1} \cdot (\tilde{y}_2 - \beta_y) \tag{B.7}$$

where

$$\alpha_u = \frac{V_{EVC,2}}{V_{EVC,1}}, \quad \beta_u = \frac{V_{EVC,2} - V_{EVC,1}}{V_{EVC,1}} \tag{B.8}$$

$$\alpha_y = \frac{\theta_{50,2}}{\theta_{50,1}}, \quad \beta_y = \frac{\theta_{50,2} - \theta_{50,1}}{\theta_{50,1}} \tag{B.9}$$

The second linear system can be expressed using $\tilde{x}_1$, $\tilde{u}_1$ and $\tilde{y}_1$ instead of $\tilde{x}_2$, $\tilde{u}_2$ and $\tilde{y}_2$:

$$\begin{aligned} \tilde{x}_1(k) &= \alpha \cdot \tilde{A}_2 \cdot \alpha^{-1} \cdot \tilde{x}_1(k) + \alpha \cdot \tilde{B}_2 \cdot \alpha_u^{-1} \cdot \tilde{u}_1(k) \\ &\quad + \alpha \cdot (I - \tilde{A}_2) \cdot \alpha^{-1} \cdot \beta - \alpha \cdot \tilde{B}_2 \cdot \alpha_u^{-1} \cdot \beta_u \\ \tilde{y}_1(k) &= \alpha_y \cdot \tilde{C}_2 \cdot \alpha^{-1} \cdot \tilde{x}_1 + \beta_y - \alpha_y \cdot \tilde{C}_2 \cdot \alpha^{-1} \cdot \beta \end{aligned} \tag{B.10}$$

Introducing the following definitions to simplify the notations:

$$\begin{aligned} A_2 &= \alpha \cdot \tilde{A}_2 \cdot \alpha^{-1}, \quad B_2 = \alpha \cdot \tilde{B}_2 \cdot \alpha_u^{-1}, \quad C_2 = \alpha_y \cdot \tilde{C}_2 \cdot \alpha^{-1} \\ d_2 &= \alpha \cdot (I - \tilde{A}_2) \cdot \alpha^{-1} \cdot \beta - \alpha \cdot \tilde{B}_2 \cdot \alpha_u^{-1} \cdot \beta_u \\ e_2 &= \beta_y - \alpha_y \cdot \tilde{C}_2 \cdot \alpha^{-1} \cdot \beta \end{aligned} \tag{B.11}$$

The second linear system becomes:

$$\begin{aligned} \tilde{x}_1(k) &= A_2 \cdot \tilde{x}_1(k) + B_2 \cdot \tilde{u}_1(k) + d_2 \\ \tilde{y}_1(k) &= C_2 \cdot \tilde{x}_1(k) + e_2 \end{aligned} \tag{B.12}$$

(B.4) $\sim$ (B.12) can be generalized to re-normalize any number of linearized systems.

Appendix C

Proof of Theorem 7.3

The lower bound on oxygen content on the next cycle is given in **Theorem 7.3**, which is stated again and proven below.

Theorem 7.3 *Suppose J_n^* is the optimal objective of the linear program (LP) shown in* (C.1), with x_k and r_k as the optimization variables, then n_{k+1}^l can be chosen as $n_{k+1}^l = J_n^* + e_1^T B_1 \cdot u_k + e_1^T d$

$$\begin{aligned} &\textit{minimize} \quad e_1^T A \cdot x_k + e_1^T B_2 \cdot r_k \\ &\textit{subject to}: \\ &x_k \in \Phi_k \\ &r_k \geq T_{420}^{s,i} + {q_i}^T \cdot (x_k - x^{s,i}), \quad \forall i = 1, ..., m \end{aligned} \tag{C.1}$$

Proof:

Suppose that the LP in (C.1) is sovled with the optimizers x_k^* and r_k^* with the optimal objective J_n^*. This means that any choice of x_k of r_k that satisfy the constraints shown in the above LP cannot yield a objective value lower than J_n^*.

It is obvious that the following condition holds :

$$\begin{aligned} J_n^* &= e_1^T A \cdot x_k^* + e_1^T B_2 \cdot r_k^* \\ x_k^* &\in \Phi_k \\ r_k^* &\geq \max_{i=1,\ldots,m} \left\{ T_{420}^{s,i} + {q_i}^T \cdot (x_k^* - x^{s,i}) \right\} \end{aligned} \tag{C.2}$$

These come directly from the LP problem statements. The last condition can be further refined:

$$r_k^* = \max_{i=1,\ldots,m} \left\{ T_{420}^{s,i} + {q_i}^T \cdot (x_k^* - x^{s,i}) \right\} \tag{C.3}$$

Condition (C.3) can be proven with the following argument. Suppose (C.2) is a strict inequality, i.e.

$$r_k^* > \max_{i=1,\ldots,m} \left\{ T_{420}^{s,i} + {q_i}^T \cdot (x_k^* - x^{s,i}) \right\}$$

Since $e_1^T B_2$ is always positive, there always exists a z^* and V^* such that

$$\begin{aligned} & r_k^* > z^* \geq \max_{i=1,\ldots,m} \left\{ T_{420}^{s,i} + {q_i}^T \cdot (x_k^* - x^{s,i}) \right\} \\ & \textit{and} \\ & J_n^* > V^* = e_1^T A \cdot x_k^* + e_1^T B_2 \cdot z^* \end{aligned}$$

Therefore, J_n^* cannot be the optimal objective value of the optimization problem, since $J_n^* > V^*$. This is a contradiction and, as a result, the equality condition in (C.3) has to be true. Furthermore, the condition below needs to hold:

$$\begin{aligned} J_n^* &= e_1^T A \cdot x_k^* + e_1^T B_2 \cdot r_k^* \\ &= e_1^T A \cdot x_k^* + e_1^T B_2 \cdot \max_{i=1,\ldots,m} \left\{ T_{420}^{s,i} + {q_i}^T \cdot (x_k^* - x^{s,i}) \right\} \\ &\leq e_1^T A \cdot x_k + e_1^T B_2 \cdot \max_{i=1,\ldots,m} \left\{ T_{420}^{s,i} + {q_i}^T \cdot (x_k - x^{s,i}) \right\}, \quad \forall x_k \in \Phi_k \end{aligned} \tag{C.4}$$

The second equality in the above comes from condition (C.3) that was just proved. If condition (C.4) were not true, then there exists a $s^* \in \Phi_k$ such that

$$\begin{aligned} J_n^* &= e_1^T A \cdot x_k^* + e_1^T B_2 \cdot \max_{i=1,\ldots,m} \left\{ T_{420}^{s,i} + {q_i}^T \cdot (x_k^* - x^{s,i}) \right\} \\ &> e_1^T A \cdot s^* + e_1^T B_2 \cdot \max_{i=1,\ldots,m} \left\{ T_{420}^{s,i} + {q_i}^T \cdot (s^* - x^{s,i}) \right\} \end{aligned}$$

Choosing the optimizer x_k and $T_{420,k}$ as below, therefore, leads to an objective value lower than J_n^*, which is again a contradiction.

$$\begin{aligned} x_k &= s^* \\ r_k &= \max_{i=1,\ldots,m} \left\{ T_{420}^{s,i} + {q_i}^T \cdot (s^* - x^{s,i}) \right\} \end{aligned}$$

Consequently, it can be concluded that condition (C.4) is true. Finally, the following inequality holds:

$$\begin{aligned} & e_1^T A \cdot x_k + e_1^T B_2 \cdot g_{comb}(x_k) \\ & \qquad \geq e_1^T A \cdot x_k + e_1^T B_2 \cdot \max_{i=1,\ldots,m} \left\{ T_{420}^{s,i} + {q_i}^T \cdot (x_k - x^{s,i}) \right\} \end{aligned} \tag{C.5}$$

This is because $e_1^T B_2$ is positive and the point-wise maximum of the hyperplanes is a global lower bound for g_{comb}. Combining condition (C.3), (C.4) and (C.5) gives

$$\begin{aligned} n_{k+1}^l &= J_n^* + e_1^T B_1 \cdot u_k + e_1^T d \\ &= e_1^T A \cdot x_k^* + e_1^T B_1 \cdot u_k + e_1^T B_2 \cdot r_k^* + e_1^T d \\ &= e_1^T A \cdot x_k^* + e_1^T B_1 \cdot u_k + e_1^T B_2 \cdot \max_{i=1,\ldots,m} \left\{ T_{420}^{s,i} + {q_i}^T \cdot (x_k^* - x^{s,i}) \right\} + e_1^T d \\ &\leq e_1^T A \cdot x_k + e_1^T B_1 \cdot u_k + e_1^T B_2 \cdot \max_{i=1,\ldots,m} \left\{ T_{420}^{s,i} + {q_i}^T \cdot (x_k - x^{s,i}) \right\} + e_1^T d, \quad \forall x_k \in \Phi_k \\ &\leq e_1^T A \cdot x_k + e_1^T B_1 \cdot u_0 + e_1^T B_2 \cdot g_{comb}(x_k) + e_1^T d, \quad \forall x_k \in \Phi_k \\ &= e_1^T \cdot x_{k+1} \end{aligned}$$

The above shows that $n_{k+1}^l = J_n^* + e_1^T B_1 \cdot u_k + e_1^T d$ is indeed a valid choice as a lower bound on oxygen content on the next cycle and completes the proof.□

With the knowledge of $C^T \cdot B_2 < 0$, **Theorem 7.4** can be proven in a similar manner.

Bibliography

[1] U.S. Energy Information Administration. Emissions of greenhouse gas report. *Report No.: DOE/EIA-0573(2008), released on Dec. 3 2009, revised on Dec. 8 2009*, 2009.

[2] U.S. Department of Energy. Vehicle per capita: U.S. vs. world. *http* : $//www1.eere.energy.gov/vehiclesandfuels/facts/2007\_fcvt\_fotw474.html$.

[3] The World Bank. Per capita carbon dioxide emissions. *http* : $//data.worldbank.org/indicator$.

[4] P.H. Lenz, K. Wichart, and D. Gruden. Variable valve timing - a possibility to control engine load without throttle. *SAE paper 880388*, 1988.

[5] T.G. Leone, E.J. Christenson, and R.A. Stein. Comparison of variable camshaft timing strategies at part load. *SAE paper 960584*, 1996.

[6] R.A. Stein, K.M. Galietti, and T.G. Leone. Dual equal VCT - a variable camshaft timing strategy for improved fuel economy and emissions. *SAE paper 950975*, 1995.

[7] T. Ahmad and M.A. Theobald. A survey of variable-valve-actuation technology. *SAE paper 891674*, 1989.

[8] T. Hosaka and M. Hamazaki. Development of the variable valve timing and lift (Vtec) engine for the Honda NSX. *SAE paper 910008*, 1991.

[9] F. Agrell, H-E. Angstrom, B. Eriksson, J. Wikander, and J. Linderyd. Integrated simulation and engine test of closed loop HCCI control by aid of variable valve timings. *SAE paper 2003-01-0748*, 2003.

[10] R.M. Richman. *The Flow Diagnostics Engine: A New System for Piston Engine Research*. PhD thesis, Stanford University, 1983.

[11] J.P. Hathout, J. Ahmed, and A. Kojic. Reduced order modeling and control of an electro-hydraulic valve system. In *Proceedings of the Fourth IFAC Symposium on Advances in Automotive Control*, 2004.

[12] R.M. Richman and W.C. Reynolds. A computer-controlled poppet-valve actuation system for application on research engines. *SAE paper 840340*, 1984.

[13] M.D. Anderson, T.C. Tsao, and M.B. Levin. Adaptive lift control of an electro-hydraulic camless valvetrain system. In *Proceedings of American Control Conference*, 1998.

[14] Z. Sun and D. Cleary. Dynamics and control of an electro-hydraulic fully flexible valve actuation system. In *Proceedings of American Control Conference*, 2003.

[15] M. Tomizuka, T.C. Tsao, and K.K. Chew. Analysis and synthesis of discrete-time repetitive controllers. *Journal of Dynamic Systems, Measurement and Control*, 111, Issue 3:353–358, 1989.

[16] A. Hultqvist, M. Christensen, B. Johansson, A. Franke, M. Richter, and M. Alden. A study of the homogeneous charge compression ignition combustion process by chemiluminescence imaging. *SAE paper 1999-01-3680*, 1999.

[17] H. Zhao, J. Li, T. Ma, and N. Ladommatos. Performance and analysis of a 4-stroke multi-cylinder gasoline engine with CAI combustion. *SAE paper 2002-01-0420*, 2002.

[18] M. Christensen, B. Johansson, and P. Einewall. Homogeneous charge compression ignition (HCCI) using isooctane, ethanol and natural gas-a comparison with spark ignition operation. *SAE paper 972874*, 1997.

[19] J. Li, H. Zhao, N. Ladommatos, and T. Ma. Research and development of controlled auto-ignition combustion in a 4-stroke multi-cylinder gasoline engines. *SAE paper 2001-01-3608*, 2001.

[20] J. Martinez-Frias, S.M. Aceves, D. Flowers, J.R. Smtih, and R. Dibble. HCCI engine control by thermal management. *SAE paper 2000-01-2869*, 2000.

[21] D. Law, D. Kemp, J. Allen, G. Kirkpatrick, and T. Copland. Controlled combustion in an IC-engine with a fully variable valve train. *SAE paper 2001-01-0251*, 2001.

[22] N.B. Kaahaaina, A.J. Simon, P.A. Caton, and C.F. Edwards. Use of dynamic valving to achieve residual-affected combustion. *SAE paper 2001-01-0549*, 2001.

[23] J. Allen and D. Law. Variable valve actuated controlled auto-ignition: speed load maps and strategic regimes of operation. *SAE paper 2002-01-0422*, 2002.

[24] P. Caton, A. Simon, J.C. Gerdes, and C.F. Edwards. Residual-affected homogeneous charge compression ignition at low compression ratio using exhaust reinduction. *International Journal of Engine Research*, 4, Number 3:163–177, 2003.

[25] G.M. Shaver, M.J. Roelle, and J.C. Gerdes. Decoupled control of combustion timing and work output in residual-affected HCCI engines. In *Proceedings of the 2005 American Control Conference*, 2005.

[26] S. Onishi, S-H. Jo, K. Shoda, P-D. Jo, and S. Kato. Active thermo-atmosphere combustion (ATAC) - a new combustion process for internal combustion engines. *SAE paper 790501*, 1979.

[27] M. Noguchi. A study on gasoline engine combustion by observation of intermediate reactive products during combustion. *SAE paper 790840*, 1979.

[28] P. M. Najt and D. E. Foster. Compression-ignited homogeneous charge combustion. *SAE paper 830264*, 1983.

[29] R. H. Thring. Homogeneous charge compression ignition (HCCI) engines. *SAE paper 892068*, 1989.

[30] R. Pfeiffer, G. Haraldsson, J-O. Olsson, P. Tunestål, R. Johansson, and B. Johansson. System identification and LQG control of variable-compression HCCI engine dynamics. In *Proceedings of the 2004 Conference in Control Applications*, 2004.

[31] J. Bengtsson, P. Strandh, R. Johansson, P. Tunestål, and B. Johansson. System identification of homogeneous charge compression ignition (HCCI) engine dynamics. In *Proceedings of the 2004 IFAC Symposium Advances in Automotive Control*, 2004.

[32] S.M. Aceves, D.L. Flowers, C.K. Westbrook, J.R. Smtih, W. Pitz, R. Dibble, M. Christensen, and B. Johansson. A multi-zone model for prediction of HCCI combustion and emissions. *SAE paper 2000-01-0327*, 2000.

[33] S.B. Fiveland and D.N. Assanis. Development of a two-zone HCCI combustion model accounting for boundary layer effects. *SAE paper 2001-01-1028*, 2001.

[34] S-C. Kong and R.D. Reitz. Application of detailed chemistry and CFD for predicting direct injection HCCI engine combustion and emissions. *Proceedings of the Combustion Institute*, 29, Issue 1:663–669, 2002.

[35] J. Kusaka, K-I. Tsuzuki, Y. Daisho, and T. Saito. Numerical study on combustion and exhaust gas emissions characteristics of a dual fuel natural gas engine using a multi-dimenstional model combined with detailed kintetics. *SAE paper 2002-01-1750*, 2002.

[36] S. Hong, M.S. Wooldridge, and D.N. Assanis. Modeling of chemical and mixing effects on methane autoognition under direct-injection, stratified charged conditions. *Proceedings of the Combustion Institute*, 29, Issue 1:711–718, 2002.

[37] G.M. Shaver, J.C. Gerdes, and M.J. Roelle. Physics-based closed-loop control of phasing, peak pressure and work output in HCCI engines utilizing variable valve actuation. In *Proceedings of the 2004 American Control Conference*, 2004.

[38] N. Ravi, M.J. Roelle, A.F. Jungkunz, and J.C. Gerdes. A physically based two-state model for controlling exhaust recompression HCCI in gasoline engines. In *Proceedings of the 2006 ASME International Mechanical Engineering Congress and Exposition*, 2006.

[39] C-J. Chiang and A.G. Stefanopoulou. Dynamics of homogeneous charge compression ignition (HCCI) engines with high dilution. *Prceedings of the 2007 American Control Conference*, pages 2979–2984, July 2007.

[40] A. Widd, P. Tunestål, C. Wilhelmsson, and R. Johansson. Control-oriented modeling of homogeneous charge compression ignition incorporating cylinder wall temperature dynamics. In *Proceedings of AVEC 2008*, 2008.

[41] J-M. Kang, C-F. Chang, J-S. Chen, and M-F. Chang. Concept and implementation of a robust HCCI engine controller. *SAE 2009-01-1131*, 2009.

[42] A. Widd, K. Ekholm, P. Tunestål, and R. Johansson. Experimental evaluation of predictive combustion phasing control in an HCCI engine using fast thermal management and VVA. In *Proceedings of the 2009 Conference in Control Applications*, 2009.

[43] G. Haraldsson, P. Tunestål, B. Johansson, and J. Hyvönen. HCCI combustion phasing with closed-loop combustion control using variable compression ratio in a multi-cylinder engine. *SAE paper 2003-01-1830*, 2003.

[44] J. Bengtsson, P. Strandh, R. Johansson, P. Tunestål, and B. Johansson. Model predictive control of homogeneous charge compression ignition (HCCI) engine dynamics. In *Proceedings of the 2006 Conference in Control Applications*, 2006.

[45] H.H. Song and C.F. Edwards. Optimization of recompression reaction for low-load operation of residual-effected HCCI. *SAE paper 2008-01-0016*, 2008.

[46] N. Ravi, H-H. Liao, A.F. Jungkunz, and J.C. Gerdes. Modeling and control of exhaust recompression HCCI using split injection. In *Proceedings of the 2010 American Control Conference*, 2010.

[47] J.O. Olsson, P. Tunestål, and B. Johansson. Closed-loop control of an HCCI engine. *SAE paper 2001-01-1031*, 2001.

[48] G.F. Franklin, J.D. Powell, and A. Emami-Naeini. *Feedback control of dynamic systems*. Prentice Hall, 5th edition, 2010.

[49] G.F. Franklin, J.D. Powell, and M.L. Workman. *Digital control of dynamic systems*. Prentice Hall, 3rd edition, 1997.

[50] N. Ravi, M.J. Roelle, H-H. Liao, A.F. Jungkunz, C.F. Chang, and J.C. Gerdes. Physical modeling and control of a multi-cylinder HCCI engine. In *Proceedings of the 2009 Dynamic Systems and Control Conference*, 2009.

[51] C-J. Chiang and A.G. Stefanopoulou. Steady-state multiplicity and stability of thermal equilibria in homogeneous charge compression ignition (HCCI) engines. In *Proceedings of the 2004 IEEE Conference on Decision and Control*, 2004.

[52] G.M. Shaver. Stability analysis of residual-affected HCCI using convex optimization. *IFAC Control Engineering Practice*, 17, Issue 12:1454–1460, 2009.

[53] C-J. Chiang and A.G. Stefanopoulou. Nonlinear observer-based control of load transitions in homogeneous charge compression ignition engines. *IEEE Transactions on Control Systems Technology*, 15:438–448, 2007.

[54] W.H. Kwon and D.G. Byun. Receding horizon tracking control as a predictive control and its stability properties. *International Journal of Control*, 50, Issue 5:1807–1824, 1989.

[55] M. Uchiyama. Formulation of high speed motion pattern of a mechanical arm by trial. *Transactions of the Society of Instrumentation and Control Engineers*, 14:706–712, 1978.

[56] S. Arimoto, S. Kawamura, and F. Miyazaki. Bettering operation of dynamic systems by learning: A new control theory for servomechanism or mechatronics systems. In *Proceedings of the 1984 IEEE Conference on Decision and Control*, 1984.

[57] G. Casalino and L. Gambardella. Leraning of movements in robotic manipulators. In *Proceedings of the 1986 IEEE Conference on Robotics and Automation*, 1986.

[58] N. Ravi, M.J. Roelle, H-H. Liao, A.F. Jungkunz, C-F. Chang, S. Park, and J.C. Gerdes. Model based control of HCCI engines using exhaust recompression. *IEEE Transactions on Control Systems Technology*, 18, Issue 6, 2010.

[59] G.M. Shaver. *Physics-based modeling and control of residual-affected HCCI engines using variable valve actuation.* PhD thesis, Stanford University, 2005.

[60] N. Ravi. *Modeling and control of exhaust recompression HCCI using variable valve actuation and fuel injection.* PhD thesis, Stanford University, 2010.

[61] C-J. Chiang and A.G. Stefanopoulou. Sensitivity analysis of combustion timing of homogeneous charge compression ignition gasoline engines. *Journal of Dynamic Systems, Measurement, and Control*, 131:014506 (5 pages), 2009.

[62] A. Widd, H-H. Liao, J. C. Gerdes, P. Tunestål, and R. Johansson. Control of exhaust recompression HCCI using hybrid model predictive control. In *Proceedings of the 2011 American Control Conference*, 2011.

[63] S. Boyd and L. Vandenberghe. *Convex Optimization.* Cambridge University Press, 2004.

[64] M. Grant and S. Boyd. CVX: Matlab software for disciplined convex programming, version 1.21. *http* : *//cvxr.com/cvx*, August 2010.

[65] S. Boyd, L.E. Ghaoui, E. Feron, and V. Balakrishnan. *Linear Matrix Inequalities in System and Control Theory.* Society for Industrial and Applied Mathematics, 1994.

[66] H. Ye, A. N. Michel, and L. Hou. Stability theory for hybrid dynamical systems. *IEEE Transactions on Automatic Control*, 43, No. 4:461–474, 1998.

[67] Z-P. Jiang and Y. Wang. A converse Lyapunov theorem for discrete-time systems with disturbances. *System and control Letters*, 45, No. 1:49–58.